VOL. VII - N.º 1 - 1985 ISSN 0100-7386

REVISTA BRASILEIRA DE CIÊNCIAS MECÂNICAS

PUBLICAÇÃO DA ABCM
ASSOCIAÇÃO BRASILEIRA DE CIÊNCIAS MECÂNICAS

A Revista Brasileira de Ciências Mecânicas é uma publicação técnico-científica, da Associação Brasileira de Ciências Mecânicas. Destina-se a divulgar trabalhos significativos de pesquisa científica e/ou tecnológica nas áreas de Engenharia Civil, Mecânica, Metalúrgica, Naval, Nuclear e Química e também em Física e Matemática Aplicada. Pequenas comunicações que apresentem resultados interessantes obtidos de teorias e técnicas bem conhecidas serão publicadas sob o título de Notas Técnicas.

Os trabalhos submetidos devem ser inéditos, isto é, não devem ter sido publicados anteriormente em periódicos de circulação nacional ou internacional. Excetuam-se em alguns casos publicações em anais e congressos. A apreciação do trabalho levará em conta a originalidade, a contribuição à ciência e/ou tecnologia, a clareza de exposição, a propriedade do tema e a apresentação. A aceitação final é da responsabilidade dos Editores e do Conselho Editorial.

Os artigos devem ser escritos em português, ou espanhol ou em inglês, datilografados, acompanhados dos desenhos em papel vegetal, em tamanho reduzido que permita ainda a redução para as dimensões da Revista e enviados para o Editor Executivo no endereço abaixo.

Departamento de Engenharia Mecânica – PUC/RJ
Rua Marquês de São Vicente, 225 – Gávea
22453 – Rio de Janeiro – RJ – Brasil

A composição datilográfica será processada pela própria secretaria da RBCM de acordo com as normas existentes.

The Revista Brasileira de Ciências Mecânicas (Brazilian Journal of Mechanical Sciences) is a technical-scientific publication, sponsored by the Brazilian Association of Mechanical Sciences. It is intended as a vehicle for the publication of Civil, Mechanical, Metallurgical, Naval, Nuclear and Chemical Engineering as well as in the areas of Physics and Applied Mathematics. Short communications presenting interesting results obtained from well-known theories and techniques will be published under heading the of Technical Notes.

Manuscripts for submission must contain unpublished material, i.e., material that has not yet been published in any national or international journal. Exception can be made in some cases of papers published in annals or proceedings of conferences. The decision on acceptance of papers will take into consideration their originality, contribution to science and/or technology, writing clearness, propriety of the subject and presentation. The Editors and the Editorial Committee are responsible for the final approval.

The papers must be written in Portuguese, Spanish or English, typed and with graphics done on transparent white drawing paper in reduced size in such a way as to permit further reduction to the dimensions of the Journal, and sent to the Executive Editor at the following address.

PUC – Pontifícia Universidade Católica do RJ
Departamento de Engenharia Mecânica
Rua Marquês de São Vicente, 225 – Gávea
22453 – Rio de Janeiro, RJ – Brasil

The final typing will be done by the secretary of RBCM according to the journal norms.

REVISTA
BRASILEIRA DE
CIÊNCIAS
MECÂNICAS

Vol. VII. nº 1 - Fev. 1985

J. DI GIORGIO EDITORES
TEL.: 261-5042 (PABX)

A REVISTA BRASILEIRA DE CIÊNCIAS MECÂNICAS
É PUBLICADA COM O APOIO

DO CNPq E FINEP
COMPANHIA VALE DO RIO DOCE
IBM DO BRASIL

EDITORIAL

O ritmo de publicação da **RBCM** está dependendo da cooperação dos pesquisadores, de sua produtividade e dos recursos da ABCM para manter ou mesmo ampliar a freqüência e volume de publicações.

A questão de cooperação embora tendo progredido, ainda não atingiu um nível ótimo. Isto é, o número de trabalhos encaminhados ainda não representa uma cifra adequada. Diga-se de passagem que os revisores têm procurado manter as exigências de qualificação e adequação dentro dos padrões requeridos pela ABCM. Isto constitui de certa forma um obstáculo ao aumento indiscriminado de volume de trabalhos aceitos, mas é uma orientação da qual não podemos abrir mão. A canalização de um volume maior de contribuições de bom nível técnico tenderá a se consolidar na medida em que a **RBCM** for adquirindo maior tradição. Por outro lado, o encaminhamento da parte da matéria atualmente apresentada nos diversos Congressos e Simpósios, para a **RBCM**, poderá aumentar substancialmente o volume da Revista.

O segundo fator relacionado com a produtividade dos meios acadêmicos e atuantes em pesquisa escapa ao controle da ABCM. A nossa função, com os recursos de que dispomos atualmente, é tentar estimular esta produtividade através, principalmente, da cooperação com o setor empresarial. A **RBCM** e os eventos patrocinados pela ABCM servem para medir a produtividade e a sua qualidade, sendo mais efeito do que causa de produção.

O terceiro ponto, que se refere aos recursos, está fundamentalmente associado ao prestígio que a ABCM desfruta nos segmentos da sociedade aos quais interessam as atividades da Associação. Além do setor acadêmico, que manifestamente apoia a ABCM, temos tido a felicidade de ver que o setor empresarial, aos poucos, toma consciência da importância da Associação e começa a apoiar concretamente as nossas atividades. Neste ano em que a ABCM completa 10 anos de existência, foi lançada uma campanha de Sócio Institucional Especial. Várias empresas manifestaram o interêsse em afiliarem-se à ABCM nesta categoria e a primeira a materializar o seu apoio foi a **IBM do Brasil**. Estamos certos de que, daqui para a frente, e cada vez mais, poderemos contar com o apoio do setor empresarial. É graças em parte a este apoio que podemos este ano, distribuir o primeiro número da **RBCM** dentro do prazo regular. Para chegarmos a esta situação passamos por momentos difíceis, e é importante que se diga que tivemos na FINEP um esteio imprescindível, sem o qual não poderíamos ter sobrevivido.

DETERMINATION OF BENDING-FREE GEOMETRIES FOR SHELLS OF REVOLUTION UNDER AXISYMMETRIC LOADS

Luiz Bevilacqua, Membro da ABCM
Departamento de Engenharia Mecânica - PUC/RJ
Dauro Braga Noronha Junior, Membro da ABCM
Natron - Consultoria e Projetos S/A.

ABSTRACT

The present paper, deals with the determination of a bending free shell geometry connecting a pipe and a spherical pressure vessel. The boundary conditions do not represent the real situation at this stage. It is shown however, that under the action of an uniform internal pressure, for a transition with variable thickness, there are enough degrees of freedom to perform the matching of the displacements between the nozzle and the spherical vessel.

RESUMO

O presente trabalho apresenta a derivação de uma geometria livre de flexão unindo um tubo com um vaso esférico. As condições de contorno ficam em parte violadas no estágio atual da análise. Entretanto, demonstra-se que a variação de espessura introduz graus de liberdade suficientes para se conseguir a compatibilidade de deslocamentos entre o bocal e a esfera.

INTRODUCTION

The design of pressure vessels requires the opening of holes in the proper places to allow for the connection with the inlet and outlet pipes [1].

The nozzle are the special structural components forming the transition between the pipe and the shell. They usually are submitted to severe mechanical loading and the stress levels are correspondingly high [2,3]. The most critical internal load is tne bending moment which usually limits the allowable external forces.

One of the main reasons that accounts for the high stress levels generated at the nozzles can be attributed to the geometry of the transition. This geometry commonly presents sharp discontinuities, in contrast with a desirable smooth transition from the pipe to the shell. The standard design as a matter of fact, is a simple intersection between the pipe and the shell, with a reinforcing plate welded to the vessel wall around the penetration zone. Figure 1(a), illustrates this type of design, for a welded nozzle.

For some special equipments with very strict safety requirements and high reliability standards it is worthwhile introducing a smoother transition as shown in Figure 1(b). This nozzle has to be fabricated through forging processes or machining which leads to higher costs. But they certainly pay off considering the better stress distribution and the associated structural integrity of the equipment.

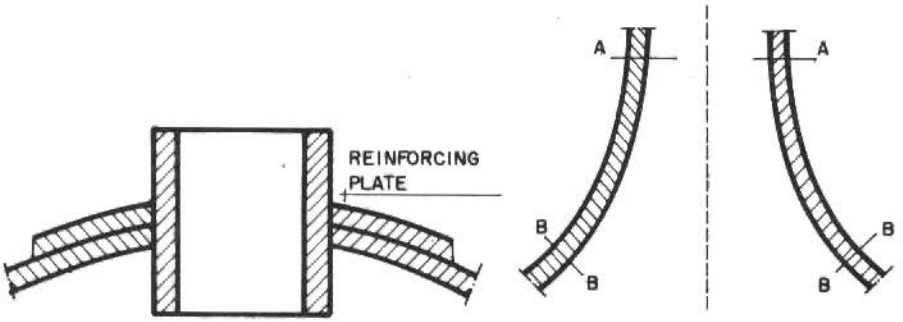

(a) STANDARD NOZZLE (b) BENDING FREE SHAPE

Figure 1. Transition types

A basic question concerning the intuitive smooth geometry, depicted in the Figure 1(b), is related to the possibility of finding a well defined meridional curve which would lead to the most convenient stress distributions. A trial and error approach is discarded from the very beginning since it does not provide a rational guide to the design. The determination of a proper shape needs the imposition of some mechanical conditions at the outset. In this paper we are concerned with transitions which will basically satisfy the following assumptions:

i) The vessel and nozzle are axissymmetric with respect to the same axis of revolution.

ii) The loads are axissymmetric, and the main external force are the axial force and the internal pressure.

iii) Pipe, nozzle and vessel can be analysed under the classical frame of the thin shell theory [4,5].

iv) The geometry of the nozzle, defined as the transition region between the pipe and the vessel, is bending free under the given constraint and boundary conditions. In Figure 1(b) for instance, the nozzle is the region within the section A-A and B-B.

This last statement deserves further explanations. It can be easily seen that there are two free geometric parameters to achieve the bending free conditions, namely the meridiam curve and the thickness. On the other hand the following geometric boundary conditions have always to be fulfilled:

i) At the pipe end: $r = r_t$, $\phi = \pi/2$

ii) At the vessel end: $r = r_b$, $\phi = \phi_b$

where r is the radius of the paralel circle and ϕ the angle between the meridional curvature radius and the vertical as shown in the Figure 2.

Now, the two geometric parameters exceed the number of necessary constraints required to define the pure membrane state together with the above geometric boundary conditions, provided that for $r = r_t$ and $r = r_b$ the shell (nozzle) is free to displace and rotate. Therefore other extra compatible constraints can be introduced, as imposed displacements at the edges to match the corresponding ones of the pipe of the pressure vessel, or full plastic state ocurring simultaneously for all sections of the nozzle, just to give two examples. How many extra constraints can be worked out simultaneously is not clear yet. Also, how to

determine the compatibility conditions is not yet a completely closed question. Both problems need to be deeply explored. Anyway, the fundamental requirement arising from the assumption iv) is that the geometry guarantees a pure membrane state for the given external loading and geometric boundary conditions at least for the simplest class of kinematic conditions at the edges, namely: free displacements and rotations.

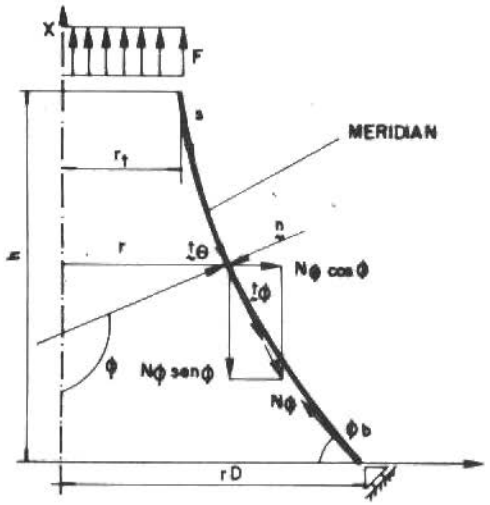

Figure 2. Geometry, internal forces and loading

This fundamental problem will be the central topic of the present paper. Clearly a transition shell, free to displace at the edges will not be kinematically compatible with the pipe and pressure vessel. This means that when the nozzle is coupled with the vessel it will not go into a pure membrane state. We will see however, that it is possible to develop the theory to solve this problem and that even for the first approximation the bending moments arising from the external loading are much smaller than the corresponding ones for the conventional design. In other words we will examine here a first approximation of the real problem and indicate how an improved solution can be carried through.

THE PURE MEMBRANE CONDITIONS

The derivation of the governing equations for the pure membrane state is not a difficult task. It lies upon the classical equilibrium equations, strain-displacement relations for rotationally symmetric shells, and Hooke's law. They are [4,5]:

Equilibrium equations

$$N_\phi - \frac{d}{dr}(r\,N_\phi) = q_\phi\, r \sec\phi \qquad (1.a)$$

$$\frac{d}{dr}(N_\phi\, r \sin\phi) = -q_\phi\, r \tan\phi - pr \qquad (1.b)$$

Strain-displacement relations

$$\chi_\phi = \frac{1}{r_\phi}\frac{d}{d\phi}\left(\frac{u_\phi}{r_\phi} + \frac{1}{r_\phi}\frac{dw}{d\phi}\right) \qquad (2.a)$$

$$\chi_\theta = \frac{\cos\phi}{r}\left(\frac{u_\phi}{r_\phi} + \frac{1}{r_\phi}\frac{dw}{d\phi}\right) \qquad (2.b)$$

$$\varepsilon^o_\phi = \frac{1}{r_\phi}\left(-\frac{dw}{d\phi} + w\right) \qquad (3.a)$$

$$\varepsilon^o_\theta = \frac{1}{r}(-u_\phi \cos\phi + w \sin\phi) \qquad (3.b)$$

Hooke's law

$$\varepsilon^o_\phi = \frac{1}{Et}(N_\phi - \nu N_\theta) \qquad (4.a)$$

$$\varepsilon^o_\theta = \frac{1}{Et}(N_\theta - \nu N_\phi) \qquad (4.b)$$

The symbols appearing in the above equations are classical and a detailed explanation is skipped here.

The fundamental condition for a bending free shell or a pure membrane estate is:

$$u_\phi + \frac{dw}{d\phi} = 0 \qquad (5)$$

Combining the equations (1), (3), (4) with the relation (5) the following condition is obtained in terms of the generalized meridional and circumferential forces N_ϕ and N_θ respectively [6,7]:

$$\frac{d}{dr}(N_\phi + N_\theta) = (N_\theta - \nu N_\phi)\frac{1}{t}\frac{dt}{dr} + (1+\nu)q_\phi \sec\phi \qquad (6)$$

Now working out this equation, and making use of the equations (1) through (4) it is possible to arrive to the three following equivalent conditions:

$$\xi^2 \frac{d^2\sigma}{d\xi^2} + (3+h)\xi\frac{d\sigma}{d\xi} + (1+\nu)h\,\sigma = 0 \qquad (7.a)$$

$$\xi^2 \frac{d^2\sigma_\phi}{d\xi^2} + (3+h)\xi\frac{d\sigma_\phi}{d\xi} + (\xi h' + (1+\nu)h)\sigma_\phi = 0 \qquad (7.b)$$

$$\frac{1}{\xi^2}\left(K+\frac{1}{2}\right) = \frac{1}{2} + \frac{h+2g-2}{1-hg-g^2+\xi g'-\nu h} \qquad (7.c)$$

where:

$$\xi = \frac{r}{r_t} \quad , \quad \sigma_\phi = N_\phi/t \quad , \quad \sigma_\theta = N_\theta/t \quad , \quad \sigma = \sigma_\theta - \nu\sigma_\phi$$

$$h = \frac{\xi}{t}\frac{dt}{d\xi} \quad , \quad g = \frac{\xi}{\sin\phi}\frac{d}{d\xi}\sin\phi$$

$$K = (\sigma_\phi^t\, t_t)/p\, r_t$$

p is the pressure normal to the middle surface. Internal pressure is negative, external pressure positive. r_t, t_t and σ_ϕ^t are respectively the radius of the nozzle, the wall thickness and the longitudinal stress at the edge connected to the pipe. For the equations (7) it was assumed that $q_\phi = 0$.

The proper selection of the equations (7.a), (7.b) or (7.c) depends on the boundary and constraint conditions. From those equations it is seen that $h(\xi)$ is a natural control parameter. If it is determined from (7.a) or (7.b) the geometry of the meridian can be obtained for instance from (7.c).

All the compatible solutions of (7.a-c) satisfy the pure membrane state requirements for unconstrained edges, except for the support in the tangential direction at either edge to prevent rigid body displacements. Taking (7.c) for instance, it is easily seen that there are several functions $g(\xi)$ and $h(\xi)$ that satisfy the geometric boundary conditions r_h, $\pi/2$; r_t, ϕ_b, allowing therefore for extra constraints.

A very important case concerns pressure vessels under internal pressure only. For this loading the value of K equals - 1/2 and the equation (7.c) reduces to:

$$\xi\, g' + (4 - h - g)g + h(2 - \nu) - 3 = 0 \qquad (7.d)$$

This is a non-linear first order equation whose solution in general can not be put into a closed form [8]. The choice of $f = h + g$ as a control parameter reduces the above equation to a linear Riccatti's form:

$$\xi\, g' + [2 + \nu - f]g + (2 - \nu)f - 3 = 0 \qquad (7.e)$$

Note that f is a very convenient parameter:

$$f = \xi \frac{d}{d\xi} \ell n(t \sin\phi)$$

Let us assume that $t \sin\phi = u(\xi)$ can be arbitrarily chosen, since $t(\xi)$ is an arbitrary positive differentiable function of ξ, among all sufficiently smooth functions which satisfies:

$$0 < \frac{u(\xi)}{t(\xi)} \leq 1 \qquad 1 \leq \xi \leq \xi_b$$

Then the solution of (7.e) is:

$$g(\xi) = -\frac{u}{\xi^{2+\nu}}\left[\int_1^{\xi} \left[(2 - \nu)\frac{d}{d\xi} \ell n\, u - \frac{3}{x}\right] \frac{x^{2+\nu}}{u}\, dx + C_1\right] \qquad (8)$$

The constant C_1 and the other one appearing from the integration of $g(\xi)$ to obtain $\sin\phi$ are sufficient to match the geometric boundary conditions at $r = r_t$ and $r = r_b$. The selection of the control function $u(\xi)$ is then left free to match other boundary conditions or constraints.

If the constraint is expressed in terms of a differential equation involving $u(\xi)$, say:

$$F(u,g) = 0 \qquad (9)$$

then (8) and (9) can be solved to give $u(\xi)$ and $g(\xi)$. If the constraint is a boundary condition, then the equations will be of

the form:

$$H(u(1), g(1)) = H_t \quad \text{at} \quad r = r_t \tag{10.a}$$

$$H(u(\xi_b), g(\xi_b)) = H_b \quad \text{at} \quad r = r_b \tag{10.b}$$

where H_t and H_b are constants and $\xi_b = r_b/r_t$. In this case there will possibly be several functions $u(\xi)$ which will fit the imposed conditions and the solution is not unique.

similar analysis can also be applied to the differential equation (7.a) or (7.b).

PARTICULAR SOLUTIONS FOR VARIABLE THICKNESS

In this section some particular cases will be considered using analytical solutions rather than numerical methods. This will be done in order to get a better insight into the behavior of the solutions. Using equations (7.b) and (7.c) the influence of the control parameters $t(\xi)$ and $u(\xi) = t \sin\phi$ will be tested.

The geometries that can be generated by solving the equations (7.a), (7.b) or (7.c) are shown in the Figure 3.

Figure 3(a) represents the typical case of a nozzle, Figure 3(b) provides the proper shape for the transition between a conical and a cylindrical shell and Figure 3(c) shows a reduction in the diameter of a pipeline. The following discussion assumes the existence of internal pressure and the corresponding axial load.

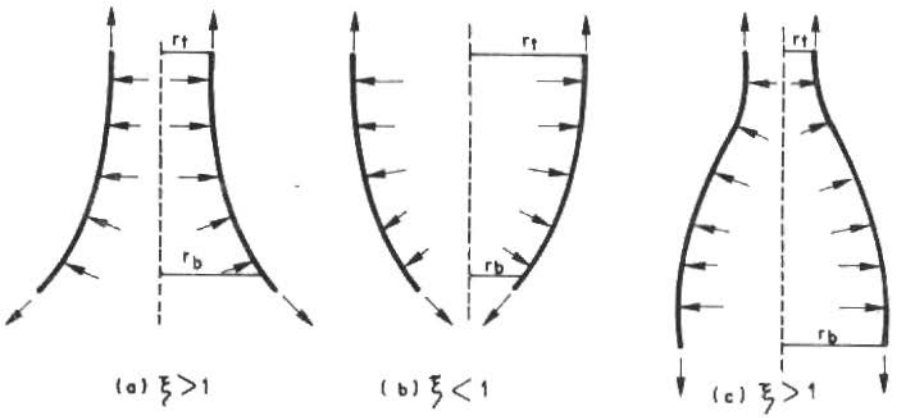

Figure 3. Possible bending free geometries

a) $\xi g' + [2 + \nu - f] g + (2 - \nu) f - 3 = 0$

The solution of this equation is given by the expression (8). The control variable $u(\xi)$ will be assumed to be of the form, $u(\xi) = t_0 \xi^k$. Substituting this expression into equation (8) and recalling the geometric boundary conditions:

$$\phi(1) = \pi/2$$

$$\phi(\xi_b) = \phi_b$$

the following equation is obtained:

$$\sin\phi = \xi^\beta \left[\frac{\sin\phi_b}{\xi_b^\beta} \right]^{(\xi^\gamma - 1)/(\xi_b^\gamma - 1)} \qquad (11)$$

where:

$$\beta = \frac{3 - (2-\nu)k}{2 + \nu - k}$$

$$\gamma = k - 2 - \nu$$

The condition $|\sin\phi| \leq 1$ determines a restriction in the choice of k, given the boundary conditions r_b and ϕ_b. For the geometries shown in the Figure 3(a) a sufficient condition for the existence of the solution is $\beta < 1$ which leads to:

$$3/(2 - \nu) < k < 2 + \nu$$

This is a sufficient, although not a necessary condition.

Taking $k = 0$ for instance, and assuming that:

$$\xi_b = \frac{r_b}{r_t} > \left[\frac{1}{\sin\phi_b} \right]^{1/(2+\nu)}$$

there will be no solutions for the geometry corresponding to the Figure 3(a). For the case shown in Figure 3(b), however, there will be solutions because the variable $\xi = r/r_b$ is always less than one.

Then the existence of a solution, for this particular choice of the variable $u(\xi)$ will depend on the value of k.

b) $\xi^2 \sigma_\phi'' + (3 + h)\xi \sigma_\phi' + (\xi h' + (1 + \nu)h)\sigma_\phi = 0$

Here the control variable is $h(\xi)$, related to the shell thickness. In order to arrive at closed solution forms, the following particular law for the variation of $t(\xi)$ will be taken:

$$t = t_o \xi^k \tag{12}$$

In this case the differential equation reduces to:

$$\xi^2 \sigma_\phi'' + (3+k)\xi \sigma_\phi' + (1+\nu)k \sigma_\phi = 0 \tag{13}$$

which has the well known solution:

$$\sigma_\phi = C_1 \xi^{\beta_1} + C_2 \xi^{\beta_2} \tag{14}$$

where:

$$\beta_1 = \frac{1}{2}(-2 - k + \sqrt{k^2 + 4k(1-\nu)})$$

$$\beta_2 = \frac{1}{2}(-2 - k - \sqrt{k^2 + 4k(1-\nu)})$$

and C_1, C_2 are constants that are determined from the boundary conditions:

$$C_1 = \frac{p\, r_t}{2\, t_o} \; \frac{\dfrac{t_o}{t_b \sin\phi_b} - \xi_b^{\beta_1 - 1}}{\xi_b^{\beta_1 - 1} - \xi_b^{\beta_2 - 1}}$$

$$C_2 = \frac{p\, r_t}{2\, t_o} \; \frac{\dfrac{-t_o}{t_b \sin\phi_b} - \xi_b^{\beta_2 - 1}}{\xi_b^{\beta_1 - 1} - \xi_b^{\beta_2 - 1}}$$

Now, recalling that

$$\frac{d}{d\xi}(t\, \xi\, \sigma_\phi \sin\phi) = -p\, r_t\, \xi$$

and $\sin\phi = 1$ for $\xi = 1$, the expression for $\sin\phi$ is easily obtained:

$$\sin\phi = -\frac{p\, r_t}{2\, t_o} \xi^{1-k} \frac{1}{C_1 \xi^{\beta_1} + C_2 \xi^{\beta_2}} \tag{15}$$

The value of k can be determined by a compatible constraint condition. It is worthwhile remarking that this case can be used to determine the geometry of a bending free reducer as shown in Figure 3(c). Taking for instance $k = 1/2$, $\xi_b = 2$ and $\sin\phi_b = 1$ which characterizes the geometry of a reducer, the following variation for $\sin\phi$ is obtained:

ξ	$\sin\phi$	t/t_o
1.0	1.0	1.000
1.25	0.8603	1.118
1.50	0.8727	1.225
1.75	0.9273	1.323
2.00	1.0	1.414

A PARTICULAR SOLUTION FOR AXIAL LOADING

A complete set of solutions was obtained for the case of axial loading only. The shell was taken first with constant tickness and an exact solution was derived assuming botn edges free to displace along the normal direction and to rotate in the meriodiond plane.

For the particular case where $p = 0$, the equation (7.c) reduces to:

$$1 - hg - g^2 + \xi g' - \nu h = 0 \qquad (16.a)$$

Under the assumption of constant thickness the above expression simplifies to:

$$1 - g^2 - \xi g' = 0 \qquad (16.b)$$

This equation can be easily integrated leading to the follwing solution:

$$\sin\phi = \frac{r\, r_t}{ar^2 + r_t^2(1-a)} \qquad (17)$$

where

$$a = \frac{r_t(r_b - r_t \sin\phi_b)}{(r_b^2 - r_t^2)\sin\phi_b}$$

From (17) and recalling that $\tan\phi = dz/dr$ the expression of the curve $z(r)$ can be easily found:

$$z = \frac{r_t}{a} \ell n \left\{ (r^2 - r_t^2)^{1/2} + (r^2 - (a-1)^2 r_t^2/a^2)^{1/2} \right\}_r^{r_b} \qquad (18)$$

There are real solutions only for $a \geq 0.5$. Figures 4 and 5 show the various shapes for the nozzle and the variation of the nozzle height versus the ratio r_b/r_t, for a given ratio $r_e/r_t = 20$. This ratio, representing the relation between the radius of a spherical vessel and the radius of the connected pipe determines the angle ϕ_b. The limiting value of the parameter "a" is associated with the height of the nozzle. From Figure 5 it is seen that the limiting ratio of r_b/r_t is 6.45 for which the height tends to infinity.

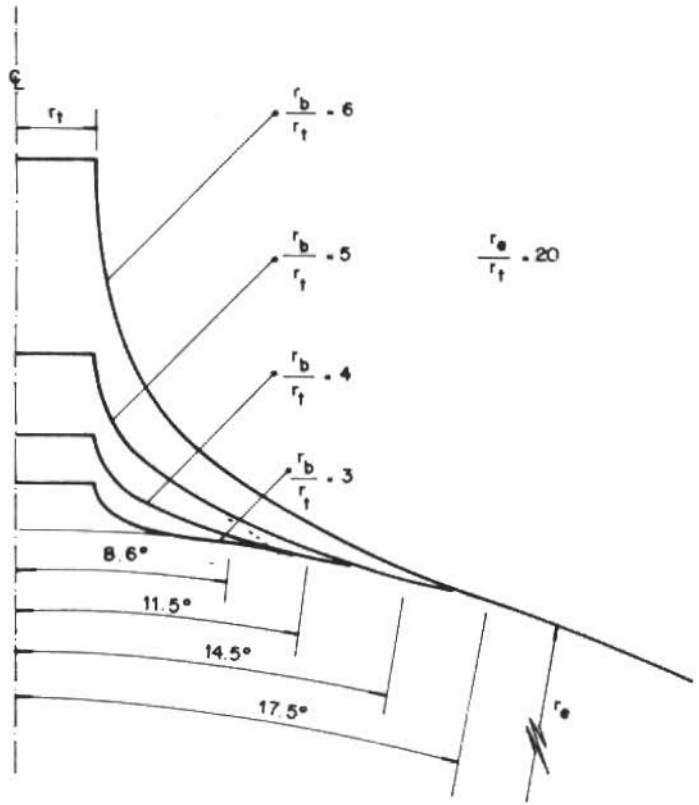

Figure 4. Bending free shapes for axial loading

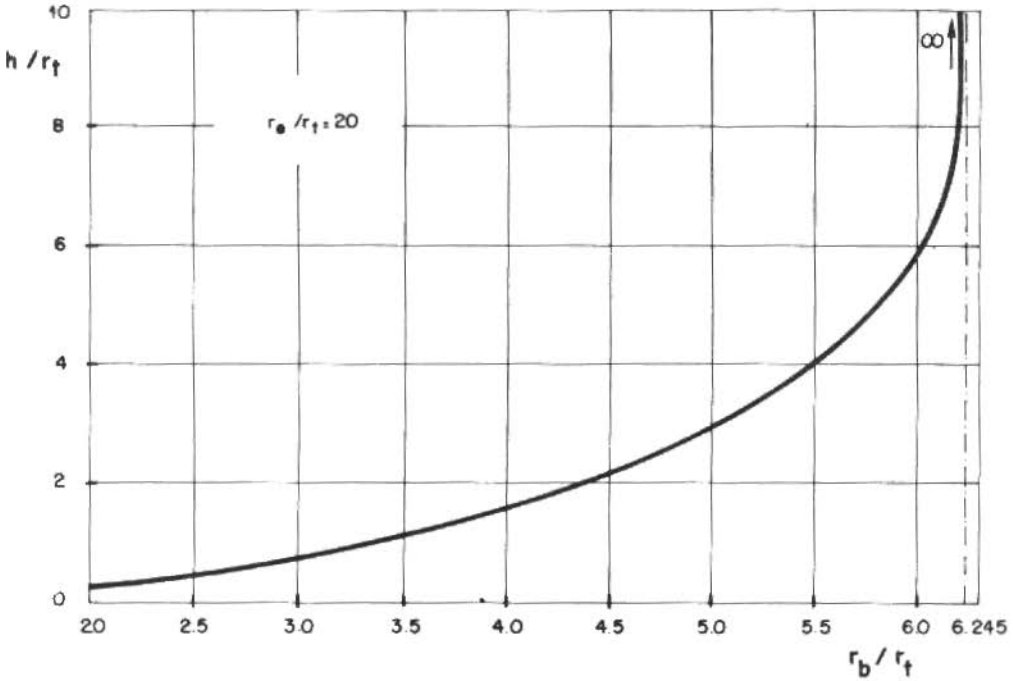

Figure 5. Nozlle height versus the pipe radius

The generalized forces N_ϕ and N_θ in an reduced form are shown in Figures 6(a) and 6(b) for the ideal case of free edges.

The perturbation introduced by the real boundary conditions, that is, for the case of a continuous transition from the nozzle to the spherical shell can be seen in the Figures 7(a) througth 7(d). The membrane forces N_ϕ and N_θ are not essentially modified, but the free bending conditions are not fulfilled anymore. The bending moments M_ϕ and M_θ are however kept at sufficiently low levels. In the Figure 8 a reduced form of the maximum shear stress is depicted versus the ratio r_b/r_t. It is clearly seen the advantage of the present shape compared with the standard design. The maximum reduced shear stress for the standard nozzle is 13.1 much higher than 1.08 found for the "bending free shape" with $r_b/r_t = 4.0$.

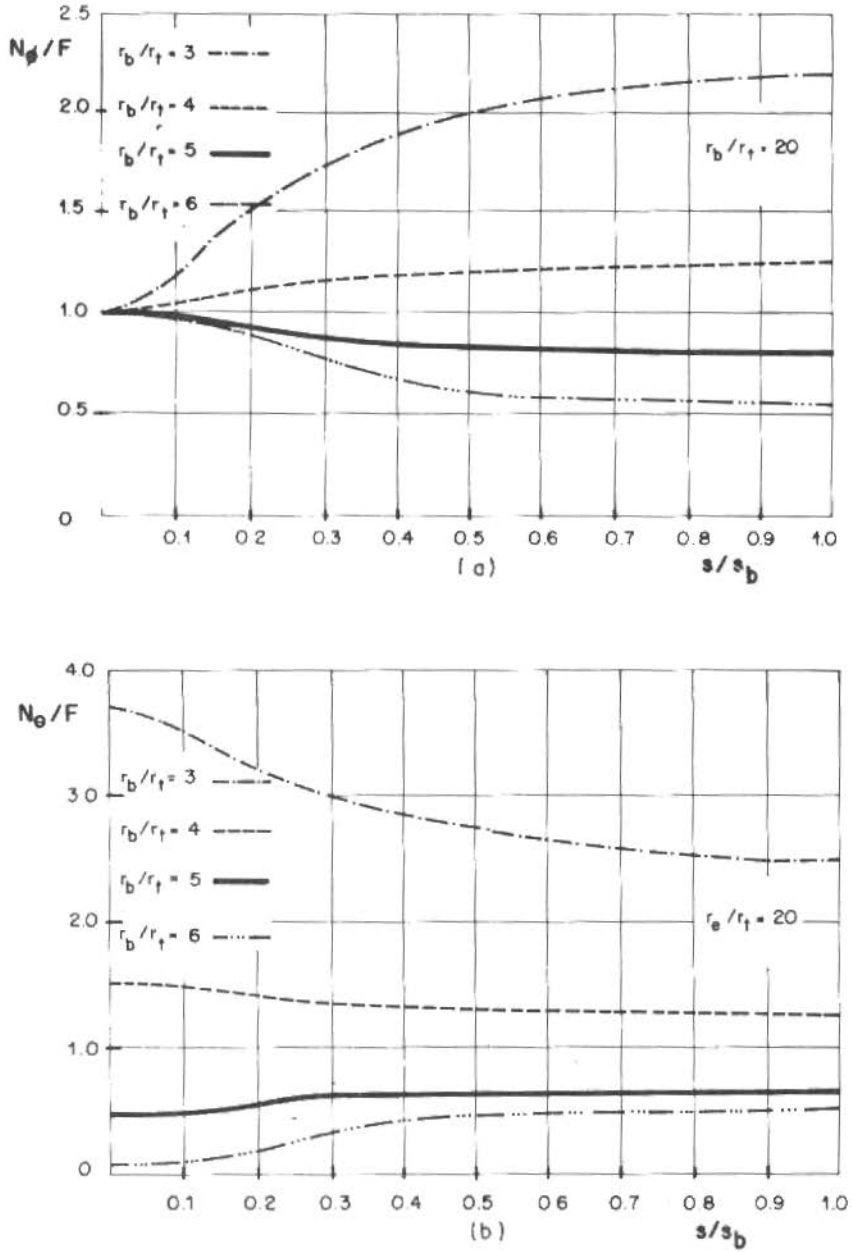

Figure 6. (a) Longitudinal force N_ϕ for constant thickness nozzle under axial loading and ideal boundary conditions

(b) Circumferential force N_θ for constant thickness nozzle under axial loading and ideal boundary conditions

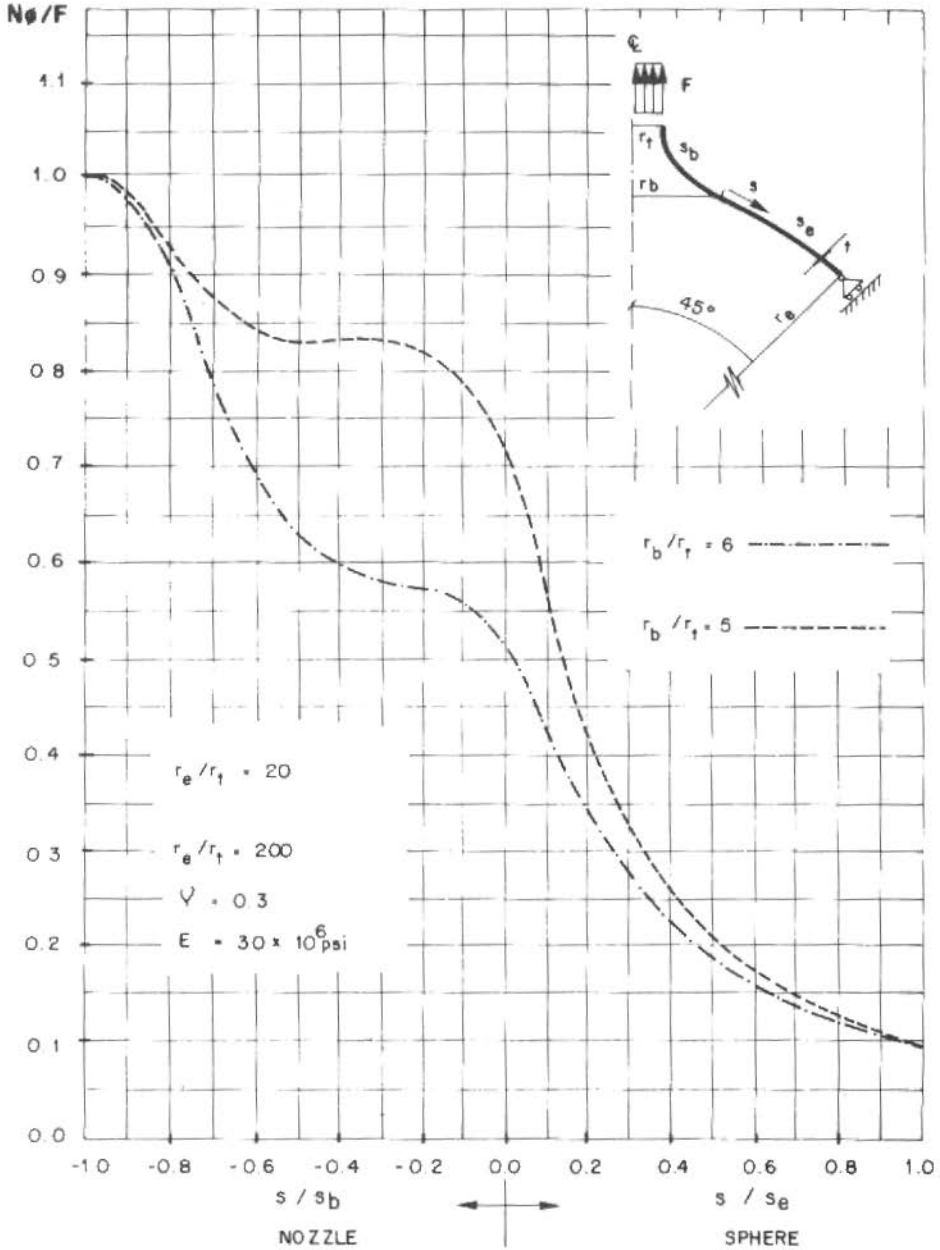

Figure 7(a). Longitudinal force N_ϕ for constant thickness nozzle under axial loading, attached to a spherical shell

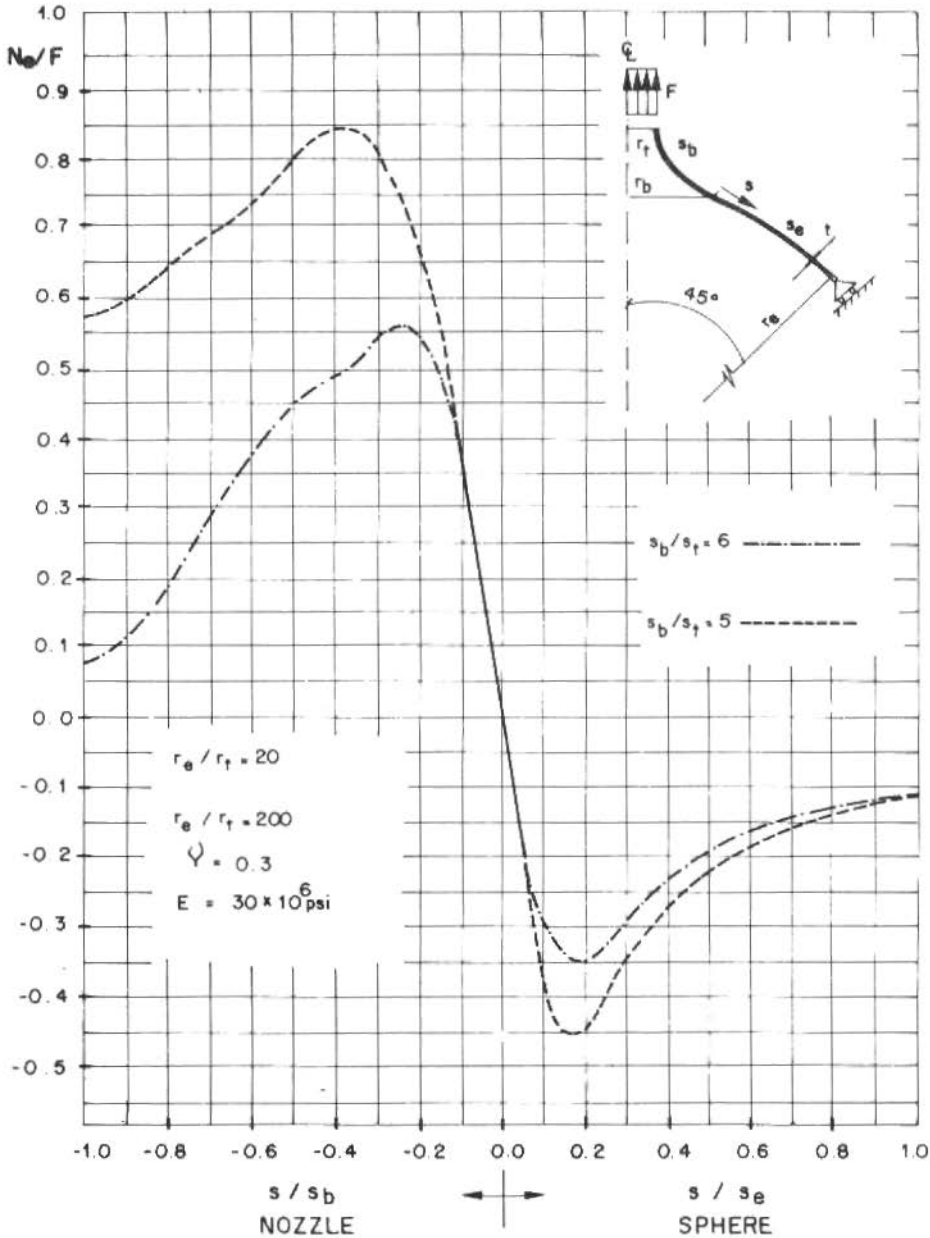

Figure 7(b). Circumferential force N_θ for constant thickness nozzle under axial loading, attached to a spherical shell

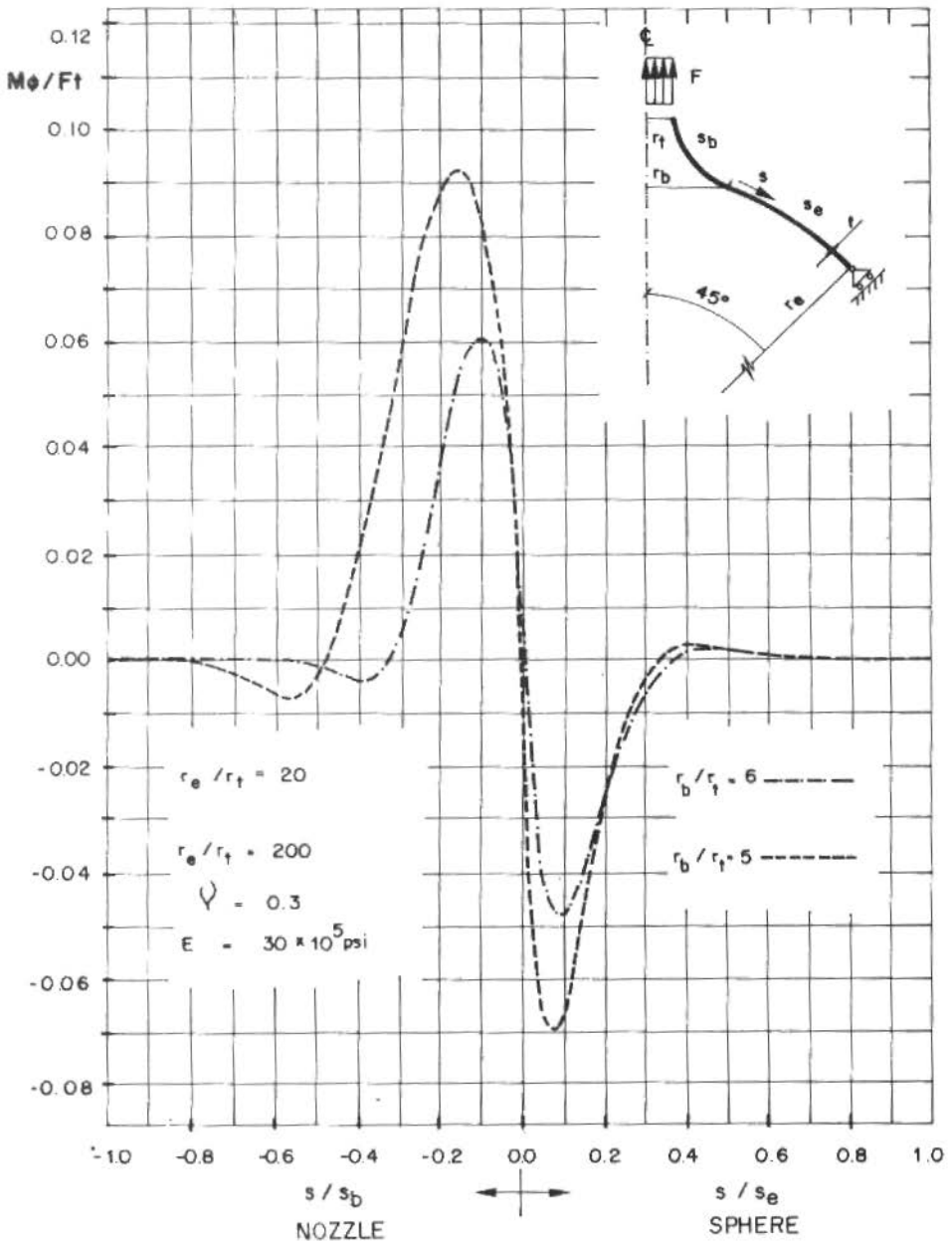

Figure 7(c). Longitudinal bending moment M_ϕ for constant thickness nozzle under axial loading, attached to a spherical shell

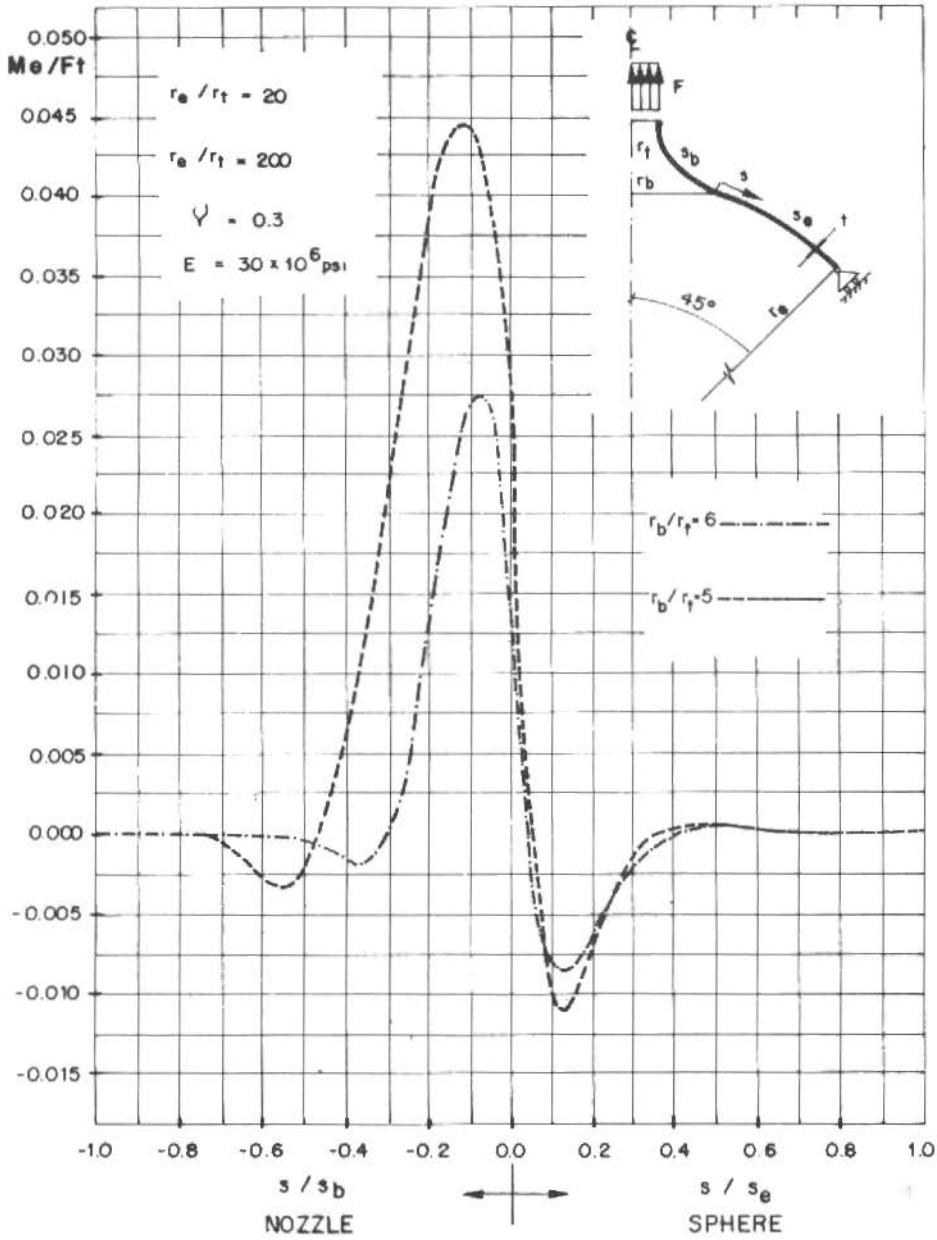

Figure 7(d). Circumferential bending moment M_θ for constant thickness nozzle under axial loading, attached to a spherical shell

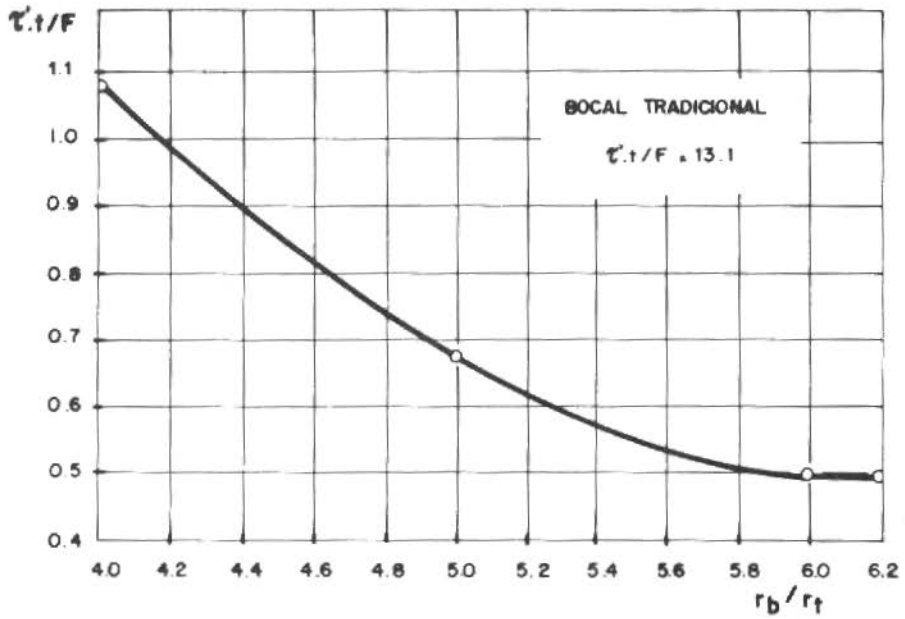

Figure 8. Maximum shear stress for axial loading. Constant thickness nozzle

It is interesting to note that for the case of internal pressure only, the "bending free shape" doesn't present advantages over the standard nozzle. Compared with the standard nozzle, the value of N_θ/pt is higher for the present shape, around 190 versus 155. The other forces fall within comparable values. In the Figure 9 the maximum shear stress for the "bending free shapes" is compared with the standard cases. For all values of r_b/r_t above 4.0 the new shape presents no advantages.

Finally if we combine the two cases as to simulate a real case of internal pressure in an equipment, it can be seen from Figure 10, that "bending free shapes" keep the stress levels bellow the corresponding ones forthe standard nozzle.

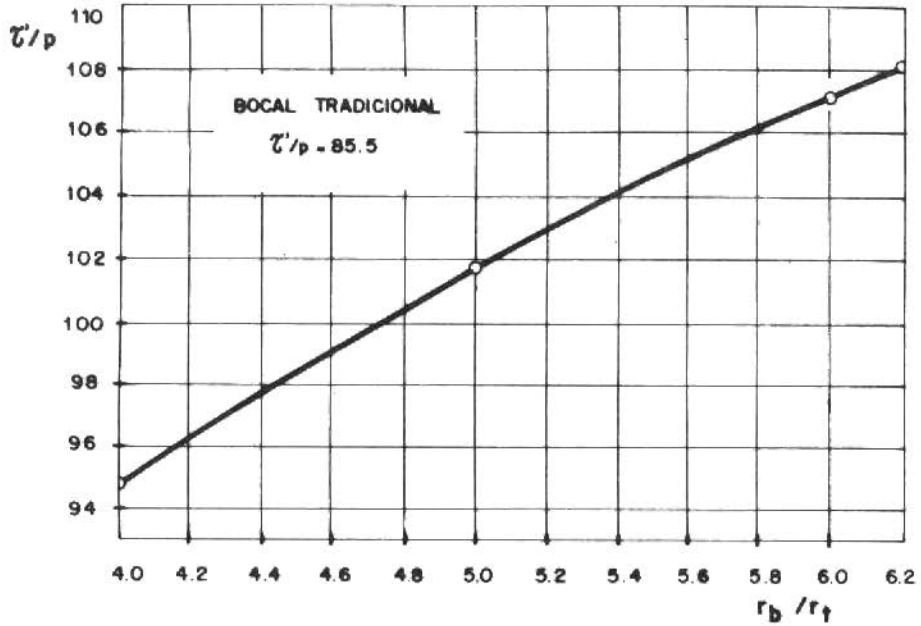

Figure 9. Maximum shear stress for internal pressure. Constant thickness nozzle

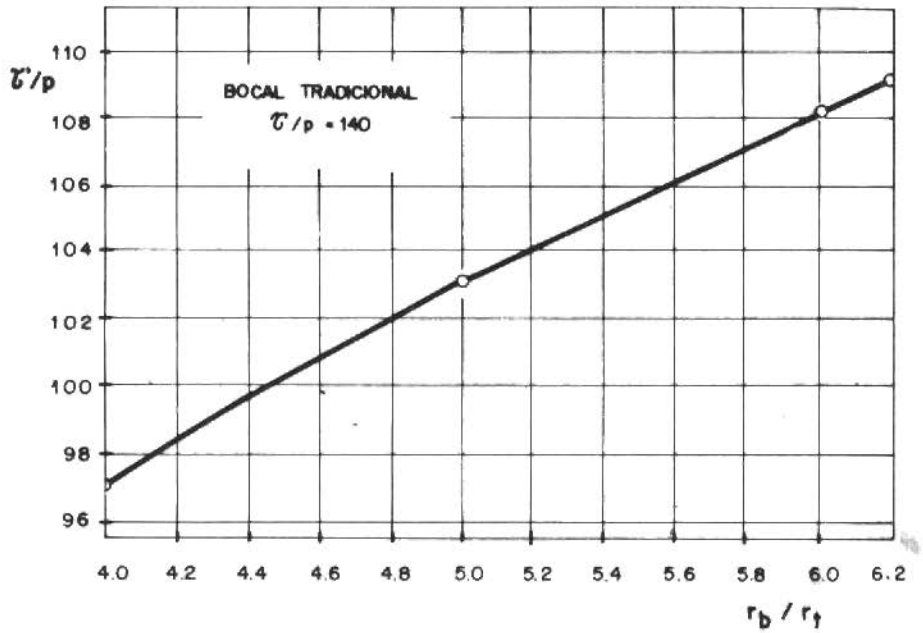

Figure 10. Maximum shear stress for internal pressure plus axial loading. Constant thickness nozzle

A second geometry, with variable thickness was also analysed. The thickness was assumed to vary linearly with the radius of curvature of the mean surface along the circumferential direction r_θ:

$$t = \frac{r_\theta - r_t}{r_e - r_t} (t_e - t_t) + t_t$$

where t_t and t_e are the thickness of the nozzle edges at the pipe and spherical shell end respectively; r_t and r_e the radius of the pipe and the spherical shell respectively. This geometry presented a much better performance as was shown in the reference [7].

For both cases, of an axial force and an internal pressure, the internal forces distribution is more uniform, mainly N_ϕ for the axial force, and are in average divided by two. The maximum reduced shear stress shown in Figure 11 for the case of internal pressure plus the corresponding axial loading, falls, for all values of $r_b = r_t$ higher than 4.0, well bellow the maximum shear stress for the standard nozzle.

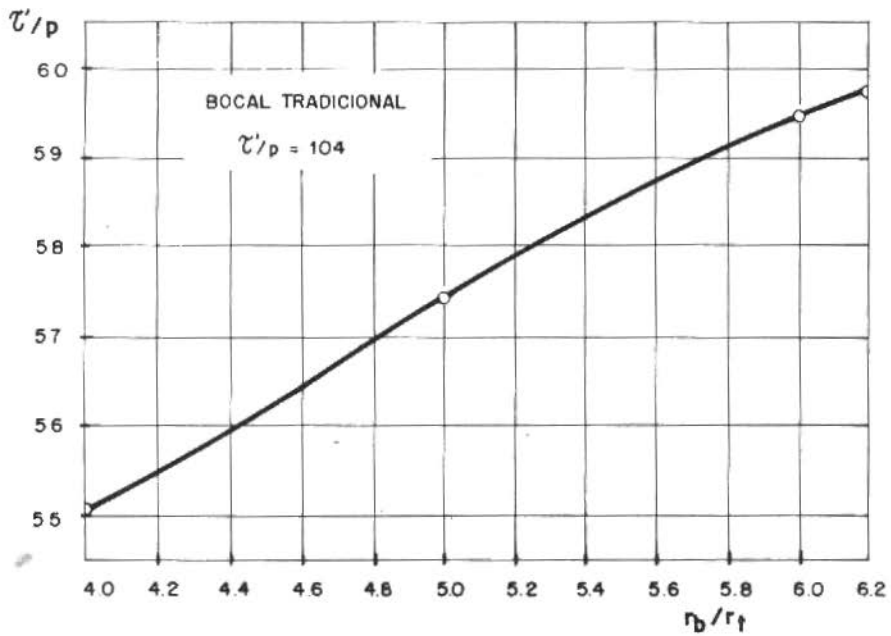

Figure 11. Maximum shear stress for internal pressure plus axial loading. Variable thickness nozzle

CONCLUDING REMARKS

The development of optimal shapes for axisymmetric nozzles and vessels was shown to be relatively easy to workout. The determination of the proper thickness variation and shape of the meridian curve can be carried through to match the real boundary condidions. Unfortunately a closed form solution is very difficult to come out due to the non-linearity of the governing equations. Nevertheless we find it worthwhile puting some effort in the qualitative discussion of the differential equations (7.a-b-c), to learn how the boundary conditions are controled through the variations of $g(\xi)$ and $h(\xi)$ or other adequated variable.

Also the choice of other conditions leading to a second differential equation involving σ, σ_ϕ, g and f is another possible approach, although it would discard the possibility of matching the desirable boundary conditions.

Other approaches to the optimization problem of nozzles have been published elsewhere, concerning mainly the optimum shape of the middle surface [9]. The problem of the bending free cross section for a thorus under special loading has also been handled [10].

ACKNOWLEDGEMENTS

The results presentedin this paper were developed in a research program supported by the FINEP under the research grant nº 5.1.82.0182.00. The presentation of this paper in the XVI IUTAM was made possible partially by the CNPq support under the grant nº 40.2081/84-EM.

REFERENCES

[1] ASME – Boiler and pressure vessel code. Section VIII, Division 1, ASME, New York, N.Y., 1974.

[2] Bijlaard, P.P. – Computation of the stress from local loads in spherical vessels or pressure vessel heads. Welding Research Council Bulletin, nº 34, March 1957, p.1-8.

[3] Bijlaard, P.P. – Stresses from local loads in cylindrical pressure vessels. Journal of Applied Mechanics, 77 (6) : 805, August 1955.

[4] Kraus, H. – Thin elastic shells. John Wiley & Sons, 1967.

[5] Flügge, W. – Stress in shells. John Wiley & Sons, 1967.

[6] Noronha Jr., D.B. e Bevilacqua, L. – Determinação da geometria de bocais para um comportamento de membrana predominante. I Simpósio Brasileiro

de Tubulações e Vasos de Pressão, Bahia, Novembro 1980.

[7] Noronha Jr., D.B. – Determinação de uma forma ótima para bocais radiais de vasos esféricos. M.Sc. Thesis, Departamento de Engenharia Mecânica, PUC/RJ, 1983.

[8] Kambe, E. – Differentialgleichungen, lösungsmethoden und lösungen. vol.1, Akademische Verlaggesellshaft, Leipzig, Germany, 1943.

[9] Hamada, M. – On the optimum shape of axisymmetric shells. IUTAM Symposium on Optimization in Structural Design, Warsav, 1973. Springer Verlag, Heidelberg, Berlim.

[10] Gray, W.H.; Stoddart, W.C.T. and Akin, J.E. – A derivation of bending free toroidal shell shapes for tokamak fusion reactor. Journal of Applied Mechanics, 46 : 120-124, Marc 1979.

ANÁLISE DE TENSÕES EM CURVAS TUBULARES SEGMENTADAS

Almir Silveira de Souza Filho
Arthur Martins Barbosa Braga
José Luiz de França Freire, Membro da ABCM
Deptº de Engenharia Mecânica - PUC/RJ

RESUMO

Este trabalho tem como objetivos o estudo e a comparação de soluções para a determinação da distribuição de tensões em curvas tubulares segmentadas sujeitas a momentos fletores no plano. Como modelo foi utilizado uma curva segmentada com ângulo de 180° composta por três gomos curtos e dois segmentos retos, formando um U. Três soluções para o problema foram estudadas: 1) Solução analítica de Kitching; 2) Solução pelo método de elementos finitos, utilizando elementos tipo casca; e, 3) Solução experimental baseada no método dos extensômetros elétricos.

ABSTRACT

The objective of this paper is to report the application of independent solution approaches to the determination of stress distributions in mitred curved pipes subjected to in plane bending moments. A U shaped model, built by welding three short straight segments and two long straight legs, was studied by the following three solution methods: 1) Theoretical solution proposed by Kitching; 2) Shell finite element; and, 3) Experimental solution with electrical resistance strain gages.

INTRODUÇÃO

No projeto de tubulações que interligam vasos de pressão, cuidados devem ser tomados quanto a prover os componentes de suficiente flexibilidade, garantindo que deslocamentos causados por va

riações de temperatura sejam absorvidos, mantendo níveis aceitáveis de esforços nos pontos de ancoramento. Dutos de grande comprimento e juntas de expansão podem proporcionar a requerida flexibilidade, mas o custo elevado deste tipo de solução aliado a problemas de espaço tornam necessária a utilização de dutos curvos. Dois tipos de curvas são empregados em sistemas de tubulação: curvas contínuas (Figura 1.a) e curvas compostas por segmentos retos (Figura 1.b). Por outro lado, enquanto o comportamento de tubos retos pode ser descrito com precisão através da teoria de flexão simples de vigas, o mesmo não ocorre com os dutos curvos, contínuos ou formados por trechos retos, cujas seções transversais sofrem ovalização. Em consequência do fenômeno de ovalização, as tensões longitudinais tornam-se superiores àquelas decorrentes da flexão simples e surgem tensões circunferenciais significativas, podendo ser superiores às longitudinais conforme as dimensões do duto.

A análise de tensões em curvas contínuas ou compostas por trechos retos é bastante complexa. Para estes tipos de tubulações não existem, ainda, soluções completas ou exatas para as distribuições de tensões e deformações. As teorias que tentam descrever o comportamento das curvas segmentadas baseiam-se na semelhança deste com o comportamento das curvas contínuas.

Zeno [1] em 1951, concluiu a partir de experimentos com curvas segmentadas sujeitas a flexão no plano, que a flexibilidade deste tipo de curva é comparável a de um tubo curvo liso. A mesma conclusão chegaram, também experimentalmente, Gross e Ford [2], Markl [3] e Lane e Rose [4]. Foi baseando-se nestas conclusões que Kitching [5,6], no início dos anos 60, propôs uma solução analítica para a flexão no plano de dutos curvos compostos por diversos trechos retos. Esta solução superpõe aos deslocamentos causados pela ovalização constante ao longo do gomo – típicos de curvas lisas – os efeitos localizados próximos à junção. Bond e Kitching [7] estudaram analiticamente, através da solução de Kitching, o comportamento de dutos gomados sob ação de pressão interna juntamente com momentos no plano e fora do plano. Jones e Kitching [8] desenvolveram uma solução analítica para a flexão no plano de dutos gomados simples (uma junção entre dois trechos retos), que já haviam sido estudados por Owen e Emmerson [9] através da fotoelasticidade tridimensional.

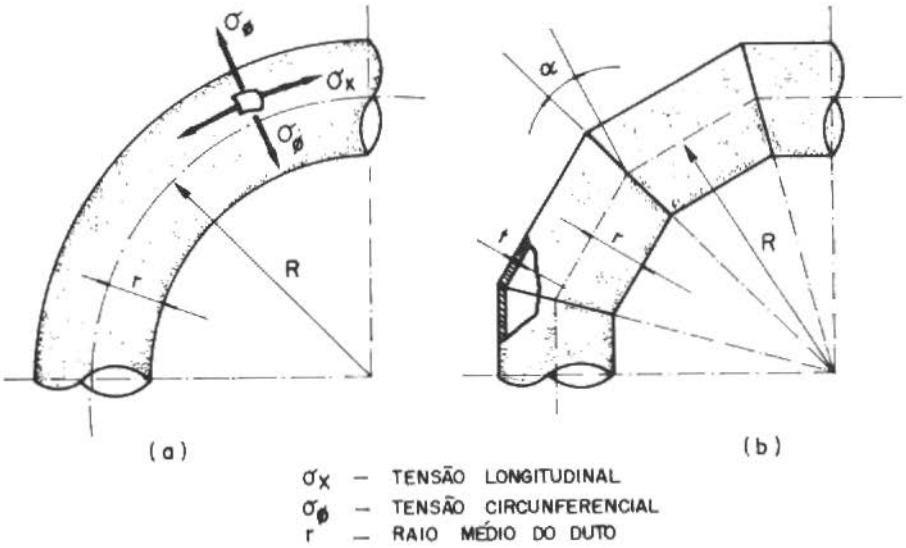

Figura 1. Curvas lisas (a) e curvas segmentadas (b)

Este trabalho originou-se de um estudo desenvolvido em cooperação pelo Departamento de Engenharia Mecânica da PUC/RJ com o Departamento de Tubulações da NATRON Consultoria e Projetos, onde o objetivo foi determinar as tensões que ocorrem em um sistema de tubulação que contém curvas gomadas e interliga um reator e um vaso de pressão de uma planta de produção de ácido fosfórico [10]. A discordância entre os resultados numéricos por elementos finitos e os encontrados via extensômetros elétricos num modelo reduzido levaram a recomendações finais de que modelos mais simples de curvas gomadas fossem estudados experimentalmente e analiticamente. O presente trabalho resulta destas recomendações e tem por objetivo fornecer subsídios ao projeto de sistemas de tubulação contendo curvas gomadas. Desta forma, uma curva segmentada com ângulo de 180^o composta por três gomos curtos e dois segmentos longos (Figura 2) foi analisada sob carregamento de flexão no plano. Três soluções para o problema foram estudadas: 1) Solução analítica de Kitching; 2) Solução pelo método dos elementos finitos a partir de elementos tipo casca; e, 3) Solução experimental baseada no método dos extensômetros elétricos resistivos. Os resultados obtidos foram também comparados com os fornecidos pela norma ASA B31.1 [11].

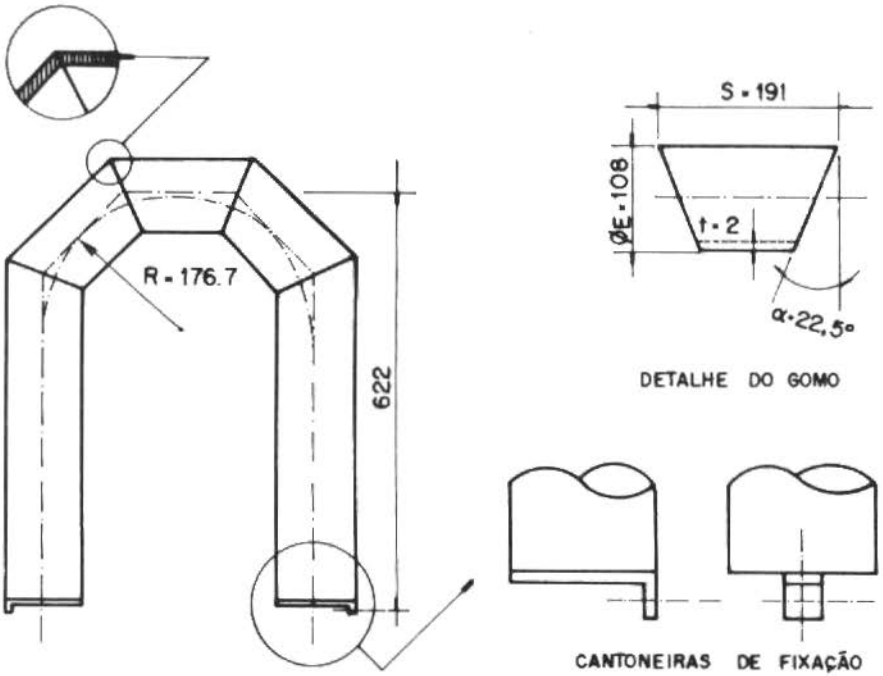

Figura 2. Modelo utilizado nas análise experimental, analítica e numérica

ANÁLISE PELO PROCEDIMENTO USUAL

Os procedimentos usuais de análise de tensões e cálculo de flexibilidades de tubulações que contêm curvas gomadas, se utilizam das semelhanças de comportamento entre estas últimas e as curvas lisas. A norma ASA B31.1 [11], por exemplo, assume que uma curva gomada pode ser substituída por uma curva lisa equivalente com mesmo diâmetro e espessura que o duto segmentado em questão. Para efeito de cálculos de flexibilidade e tensões de serviço, a curva equivalente tem um raio R_E dado pela expressão abaixo, onde a notação é a da Figura 1:

$$R_E = r \frac{(1 + \cotan \alpha)}{2} \qquad (1)$$

O fator característico para uma curva lisa é um parâmetro adimensional frequentemente utilizado na análise de flexibilidade des

tas curvas. Define-se este fator por:

$$\lambda = \frac{Rt}{r^2} \tag{2}$$

onde R é o raio da curva lisa (Figura 1.a). Desta forma, para uma curva gomada, pode ser definido o fator característico equivalente:

$$\lambda_E = \frac{(1 + \cotan \alpha)t}{2r} \tag{3}$$

Tubulações com curvas têm uma flexibilidade relativamente superior a dos dutos retos de igual perímetro, fato que decorre da ovalização que as seções transversais das primeiras sofrem em consequência de momentos no plano ou fora do plano. Para quantificar esta redução da rigidez à flexão dos tubos curvos, define-se o fator de flexibilidade. Assim, a rigidez à flexão de uma curva lisa pode ser dada por EI/K, onde EI é rigidez flexural de um tubo reto, com mesmo diâmetro e espessura, e K corresponde ao fator de flexibilidade, maior que a unidade. A norma A.S.A. fornece valores de K, baseados no trabalho de Clark e Reissner [12], que podem ser obtidos pela expressão:

$$K = \frac{1{,}65}{\lambda} \tag{4}$$

Esta norma fornece também valores empíricos [3] para o fator de flexibilidade de curvas gomadas:

$$K_E = \frac{1{,}52}{\lambda_E^{5/6}} \tag{5}$$

Outro parâmetro adimensional utilizado com frequência na análise de tensões em dutos curvos, é o fator de intensificação de tensões. Este é definido como sendo a razão entre a tensão de serviço e a tensão que ocorre em um duto reto de mesmo diâmetro e espessura, sujeitos a momentos fletores da mesma intensidade. Assim:

$$i = \frac{\sigma}{\sigma_n} \tag{6}$$

onde

$$\sigma_n = \frac{\overline{M}}{\pi r^2 t} \tag{7}$$

sendo σ a tensão de serviço e σ_n a tensão nominal para o momento fletor $\bar{M}$ que atua na seção.

Para curvas lisas o fator de intensificação de tensões, indicado pela norma ASA, é obtido por:

$$i = \frac{0,9}{\lambda^{2/3}} \tag{8}$$

Para dutos gomados, a mesma norma, fornece:

$$i_E = \frac{0,9}{\lambda_E^{2/3}} \tag{9}$$

Estas expressões são baseadas nos resultados experimentais obtidos por Markl [3], que realizou testes de fadiga em tubos curvos, lisos e gomados. Naquele trabalho, Markl comparou a vida de fadiga de dutos curvos com a de tubos retos comerciais. Tendo verificado um paralelismo entre os diagramas S × N de ambos os tipos de duto, Markl concluiu que um fator de intensificação de tensões único, independente do número de ciclos de projeto, poderia ser utilizado. Entretanto, a expressão (8) fornece fatores que são a metade dos obtidos analiticamente por Clark e Reissner [12] para as tensões circunferenciais máximas em curvas contínuas fletidas no plano. Estes últimos são dados por:

$$i_\phi = \frac{1,80}{\lambda^{2/3}} \tag{10}$$

para as tensões circunferenciais, e

$$i_x = \frac{0,84}{\lambda^{2/3}} \tag{11}$$

para as tensões longitudinais.

A "American Standard Association" optou por utilizar os resultados de Markl como fatores de projeto, tanto para curvas contínuas quanto para curvas segmentadas, sendo que para estas últimas este fator é calculado substituindo-se na expressão (8) o fator característico equivalente (λ_E). Esta decisão, baseou-se no fato de que a expressão (8) fornece valores que são próximos dos fatores de intensificação de tensões longitudinais, obtidos analiticamente por Clark e Reissner e dados pela expressão (11). Assim, uma vez que, para carregamentos estáticos, a integridade estrutural só é compro

metida quando ocorrem deformações longitudinais plásticas, ainda que já tenham ocorrido plastificações localizadas causadas por tensões circunferenciais elevadas [13], o fator de projeto dado pela expressão (8) pode ser empregado.

Para o duto analisado neste trabalho, cujo fator característico λ_E é 0,0644, os fatores K_E e i_E, calculados pelo procedimento recomendado pela norma ASA, são apresentados na seção de análise de resultados.

Neste trabalho, como será visto nas seções seguintes, três métodos foram empregados para a análise de tensões do duto mostrado na Figura 2. Para as análises experimental e numérica, os carregamentos aplicados sobre os seus respectivos modelos consistiram de esforços concentrados aplicados transversalmente às seções extremas da curva, de forma a fornecerem momento fletor uniforme ao longo do gomo central. Os fatores de flexibilidade para a curva, previstos por estes métodos de análise, foram obtidos pela expressão:

$$K = \phi_A \left[\frac{VR^2 + \pi/2\ VLR}{\pi r^3 t E} \right]^{-1} \qquad (12)$$

onde ϕ_A é a rotação calculada para a seção final do trecho reto do duto, seção A na Figura 3, e o termo entre colchetes corresponde à rotação desta seção prevista pela teoria de vigas curvas, quando o duto é carregado pelo esforço V; conforme mostrado na Figura 3.

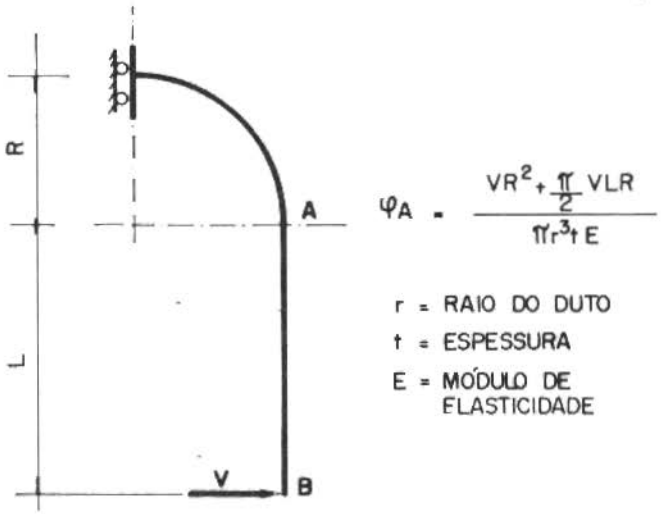

Figure 3. Modelo empregado no cálculo do fator de flexibilidade. A expressão para a rotação da seção A corresponde à calculada pela teoria de vigas

SOLUÇÃO ANALÍTICA

O comportamento sob carregamento de flexão no plano do duto gomado mostrado na Figura 2, objeto do presente trabalho foi analisado através da solução analítica de Kitching [5]. Esta solução, que utiliza a teoria de cascas elásticas como ferramenta matemática, foi proposta em 1965. Kitching descreveu a flexão no plano de curvas gomadas como sendo a superposição de dois campos de deslocamentos infinitesimais. Um deles varia unicamente com a direção circunferencial do duto, enquanto permanece constante ao longo da direção longitudinal, sendo típico da ovalização constante de curvas tubulares lisas. O segundo campo de deslocamentos corresponde a uma perturbação local, causada pela junção oblíqua, decaindo rapidamente a medida que o ponto estudado se afasta da extremidade do gomo. Este último é o maior responsável pelas diferenças de comportamento entre as curvas gomadas e as curvas lisas.

Os aspectos fundamentais da solução de Kitching [5] são apresentados abaixo:

1. Cada segmento da curva sofre ovalização constante, equivalente à de um tubo curvo quando submetido a momento no plano. O deslocamento radial pode ser descrito satisfatoriamente pelos três primeiros termos da série [5]:

$$\omega = \Sigma\, \omega_n \cos 2n\phi \qquad (13)$$

2. A partir da série acima, é obtida a expressão que fornece as deformações circunferenciais de flexão. Para uma rotação ϕ_0 nas junções oblíquas do gomo, é derivada a expressão das deformações longitudinais utilizando a hipótese de que o perímetro de uma seção transversal do duto permanece constante. Esta hipótese pode ser utilizada uma vez que as deformações circunferenciais de membrana são pequenas, quando comparadas com as demais.

3. Através da minimização da energia de deformação, são obtidos os parâmetros $\omega_n(\omega_1, \omega_2, \omega_3)$ da expressão (13). Uma observação importante é que, para o cálculo da energia de deformação, somente as parcelas das deformações correspondentes à ovalização constante foram consideradas, uma vez que as causadas por efeitos locais decaem rapidamente com o afastamento da junção.

4. Para a obtenção das deformações ocasionadas pelos efeitos localizados na junção, que deverão ser somadas às deformações de o-

valização constante, Kitching [5] supôs que o plano da junção dos gomos funcionasse como plano de simetria. Assim os esforços que anulam a rotação na junção do gomo de uma geratriz do tubo, fornecida pela análise de ovalização constante, são calculados. Desta forma as tensões na junção são determinadas e somadas às obtidas anteriormente.

Para o cálculo do fator de flexibilidade e das tensões circunferenciais e longitudinais para a curva da Figura 2, sujeita a momento fletor no plano, foi desenvolvido um programa de computador [14] que utiliza a solução analítica de Kitching. Os resultados fornecidos pelo programa MITER [14] são apresentados na seção de análise de resultados.

SOLUÇÃO NUMÉRICA

Uma análise numérica do problema foi realizada, tendo sido utilizado o elemento de casca isoparamétrico do programa ADINA[15], com 16 nós na superfície média da casca.

Com o intuito de minimizar o custo da análise numérica e otimizar o processo de obtenção de resultados, foram adotados os seguintes critérios para a modelagem através de elementos finitos:

i) Apenas 1/4 do duto foi analisado, aproveitando-se assim, a dupla simetria do problema. O restante da curva pôde ser simulado através de condições de contorno apropriadas.

ii) Levando-se em conta informações fornecidas pela solução analítica de Kitching, elementos de menor tamanho foram alocados no setor compreendido entre os ângulos de 90° e 130°, já que aí ocorre uma variação mais acentuada das tensões ao longo da direção circunferencial.

iii) Elementos menores foram utilizados nas regiões próximas às junções oblíquas, onde as tensões decaem rapidamente com a direção longitudinal.

iv) Para a parte reta do duto, que tem o comportamento semelhante ao de uma viga reta à flexão, utilizou-se um menor número de elementos.

Duas malhas de elementos finitos foram empregadas na análise do problema. A primeira malha utilizada, composta por 76 elementos e 754 nós, não forneceu bons resultados uma vez que foram encontradas algumas dificuldades para ajustar os valores do fator de flexibilidade e os fatores de intensificação de tensões. Este pri

meiro modelo numérico, entretanto, forneceu informações importantes que permitiram a construção de uma malha de elementos finitos que melhor modelou o problema. Esta última, que pode ser vista na Figura 4, contou com 106 elementos e 1024 nós. Para a sua implementação no computador, foi desenvolvido um programa para a geração automática deste tipo de malha. O programa ADINA pode fornecer as respostas para tensão tanto em pontos no contorno dos elementos quanto nos pontos de integração. Optou-se por utilizar a segunda opção de resposta, uma vez que as tensões calculadas nos pontos de integração se aproximam melhor dos valores reais [16]. Estes pontos não se encontram posicionados nas superfícies externa ou interna do elemento [15], de sorte que foi necessário desenvolver um programa de computador para extrapolar as tensões para os pontos nas paredes externa e interna do duto.

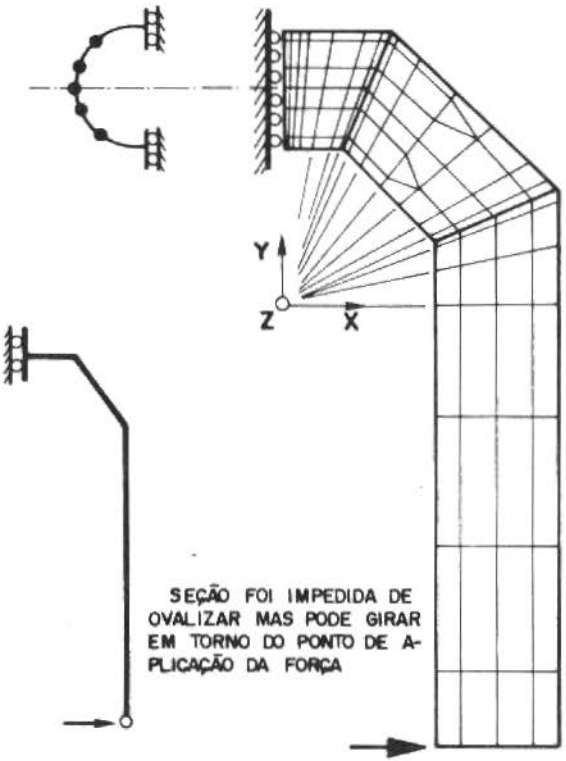

Figura 4. Malha de elementos finitos empregada na análise numérica. Foram utilizados 106 elementos de casca com 16 nós do programa ADINA

Para que se tornasse possível a comparação entre os resultados fornecidos pela análise via elementos finitos e os obtidos pelos dois outros métodos, analítico e experimental, optou-se por carregar o modelo numérico através de uma carga concentrada, aplicada na extremidade da curva, fornecendo momento fletor constante ao longo do gomo central do duto.

A rotação da seção final do trecho reto do tubo, seção A na Figura 3, utilizada para calcular o fator de flexibilidade através da expressão (10), foi obtida dividindo-se a diferença entre os deslocamentos na direção de aplicação da carga para as seções A e B (Figura 3) pelo comprimento do trecho reto do duto. Neste cálculo foi desprezada a flexão do trecho do duto compreendido entre as seções A e B.

Os resultados obtidos a partir da análise numérica são apresentados, juntamente com os fornecidos pelos demais métodos, na seção de análise e comparação de resultados.

SOLUÇÃO EXPERIMENTAL

O modelo utilizado na análise experimental por extensômetros elétricos foi construído a partir de um tubo de aço carbono sem costura. As dimensões do modelo se encontram na Tabela 1, onde a notação da Figura 2 é utilizada. Os gomos foram usinados separadamente e unidos com solda oxi-acetilênica. Procurou-se dar à junção soldada um acabamento de forma a delinear bem as arestas dos gomos, condição importante para permitir semelhança com a modelagem analítica do problema. Ainda assim, o acabamento da região próxima a junção soldada não foi plenamente satisfatório.

Tabela 1. Dimensões do modelo experimental

α	R(mm)	r(mm)	t(mm)	E(GPa)	ν
25,5°	177	53,0	2,0	209	0,273

Para as medidas de deformação foram utilizados extensômetros elétricos resistivos uniaxiais com comprimentos úteis de 3,2mm (FAE 12 - 12 - S6EL) e de 0,79mm (FAE - 03 - 12 - S6EL), ambos produzidos pela BLH-Eletronics. Os primeiros, em número de 22, foram instalados

aos pares na superfície externa do gomo central, fornecendo medidas das deformações longidutinais e transversais. Em mesmo número que os anteriores e fornecendo medidas das mesmas deformações, os extensômetros de 0,79mm foram colados na junção oblíqua da parte central. Tendo em vista que as análises numérica e analítica evidenciaram anteriormente uma acentuada variação das tensões na região compreendida entre os ângulos ϕ de 90^{o} e 130^{o}, maior número de extensômetros foram colados nesta região. Na Figura 5 é mostrado em detalhe a parte central da curva, onde os extensômetros foram posicionados. Com a finalidade de verificar a concordância entre as direções principais de tensão previstas pela solução analítica, numérica e as experimentais, foram realizadas medições em dois pontos ao longo da junção oblíqua do gomo através de extensômetros de 3,2mm, montados em forma de roseta triangular. Através de seguidas repetições dos testes, todos os extensômetros puderam ter suas deformações lidas, para valores determinados de carga, por duas pontes de Wheatstone modelo Vishay BAM - 1B auxiliadas por um conector de 10 canais modelo Vishay SB - 1.

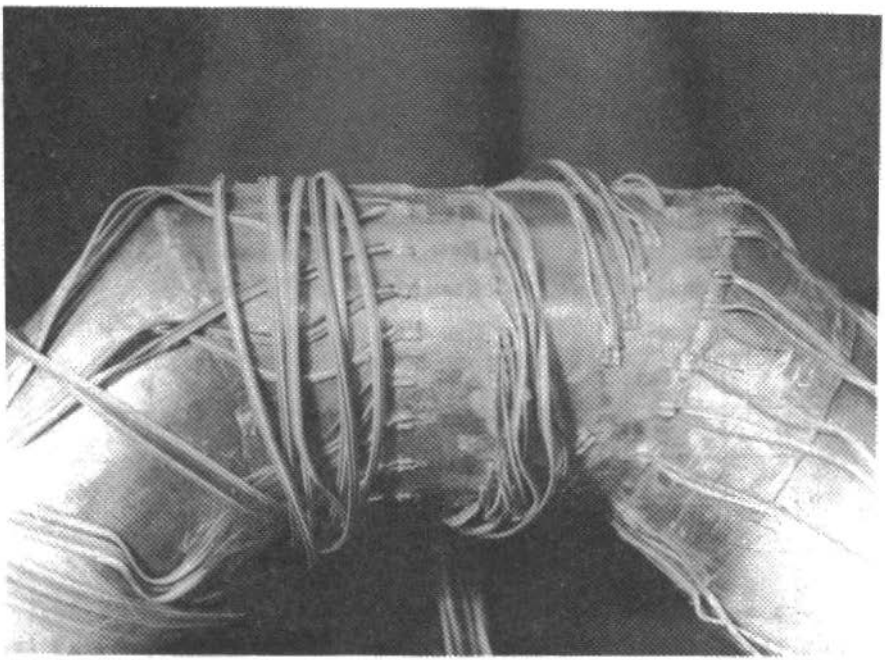

Figura 5. Posicionamento dos extensômetros

Para a realização dos experimentos foi utilizado um equipamento INSTRON 1125. Aos reforços em forma de L, soldados nas extremidades da curva, foram aparafusados pinos que permitiram a fixação do modelo à máquina. Na Figura 6 pode ser visto o sistema de carregamento. O pino superior foi ligado à célula de carga, fixada no travessão móvel da máquina, através de uma junta universal. Este procedimento teve a finalidade de permitir a rotação da seção onde o carregamento foi aplicado. De modo a evitar que o peso próprio do duto provocasse uma rotação acentuada desta seção, concentrando esforços na fixação inferior, foi providenciado um apoio para a parte em balanço. Uma vez que a solicitação foi efetuada por incrementos e o experimento foi realizado dentro dos limites de pequenos deslocamentos, a medida das variações de deformação permitiu o desacoplamento dos efeitos de peso próprio e dos causados pela montagem do modelo ao sistema de carregamento.

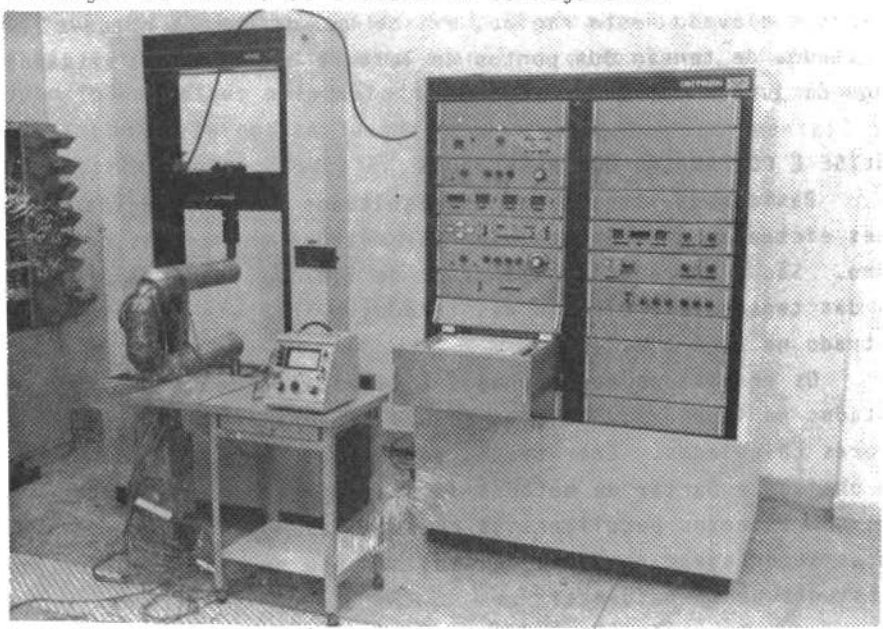

Figura 6. Sistema de carregamento

Além dos extensômetros, relógios comparadores foram utilizados nos ensaios para medir as deflexões da extremidade do duto (seção B - Figura 3) e da seção final da parte curva do modelo (seção A). A diferença entre estes deslocamentos dividida pelo comprimento da parte reta do modelo (445,3mm), forneceu o valor da rotação

da seção final da curva. Esta rotação substituída na expressão (12), permitiu o cálculo dofator de flexibilidade experimental. Este valor é apresentado na Tabela 2, na seção seguinte.

Os fatores de intensificação de tensões obtidos experimentalmente são apresentados na próxima seção, nas Figuras 8 e 9, juntamente com os calculados pelos outros métodos. As direções principais de tensão para as posições 45^{0} e 120^{0} da seção oblíqua da junção do gomo central, obtidas das deformações acusadas pelos conjuntos de extensômetros montados em forma de roseta triangular, apresentaram desvios em relação àquelas previstas através da solução analítica de Kitching. Certamente, a posição de colagem das rosetas improvisadas contribuiu para este desvio. Em consequência do mau acabamento da região próxima ao cordão de solda, os extensômetros só puderam ser colados a distâncias de 3 a 5mm da seção oblíqua. A estas distâncias da junção, uma vez que o decaimento das tensões é elevado nesta região, existe uma diferença razoável entre os estados de tensão dos pontos de leitura e dos pontos situados ao longo da junção oblíqua.

ANÁLISE E COMPARAÇÃO DOS RESULTADOS

Basicamente três tipos de resultados foram extraídos das análises efetuadas através dos diversos métodos empregados neste trabalho. São eles relativos ao fator de flexibilidade, à distribuição das tensões e à direção das tensões principais no duto gomado mostrado na Figura 2.

Os resultados relacionados à flexibilidade do duto são apresentados na Tabela 2. Observa-se uma pequena discrepância entre os fatores calculados. Entretanto, ao se levar em conta que estes foram obtidos a partir de métodos de análise totalmente independentes, com aspectos peculiares às respectivas modelagens, estas diferenças se encaixam na faixa de espalhamento de resultados esperada em estudos desta natureza.

Tabela 2. Fatores de flexibilidade

ANÁLISE	K
Kitching	10,9
El.Finitos	12,2
Ext. Elétricos	11,6
ASA B31.1	14,9

A principal diferença entre o modelo analítico e os modelos experimental e numérico, reside no tipo de carregamento empregado para solicitar o duto. O modelo analítico de Kitching pressupõe que a curva seja composta por diversos gomos, todos iguais, e que o carregamento de flexão no plano seja uniforme ao longo de todo o duto. Esta imposição é que permite supor que a extremidade oblíqua do gomo trabalhe como plano de simetria. Por outro lado, quando se aplicou aos modelos experimental e de elementos finitos uma carga concentrada na extremidade da curva, permitiu-se que o momento fletor, nos demais gomos que não o gomo central, variasse de ponto a ponto. Outro aspecto importante, relativo às diferenças entre os resultados numéricos e experimentais, é a não simetria, em relação à seção central da curva, do modelo experimental. A Figura 7 mostra de forma esquemática as condições de contorno impostas pela forma de fixação do mesmo à máquina de ensaios. Por razões de economia, uma vez que um estudo por elementos finitos através de uma malha que reproduzisse todo o duto tornaria a análise muito cara, somente 1/4 do duto foi modelado pelo método numérico, de forma que o carregamento simétrico tornou-se levemente diferente do experimental, como pode ser visto na Figura 7.

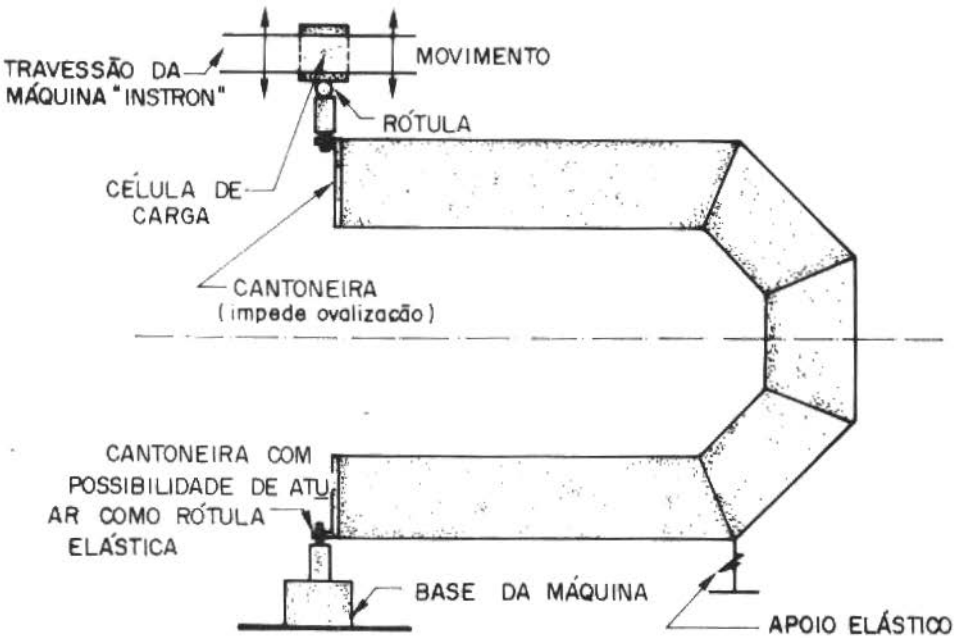

Figura 7. Esquema de carregamento do modelo experimental

Quanto à norma ASA B31.1 que foi também utilizada para fornecer um fator de flexibilidade para a curva analisada, ela se baseia em resultados empíricos, sujeitos a desvios conforme as particularidades dos experimentos que os forneceram. Se o desvio padrão for adotado como medida da variação dos fatores de flexibilidade obtidos neste estudo, este se encontra na faixa de 5,6% em relação a média, quando não se leva em conta o fator fornecido pela norma.

O segundo tipo de resultado obtido neste trabalho, refere-se à distribuição das tensões. As Figuras 8 e 9 apresentam a variação dos fatores de intensificação de tensões, circunferenciais e longitudinais, para a seção central do duto e para a seção oblíqua da extremidade do gomo central. Uma análise da Figura 8 revela a acentuada concordância entre os resultados experimental e numérico para a seção central. A solução de Kitching prevê uma distribuição de tensões bem próxima destas últimas, verificando-se entretanto, uma pequena defasagem no posicionamento dos picos de tensão.

Para a seção oblíqua na junção do gomo, não se observou a mesma proximidade entre os resultados experimental e numérico, verificada anteriormente na seção central da curva. Para as tensões circunferenciais externas os valores das tensões citadas acima, ainda estão bem próximos. Entretanto, para as tensões longitudinais externas, a discrepância entreos valores numérico e experimental chega a 50% para um ângulo de 120^{o}. Este fato não causa estranheza quando se leva em conta que os extensômetros, no modelo experimental, têm um comprimento útil finito e não foram colados exatamente na junção dos gomos. A Figura 10 apresenta a variação das tensões longitudinais com a distância ao plano oblíquo da extremidade do gomo, fornecida pela análise por elementos finitos. Nota-se claramente o acentuado decaimento destas tensões com o afastamento da junção, principalmente para a posição relativa a $127,5^{o}$, onde foi observada a maior diferença entre os resultados experimental e numérico. Além disso, o mau acabamento da junção soldada contribuiu para que não fosse reproduzido pelo modelo experimental o que houvera sido previsto a partir da análise numérica. A distribuição das tensões calculadas através do método analítico de Kitching, não se afastou muito das fornecidas pelos dois outros métodos. Este fato encontra explicação na diferença do tipo de carregamento utilizado para solicitar os modelos empregados neste estudo, aspecto que já

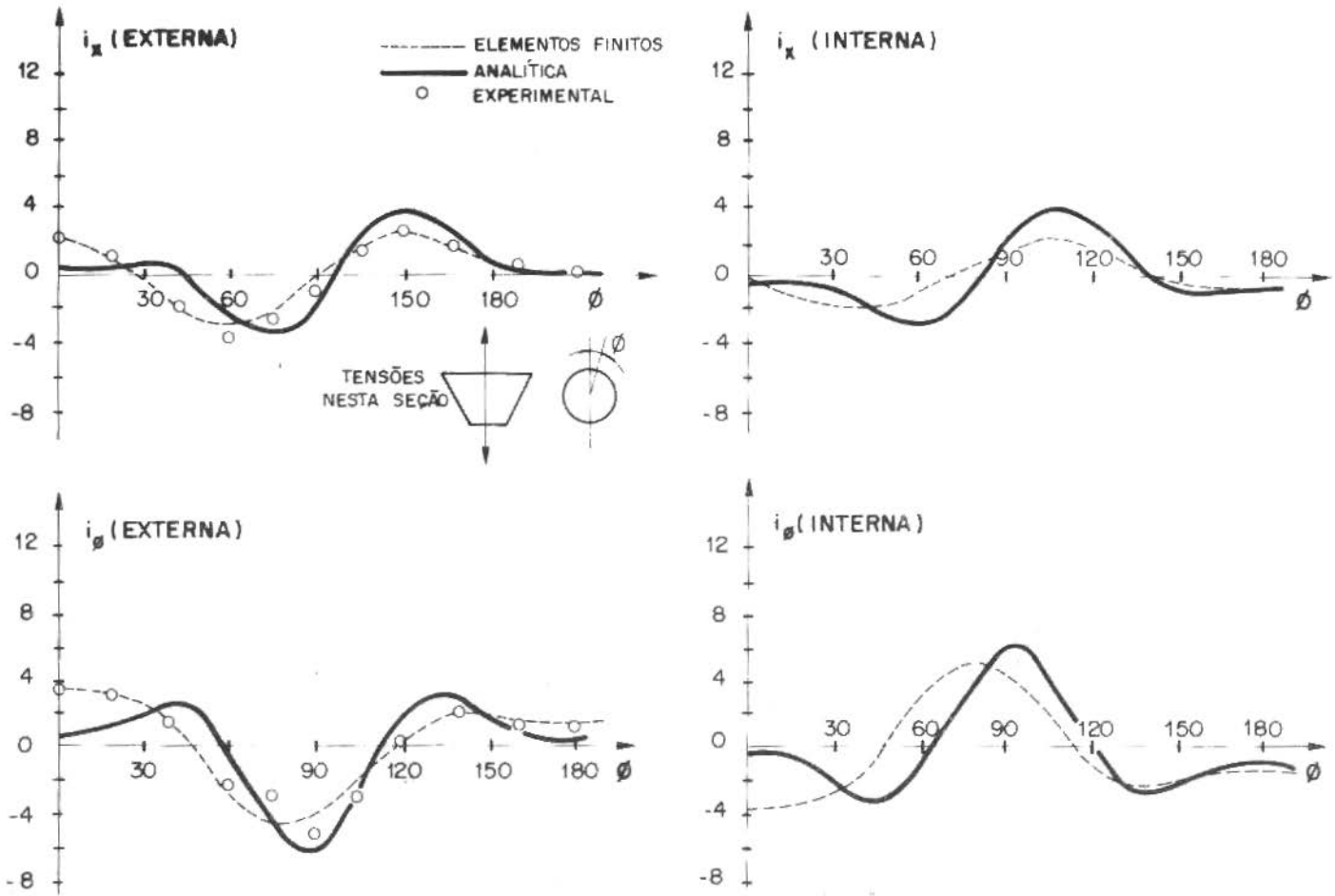

Figura 8. Tensões no gomo central

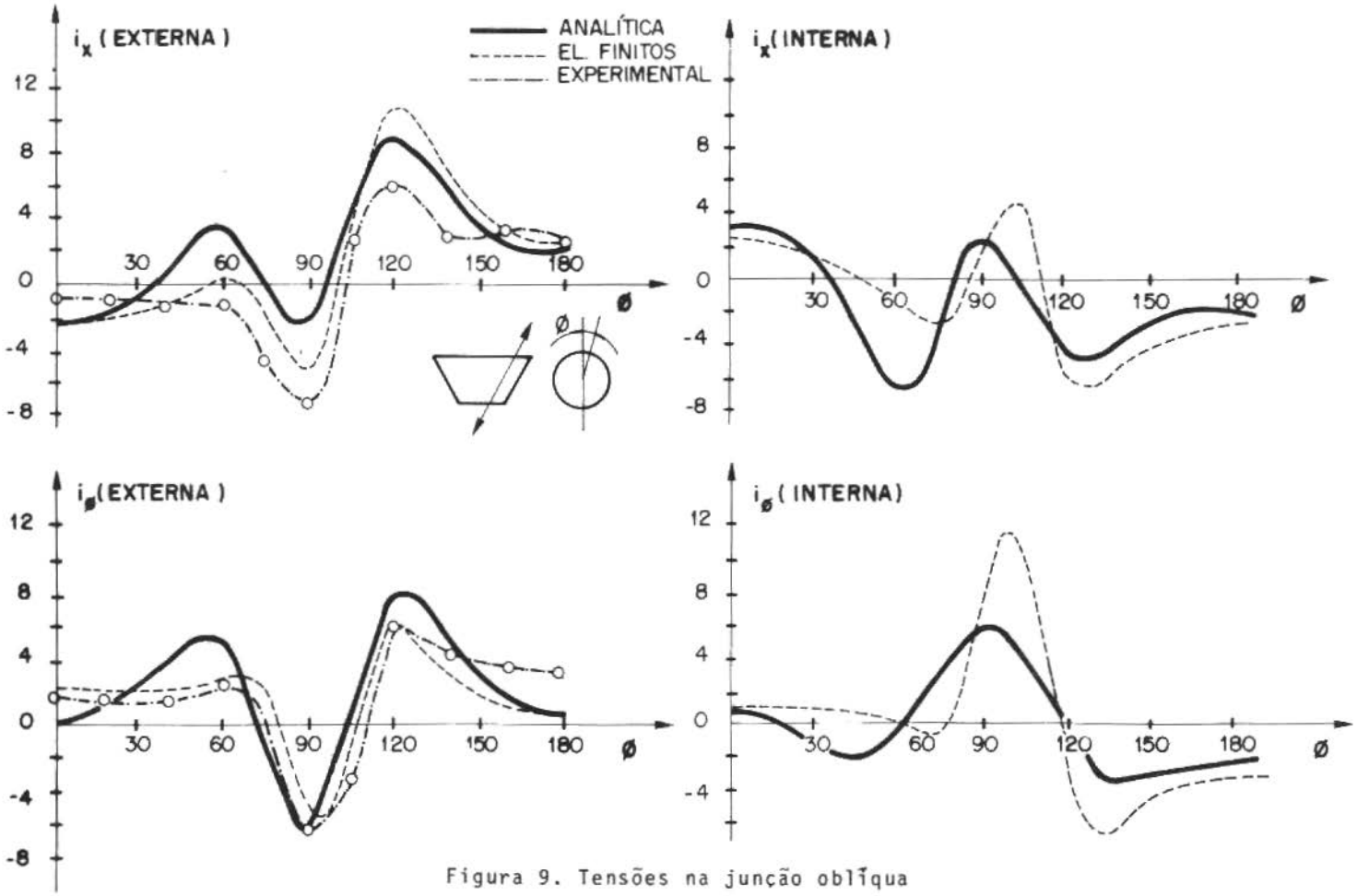

Figura 9. Tensões na junção oblíqua

foi discutido anteriormente. Desta forma, diferenças da ordem de 45%, como foi verificada entre as tensões circunferenciais internas máximas, numérica e analítica, na junção do gomo, não invalidam os resultados obtidos neste trabalho.

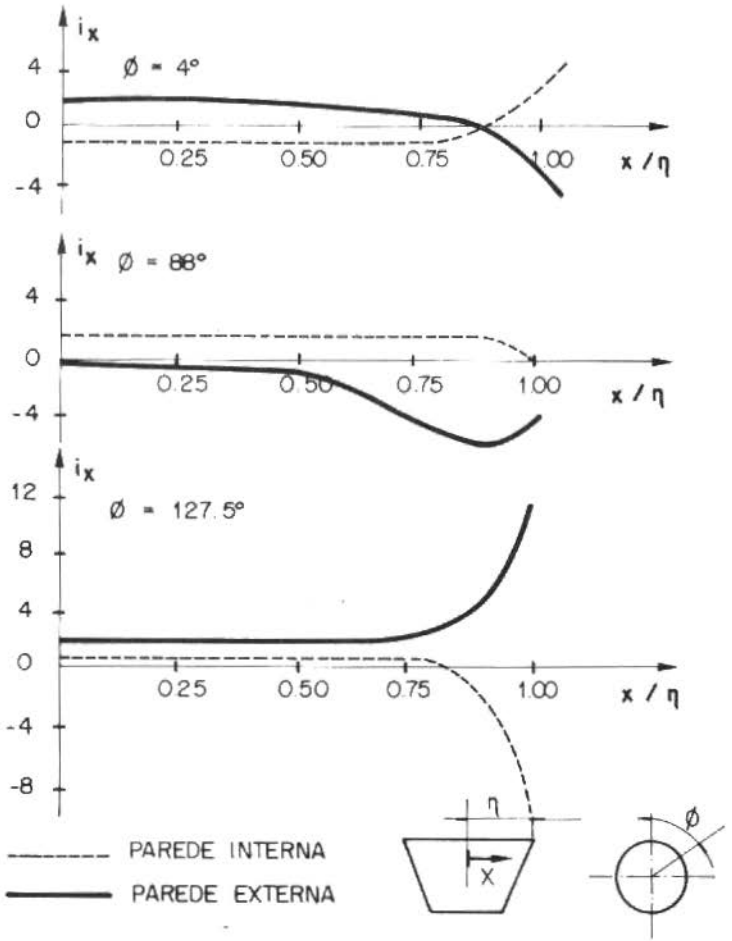

Figura 10. Variação das tensões longitudinais ao longo do gomo

A Tabela 3 apresenta os fatores de intensificação de tensões máximos obtidos através dos diversos métodos de análise aqui empregados. Além destes, a tabela mostra também os fatores fornecidos pela norma ASA B31.1, calculados pela expressão (9), e os previstos por Clark e Reissner [12] que foram obtidos substituindo-se o fator

característico equivalente (λ_E) nas expressões (10) e (11). Observa-se que o fator calculado pela norma é inferior aos obtidos através dos outros métodos. Este fato não causa surpresa uma vez que, como já foi discutido anteriormente, a norma indica um fator de projeto que é a metade do fator analítico de Clark e Reissner para as tensões circunferenciais. Este último, como é visto na Tabela 3 está bem próximo do fator experimental. Entretanto, deve sempre ser lembrado que tanto o fator da norma quanto os fatores previstos por Clark e Reissner são baseados em resultados para curvas contínuas, o que justifica as diferenças com os demais resultados.

Tabela 3. Fatores de intensificação de tensões

ANÁLISE	SUP. INTERNA		SUP. EXTERNA	
	i_ϕ	i_x	i_ϕ	i_x
Kitching	6,2	-6,6	7,5	9,1
El. Finitos	11,8	-7,0	6,5	12,0
Ext. Elétricos	–	–	7,0	8,0
ASA B31.1	5,6			
Clark e Reissner	11,2	–	–	5,2

A Figura 11 mostra a variação das direções principais de tensão ao longo da junção oblíqua do gomo central. Os valores na ordenada do gráfico representam os ângulos formados pela direçao de tensão principal máxima e a direção circunferencial. Os valores numéricos são bem próximos dos previstos pela solução analítica, a não ser para a região próxima a ϕ igual a 90^0, onde algumas perturbações foram observadas. Os resultados experimentais podem ser considerados satisfatórios, apesar de terem apresentado algum desvio, cujas prováveis causas já foram discutidas anteriormente, na seção relativa à análise experimental.

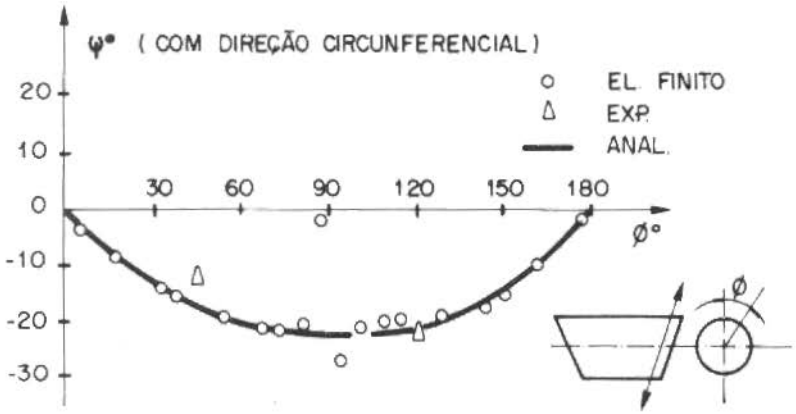

Figura 11. Direções principais ao longo da junção oblíqua

CONCLUSÃO

O presente trabalho faz parte de um programa extenso sobre o comportamento de dutos segmentados submetidos a esforços de flexão no plano. Sua motivação principal originou-se de um trabalho anterior [10] que procurou determinar tensões e deformações num duto com curvas gomadas através dos métodos de elementos finitos e extensômetros elétricos. Como os resultados finais foram discrepantes, sugeriu-se o estudo de um modelo de curva gomada mais simples que pudesse ser analisada pelos métodos experimental e numérico bem como pelo método analítico de Kitching. Assim, as limitações, vantagens e desvantagens de cada método poderiam ser comparadas e analisadas. Outro aspecto importante foi permitir que se tenha uma noção dos desvios apresentados pelas soluções de Kitching e de elementos finitos com relação à solução experimental por extensômetros elétricos. Isto proporcionará a previsão de distribuições de tensões e de fatores de flexibilidade em novos projetos com maior confiabilidade.

Ao final deste trabalho pode-se concluir que:

i) O efeito de ovalização, como já era esperado, mostrou-se importante na flexão do duto gomado estudado, mostrando que a teoria de vigas, tal como empregada no chamado cálculo de flexibilidade de tubulações, não prevê com segurança a flexão destas curvas.

ii) Os resultados obtidos pelos diversos métodos, apesar de

algumas diferenças quanto aos valores exatos das tensões máximas e levando-se em conta os aspectos específicos de cada modelagem, mostraram uma mesma tendência. Desvios pequenos, da ordem de até 15%, ocorrem na região central dos gomos. Para o plano oblíquo da junção desvios maiores foram observados chegando até 45%. No entanto, as tendências apresentadas pelos três métodos de análise foram as mesmas, mostrando que as diferenças entre os valores dos picos de tensão se devem aos problemas específicos da modelagem de cada método. As tensões máximas ocorreram na junção dos gomos, na região compreendida entre 90^{o} e 130^{o}.

iii) A solução de Kitching pode ser utilizada com segurança no projeto de tubulação que contenham curvas gomadas, uma vez que pelo menos para o modelo aqui estudado, os resultados por ela previstos são próximos dos obtidos através dos outros métodos.

iv) A análise numérica através de elementos finitos fornece bons resultados, desde que um número suficiente de elementos seja utilizado. Porém, é um método caro quando se utiliza elementos de casca, devendo ser empregado em casos esporádicos quando dúvidas importantes precisam ser esclarecidas. Um elemento finito específico, para uma análise rápida e mais econômica de tubulações gomadas, foi recentemente desenvolvido [17] e deve ser utilizado para projetos de dutos complicados envolvendo muitas curvas. A análise com elementos de casca e através dos métodos empregados neste trabalho serviram então como uma verificação para validar este novo elemento.

v) A concordância satisfatória entre a análise experimental utilizando extensômetros elétricos e defletômetros com a análise realizada através dos dois outros métodos – analítico e numérico – para o modelo de curva gomada simples estudada, permite concluir que resultados confiáveis e compatíveis poderão ser obtidos em problemas mais complexos, tal como aquele estudado em [10].

Como conclusão final, pode-se destacar que os resultados obtidos pelos diversos métodos apresentaram concordância satisfatória levando-se em conta as dificuldades inerentes a cada método no que se refere à aplicação de esforços, à imposição de condições de contorno similares e às suas próprias limitações.

AGRADECIMENTOS

Os autores agradecem ao Departamento de Engenharia Mecânica da PUC/RJ e à NATRON Consultoria e Projetos o suporte técnico e fi

nanceiro e, em particular, ao Prof. Carlos Alberto de Almeida e aos Engenheiros José Luiz de França Filho, Cid do Nascimento Silva e Cláudio Patrone Monteiro de Barros pelo apoio e as discussões que permitiram o desenvolvimento do programa de pesquisa do qual este trabalho faz parte.

REFERÊNCIAS

[1] Zeno, D.R. – Trans. ASME, 73 : 64-67 (1951).

[2] Gross, N. and Ford, H. – The flexibility of short-radius pipe bends. Heat and Air Treat. Engrs., 16 : 152-155, 197-200, 210-216 (1953).

[3] Markl, A.B.C. – Fatigue tests of piping components. Trans. ASME, 74 : 287--303 (1952).

[4] Lane, P.H.R. and Rose, R.T. – Experiments on fabricated pipe bends. Brit. Weld. J., 9 (6) : 323 (1961).

[5] Kitching, R. – Mitre bends subjected to in-plane bending moments. Int. J. Mech. Sci., 7 : 551 (1965).

[6] Kitching, R. – In-plane bending of a 180° mitred pipe bend. Int. J. Mech. Sci., 7 : 721 (1965).

[7] Bond, M.P. and Kitching, R. – Multi-mitred pipe bends subjected to internal pressure combined with external loadings. J. Strain Analysis, 7 (2) (1972).

[8] Jones, N. and Kitching, R. – An experimental investigation of a right--angled single unreinforced mitred-bend subjected to various bending moments. J. Strain Analysis, 1 : 248 (1966).

[9] Owen, B.S. and Emmerson, W.C. – Elastic stresses in single mitred bends. J. Mech. Engr. Sci., 5 : 303 (1963).

[10] França Fº, J.L.; Campos, M.; Freire, J.L.F. e Vieira, R.D. – Um caso prático de análise de tensões para dutos com curvas gomadas. Revista Brasileira de Ciências Mecânicas, V (3) : 5-23 (1983).

[11] American Standards Association B31.1 – American Standard Code for Pressure Piping. (1967).

[12] Clark, R.A. and Reissner, E. – Bending of curved tubes. Adv. in Appl. Mechs., 2 : 93-122, Academic Press (1951).

[13] The M.W. Kellog Company – Design of Piping Systems. 2nd ed. rev., John Wiley, N.Y., (1965).

[14] Souza Fº, A.S. – Análise de tensões em tubos curvos compostos por trechos retos. Tese de Mestrado, Departamento de Engenharia Mecânica, PUC/RJ, Maio 1984.

[15] Bathe, K.J. – ADINA - A Finite element program for automatic dynamic in-

cremental non linear analysis. Report 82448-1, Acoustic and Vibration Laboratory, Dep. of Mech. Engr. Cambridge, Mass., 1975 (Rev. Dec. 1978).

[16] Bathe, K.J. – Finite elements procedure in engineering analysis. Prentice-Hall, N.J. (1982).

[17] Salles, A.C.S.L. – Análise de tubos segmentados utilizando modelos de vigas - Via método dos elementos finitos. Revista Brasileira de Ciências Mecânicas, VII (1) : 304-322 (1985).

ANALYSES OF PIPE MITRED BENDS THROUGH A MODIFIED BEAM MODEL – F E APPROACH

Carlos Alberto de Almeida, Membro da ABCM
Angela Cristina Souza Leão de Salles
Deptº de Engenharia Mecânica - PUC/RJ

ABSTRACT

The formulation of a recently proposed displacement-based straight pipe element for the analysis of pipe mitred bends is summarized in this paper. The element kinematics includes axial, bending, torsional and ovalisation displacements, all varying cubically along the axis of the element. Interaction effects between angle adjoined straight pipe sections are modeled including the appropriate additional strain terms in the stiffness matrix formulation and by using a penalty procedure to enforce continuity of pipe skin flexural rotations at the common helical edge. The element model capabilities are illustrated in some sample analyses and the results are compared with other available experimental, analytical or more complex numerical models.

RESUMO

Este trabalho apresenta a formulação de um elemento recentemente proposto à análise de tubos curvos segmentados. A formulação do elemento inclui os deslocamentos axial, de flexão, de torção e de ovalisação, todos interpolados cubicamente ao longo do eixo longitudinal do tubo. Os efeitos da interação entre tubos retos adjacentes são modelados incluindo-se na matriz de rigidez as deformações correspondentes, e utilizando-se um método de penalidades para garantir a continuidade das rotações devido à flexão da casca ao longo da seção comum aos tubos. As possibilidades e limitações do modelo são ilustradas em algumas análises e os resultados comparados com soluções de outros modelos experimentais, analíticos ou de formulação numérica mais complexa.

INTRODUCTION

The structural integrity and cost of pipelines are of major concern in nuclear, oil, chemical and other industrial plants. Due to its great flexibility, curved sections formed by mitring and welding together straight thin-walled pipe sections occur quite frequently in piping systems and are required to support severe thermal, seismic, and other mechanical loads. For these reasons, an increasing amount of attention has been given to their analysis [1-3].

Because of the importance and dificulties that lie in the analysis and design of pipe mitred bends, much research has been devoted to the study of their structural behavior. In these investigations, during recent years, various simple to complex analytical and numerical models of mitred bends have been proposed [2-5]. However, these structural models presented some limitations either with regard to their accuracy in predicting displacements and stresses or the cost of using them. In essence, these models use general shell theory to describe the behaviour of the mitred bend. Green and Emmerson in Ref.[6] obtained a solution for two long straight pipes rigidly joined to form a bend subjected to internal pressure on in-plane bending. Similar procedures for the same problem were obtained by van der Neut [7] using thin shell theory. Both analysis, however, were restricted to small angles of intersection. Jones and Kitching [8], using the minimization of the strain energy, evaluated the overall flexibility and load deformation of a discontinuous pipe bend in a manner similar to that employed by von Kārmān for the smooth pipe bend [9]. Short damping length deformation terms were introduced in the formulation to satisfy the continuity and equilibrium conditions between pipes at the common edge, and the results compared well to experiments except for large angles.

The greatest potential for general analysis of pipe mitred bends lies on the use of the finite element method. In theory, either three-dimensional or general shell elements can be employed to model any pipe bend very accurately by using a fine enough finite element mesh. However, in practice, such an analysis of a single bend requires of the order of a thousand finite element equilibrium equations that need be operated upon, which means that the linear analysis of an assemblage of pipe mitred bends can be prohibitively expensive.

In order to reduce the number of finite element variables, special beam-shell elements have been recently proposed for smooth pipe bends [10,11]. The purpose of this paper is to extend the beam-shell element formulation for the analysis of discontinuous pipe bends. The element is a four node displacement-based finite element with axial, torsional, and bending displacements and the von Kārmān ovalisation deformations all varying cubically along the element length. Modifications in the element beam displacement equations and in the interaction conditions between joining elements are introduced in the original pipe formulation to satisfy the element boundary conditions at the angled edge section. Also, the compatibility between shell mid-surface displacements of elements joining at the oblique edge is enforced through a penalty procedure.

In the next section of this paper we discuss the amendments in the basic beam-shell formulations so that the element is applicable to the modelling of pipe mitred bends. In the presentation we assume that the reader is familiar with the early beam-shell formulation presented in Refs.[10-12,14], and we concentrate only on the additional evaluations. The formulation has been implemented in the computer, and in Section 3 the numerical results obtained for the analyses of two pipe mitred bends are compared with available numeric and experimental solutions [13].

PIPE MITRED ELEMENT FORMULATION

As in the basic elbow pipe element, which was formulated using the displacement-based finite element method, the essential ingredientes of the pipe mitred element formulation are the specific displacement assumptions used and the strain and stress components included in the evaluation of the element strain energy. Therefore, in the following sections, we concentrate on the element kinematic and constitutive assumptions used in the formulation.

Element Geometry and Displacement Interpolations

The basic assumption of the formulation is that the total displacement of any point in the element is the sum of two sets of displacement fields. First, axial, torsional and bending displacements, all varying cubically along the lenght of the pipe, are referred to the element center line displacements through a

local coordinate system r,s,t. Considering the element in Fig. 1, the coordinates of a point in the element before and after deformation can be written as

$$ {}^{\ell}x_i(r,s,t) = \sum_{k=1}^{4} h_k\left[{}^{\ell}x_i^k + t\, a_k\, {}^{\ell}V_{ti}^k + s\, a_k\left({}^{\ell}V_{si}^k + \tan\alpha_k\, {}^{\ell}V_{ri}^k\right)\right], \quad i = 1,2,3 \tag{1} $$

where

r,s,t = isoparametric coordinates [15],

${}^{\ell}x_i$ = Cartesian coordinate of a material point (r,s,t)

$h_k(r)$ = isoparametric interpolation functions, see Fig. 1,

${}^{\ell}x_i^k$ = Cartesian coordinate of a nodal point k,

a_k = element outer radius at node k,

α_k = oblique section angle at node k,

${}^{\ell}V_{ri}^k$ = i-th component of unit vector ${}^{\ell}V_r^k$, in direction r,

${}^{\ell}V_{ti}^k$ = i-th component of unit vector ${}^{\ell}V_t^k$, in direction t,

${}^{\ell}V_{si}^k$ = i-th component of unit vector ${}^{\ell}V_s^k$, in direction s,

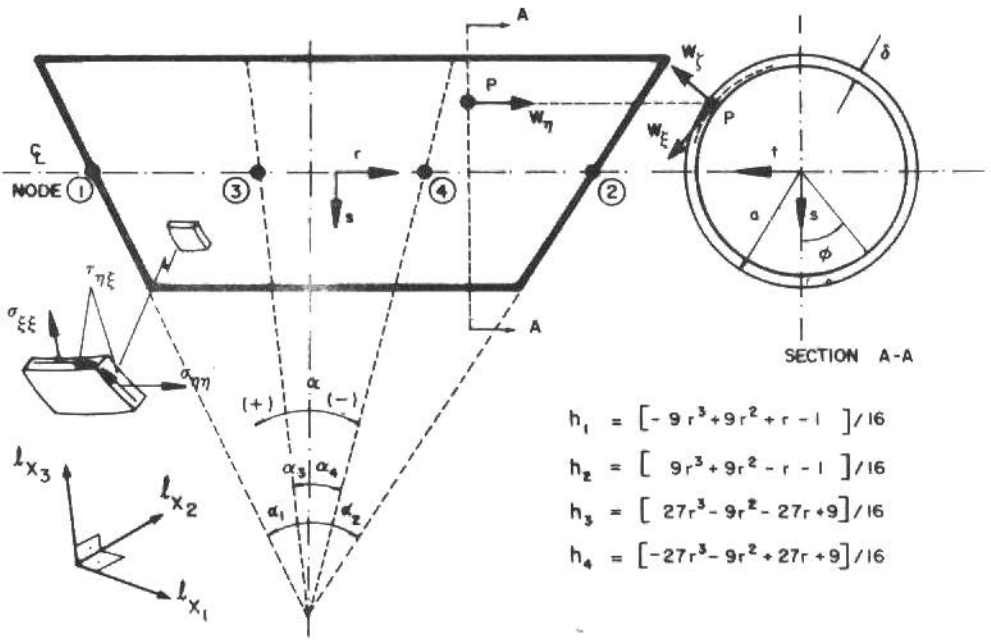

Figure 1. Displacement and coordinate systems of pipe mitred element

and the left superscript $\ell = 0$ denotes the original configuration, whereas $\ell = 1$ corresponds to the deformed position. Using equation (1) with the linear displacement definition

$$u_i(r,s,t) = {}^1x_i - {}^0x_i \quad , \tag{2}$$

the displacement components at any point r,s,t in the pipe are readily obtained

$$u_i(r,s,t) = \sum_{k=1}^{4} h_k\left[u_i^k + t\, a_k\, V_{ti} + s\, a_k\left(V_{si} + \tan\alpha_k\, V_{ri}\right)\right] \tag{3}$$

with

$$\begin{aligned} \mathbf{V}_r &= \theta^k \times {}^0\mathbf{V}_r \\ \mathbf{V}_s &= \theta^k \times {}^0\mathbf{V}_s \\ \mathbf{V}_t &= \theta^k \times {}^0\mathbf{V}_t \end{aligned} \tag{4}$$

where θ^k is a vector listing the nodal point rotations at node k. Thus, from equation (3) the displacement components $u_i(r,s,t)$ are given in terms of the nodal point displacements u_i^k and rotations θ_i^k, i = 1,2,3 and k = 1,2,3 and 4. In the equation (4) above the superscript k has been supressed from the nodal point unit vectors because they are uniform along the element length.

The second displacement field is that the shell surface of the pipe mitred element can deform (ovalise) with certain displacement patterns, see Ref.[10, Fig.4], and we interpolate these displacements cubically along the length. Considering the shell mid-surface displacements in the tangential and radial directions we use, respectively,

$$w_\xi(r,\phi) = \sum_{k=1}^{4} h_k\left[\underbrace{\sum_{m=1}^{N_c} c_m^k \sin 2m\phi}_{\text{in-plane bending}} + \underbrace{\sum_{m=1}^{N_d} d_m^k \cos 2m\phi}_{\text{out-of-plane bending}}\right] \tag{5}$$

and, with a non-stretching condition [10],

$$w_\zeta = -\frac{dw_\xi}{d\phi} \tag{6}$$

where the c_m^k and d_m^k are the unknown generalized ovalisation displacements. In the implementation we have allowed N_c to be 0 (no ovalisation), 1,2 or 3, and similarly for N_d. Thus, the total element displacements are the sum of the displacements given in equations (3) and (5) and, a typical element nodal point can have from 6 to 12 degrees of freedom, i.e.,

$$u^{k^T} = \left[u_1^k\ u_2^k\ u_3^k\ \theta_1^k\ \theta_2^k\ \theta_3^k\ c_1^k\ c_2^k\ c_3^k\ d_1^k\ d_2^k\ d_3^k\right] \tag{7}$$

depending whether the ovalisation displacements are included and which ovalisation patterns are used.

Element Strain and Stress Components

Considering the surface of the pipe mitred element to be a cylindrical thin shell, which deforms in the axial (η), radial (ζ) and tangential (ξ) directions, the strain terms included in the formulation are the same that in the pipe elbow element [10-12]. Namely, two normal and two shear strain components in the η - ξ plane are due to the beam bending nodal displacements and rotations and the shell mid-surface ovalisation which can vary along the longitudinal axis of the element. Therefore, the element complete strain-displacement transformation matrix is obtained by substituting the foregoing equation (3) into equations (18) to (24) of Ref.[10] to obtain the $\mathbf{B}^k$ matrix in Ref.[10, eq.(16)] and the corresponding Jacobian transformation **J**. The remaining ovalisation contribution matrices are obtained using geometric compatibility equations with the assumptions stated in Refs.[10,11]. Considering the skin of the mitred pipe as a thin cylindrical shell [14], we have identified the following important strain definitions, which are included in the element formulation,

$$(\varepsilon_{\eta\eta})_{ov} = \left(\frac{a^2}{\det \mathbf{J}}\right)\left[w_R(\tan\alpha_1 - \tan\alpha_2) - \left(\frac{a^2}{\det \mathbf{J}}\right)\frac{d^2 w_\zeta}{dr^2}\,\zeta\right] \tag{8}$$

$$(\varepsilon_{\xi\xi})_{ov} = -\frac{1}{a^2}\left[w_\zeta + \frac{d^2 w_\zeta}{d\phi^2}\right]\zeta \tag{9}$$

$$(\varepsilon_{\eta\xi})_{ov} = \left(\frac{a^2}{\det \mathbf{J}}\right)\frac{dw_\xi}{dr} \tag{10}$$

where w_R is the local displacement of the pipe wall in a direction

parallel to the plane of the pipe, a is the outer radius of the pipe, ζ is the local coordinate in the pipe wall and α_i is the cross-section central angle, see Figure 1. The strain terms in equations (8-10) can be directly evaluated using the interpolation of w_ξ and w_ζ given in Eqs.(5) and (6). However, since the second term of Eq.(8), which is due to longitudinal bending of the pipe skin, contains the second derivative of the pipe skin radial displacement, it is necessary to enforce in the finite element formulation continuity in the first derivative [15]. This is achieved using a penalty procedure described in the next section. Using the above strain expressions and the displacement interpolations in equations (3) and (5), the total element strain--displacement matrix is obtained, as included in Refs.[10, eqs.(25--31)] and [11, eqs.(10-15)].

The stress-strain matrix used in the analysis corresponds to plane stress conditions in the ξ - η plane, as given in [10, eq.(32)].

Imposition of Continuity on Derivative of Pipe Skin Radial Displacement

The objective is to enforce continuity on the first derivative of w_ζ between adjoining elements without introducing additional degrees of freedom. To impose this continuity condition, e penalty procedure is employed [16]. The basic technique of this method is to add the constraint to be achieved in the solution,

$$\text{CONSTRAINT} = 0 \tag{11}$$

to the Variational Indicator Π of the problem in the form of

$$\frac{1}{2}\int_0^{2\pi} \kappa(\text{CONSTRAINT})^2 \, d\phi \tag{12}$$

where κ is the penalty parameter. The solution obtained by imposing $\delta\Pi = 0$ with equation (12) will satisfy equation (11) to a required accuracy provided κ is selected to be sufficiently large [16,18]. In classical analysis of beam structures, this continuity can be realized without using rotational degrees of freedom. In this case no transverse shear is assumed in the beam section and the penalty parameter κ physically represents the stiffness of a coil spring attached to each element at the common section [18].

Considering the intersection of two pipe mitred elements (under in-plane bending), shown in Figure 2, we have the following continuity condition at the oblique common edge,

$$\text{CONSTRAINT} = \frac{dw_\zeta}{d\Delta}\bigg|^{(n)}_{r=+1} - \frac{dw_\zeta}{d\Delta}\bigg|^{(n+1)}_{r=-1} \tag{13}$$

where Δ is a coordinate perpendicular to the helical edge. Referring to local shell coordinates, the derivatives in equation (13) can be written

$$\frac{dw_\zeta}{d\Delta} = \frac{dw_\zeta}{d\eta}\sin\Psi + \frac{dw_\zeta}{\bar{a}\,d\phi}\cos\Psi \tag{14}$$

where, $\bar{a}$ is the pipe mid-surface radius and Ψ is the local helix angle. In this study the radial displacement w_ζ is interpolated in the ϕ-direction with the same function patterns at both adjoining elements, see Eq.(6). Hence, in the penalty procedure the above equation can be reduced to

$$\frac{dw_\zeta}{d\Delta} = \frac{dw_\zeta}{d\eta}\sin\Psi \tag{15}$$

Substituting equations (15), (13) and (6) into equation (12) and invoking the stationarity condition on Π results into the following penalty matrix

$$\mathbf{K}_p^C = \kappa \int_0^{2\pi} \mathbf{G}_C^T\, \mathbf{G}_C\, d\phi \tag{16}$$

where

$$\mathbf{G}_C = \Big[\ldots a_1^{k(n)}\ a_2^{k(n)}\ a_3^{k(n)}\ b_1^{k(n)}\ b_2^{k(n)}\ b_3^{k(n)} \ldots\ a_1\ a_2\ a_3\ b_1\ b_2\ b_3 \ldots$$

$$\ldots a_1^{k(n+1)}\ a_2^{k(n+1)}\ a_3^{k(n+1)}\ b_1^{k(n+1)}\ b_2^{k(n+1)}\ b_3^{k(n+1)} \ldots\Big] \tag{17}$$

$$a_m^{k(n)} = -\chi_m^{(n)}\frac{dh_k}{dr}\bigg|_{r=+1}\cos 2m\phi \qquad \left.\begin{matrix} \\ \\ \end{matrix}\right\} \ k \neq 2 \tag{18}$$

$$b_m^{k(n)} = \chi_m^{(n)}\frac{dh_k}{dr}\bigg|_{r=+1}\sin 2m\phi \tag{19}$$

$$\left.\begin{aligned} a_m^{k(n+1)} &= \chi_m^{(n+1)} \left.\frac{dh_k}{dr}\right|_{r=-1} \cos 2m\phi \\ b_m^{k(n+1)} &= -\chi_m^{(n+1)} \left.\frac{dh_k}{dr}\right|_{r=-1} \sin 2m\phi \end{aligned}\right\} \quad k \neq 1 \tag{20, 21}$$

and for the common node i,

$$a_m = a_m^{2(n)} + a_m^{1(n+1)} \tag{22}$$

$$b_m = b_m^{2(n)} + b_m^{1(n+1)} \tag{23}$$

with the following notation

$$\chi_m^{(n)} = \frac{4m}{L_n + \bar{a}\cos\phi\,\tan\alpha} \sin\Psi \tag{24}$$

and K_p^C is defined corresponding to the ovalisation degrees of freedom of both elements (n) and (n+1). The matrix K_p^C with a relatively large value of κ is added employing the usual direct stiffness matrix procedure [15] to enforce the constraint in Eq. (13). In section 3 the appropriate magnitude for the penalty parameter κ is illustrated throughout the sample analyses presented.

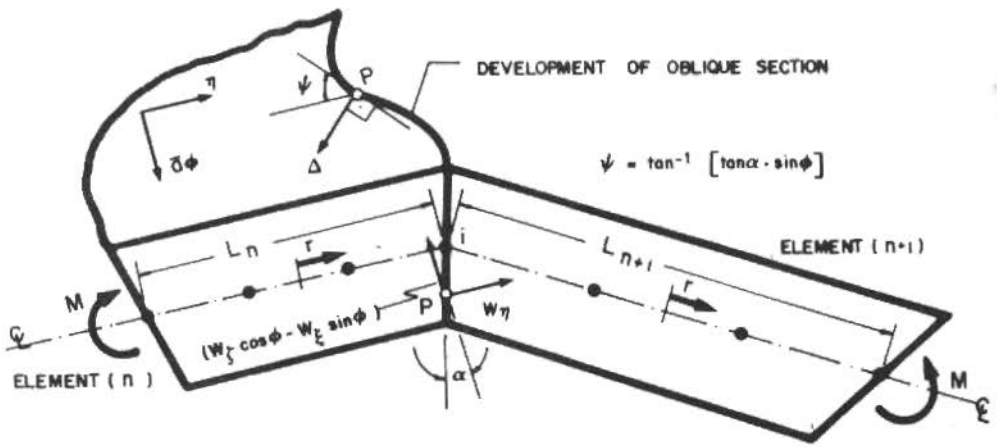

Figure 2. Element interactions at oblique common section

SAMPLE ANALYSIS

The foregoing enhancements to the basic pipe elbow formulation have been implemented in the computer [10,11]. The following two sample analyses are presented to indicate the applicability of these enhancements.

Analysis of a 90-deg Pipe Mitred Bend

The 90-deg. pipe mitred bend structure, considered already in Refs.[3,19] for experimental and analytical analyses, was now modelled for its elastic response under in-plane bending. Figure 3 shows the pipe bend and the finite element idealization considered. Beam y-z displacements and the corresponding nodal rotations are left free, while compatibility conditions have been imposed at nodes 4, 7 and 10. Three in-plane ovalisation patterns at each node are considered in the model.

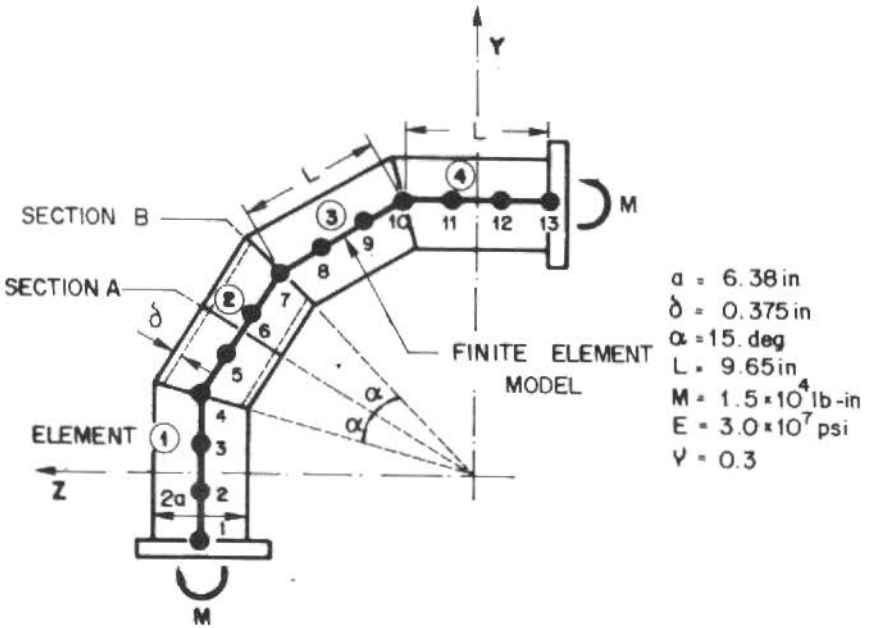

Figure 3. 90-Deg. piping structure and FE idealization considered

Figures 4 to 7 show the stress factors at sections A and B as predicted by the finite element model and compared to previously published results [3,19]. The correspondence between the results is good, however, it is noticed that the longitudinal factors at

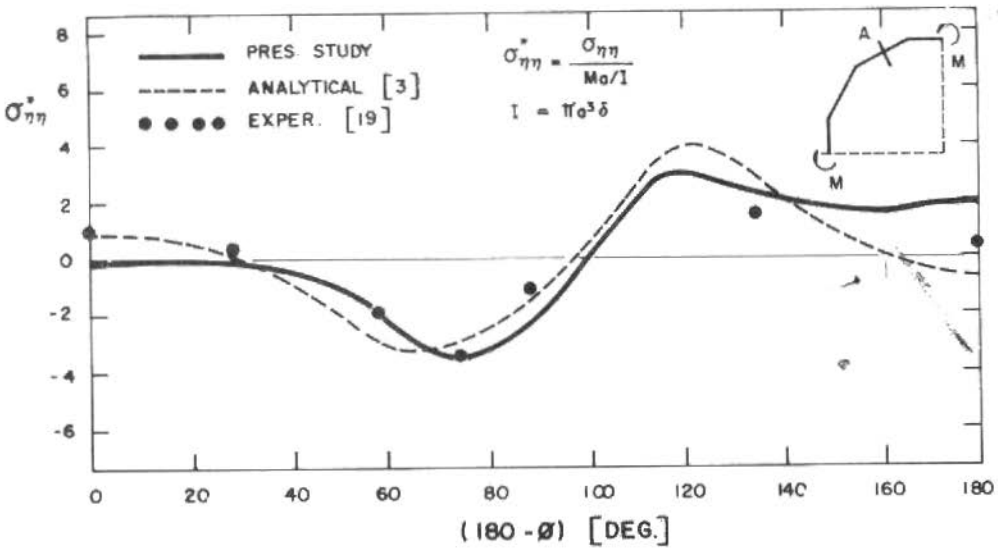

Figure 4. Longitudinal stress factors at mid-section A, at the outer surface of the pipe

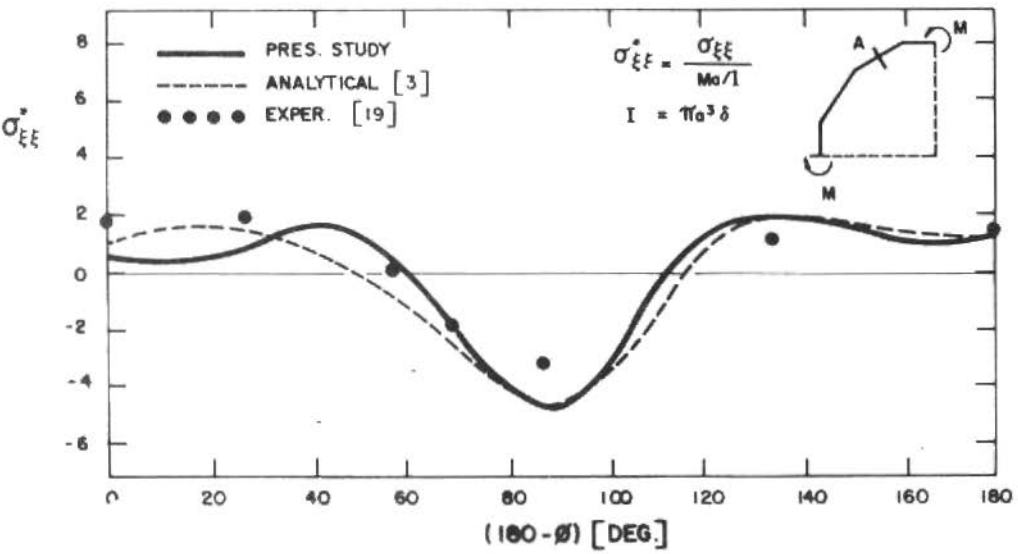

Figure 5. Circumferential stress factors at mid-section A, at the outer surface of the pipe

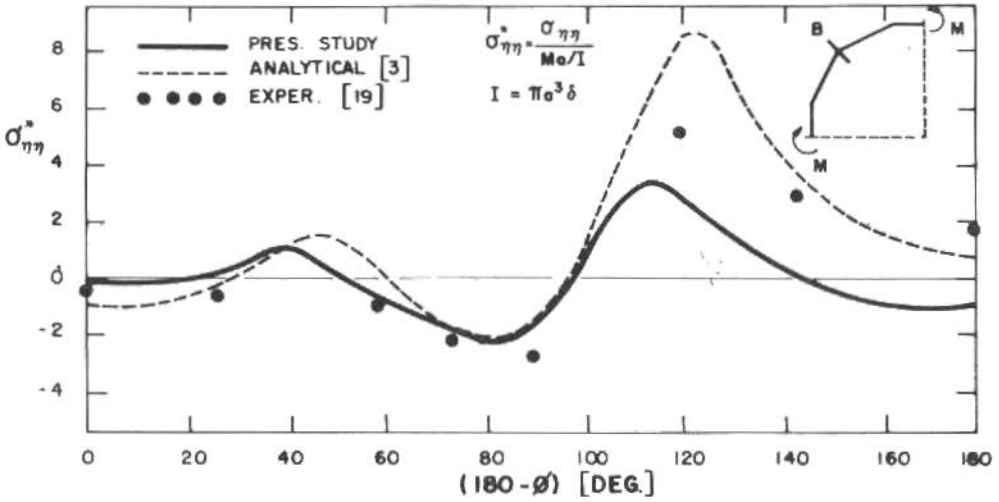

Figure 6. Longitudinal stress factors at edge-section B, at the outer surface of the pipe

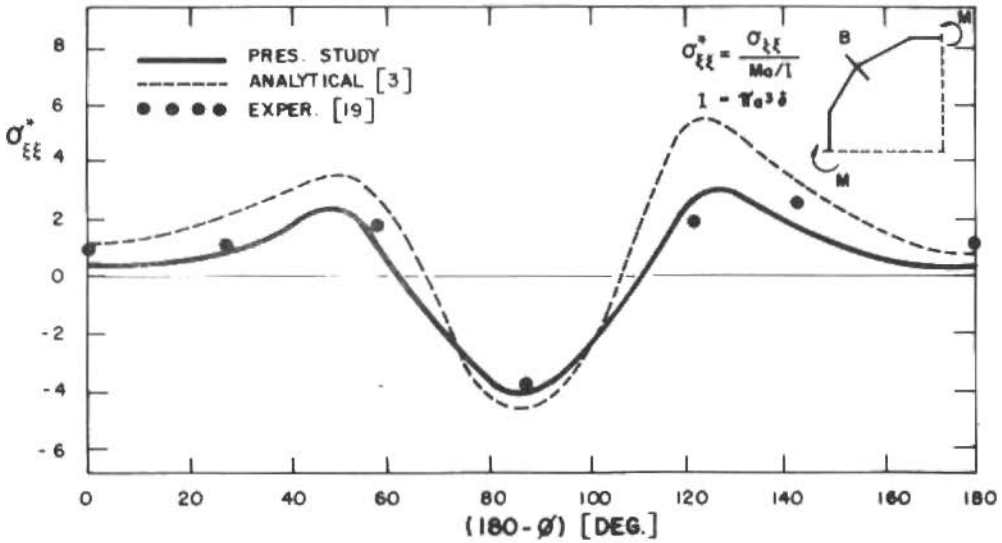

Figure 7. Circumferential stress factors at edge-section B, at the outer surface at the pipe

the common edge show larger differences. The deviation from the experimental results is due mainly to geometric and kinematic approximations used in the model formulations.

Table 1 shows the overall pipe flexibility factors predicted by the analyses. The results present a deviation smaller than 10%. It is interesting to notice that the flexibility factor for the smooth bend theory is in this case within the range of the mitred bend theory results. The penalty parameter κ, that provides good agreement between local rotations at the inter-element edge is of order of 10^3.

Table 1. 90-deg. pipe flexibility factors

Analytical [3]	8.06
Experimental [19]	7.93
Present Study	6.73
Smooth Pipe Theory [9]	7.55

Analysis of a 180-deg. Pipe Mitred Bend

Figure 8 shows a piping structure recently studied for in-plane bending in both experimental and numerical investigations [13]. The numerical analysis was performed with the ADINA program on one-quarter of the piping structure with a 106 shell element model and 4804 d.o.f.

In our analysis we used the 4 element model shown in Figure 8. Interaction effects were imposed at the inter-element nodes and, because of symmetry, only one half of the structure was considered but, with the appropriate boundary conditions at node 13.

The stress responses predicted using the pipe mitred model are shown in Figures 9 to 12. It is seen that the predicted responses given by the shell model at section A follow very closely the experimental results, while the simplified mitred model shows just the same trend. Differences are more significant at the section B for the longitudinal stress factors. However, as it has

been shown in the shell model [13] that difference decays very rapidly along the element length, and its effects on the pipe overall behaviour is negligible. Table 2 shows the pipe flexibilities and a good agreement in the results given by the models is noticed. In this case, the smooth bend theory predicts the lowest flexibility factor, indicating the stiffning effect that occurs as the number of mitred elements is increased to form the pipe bend.

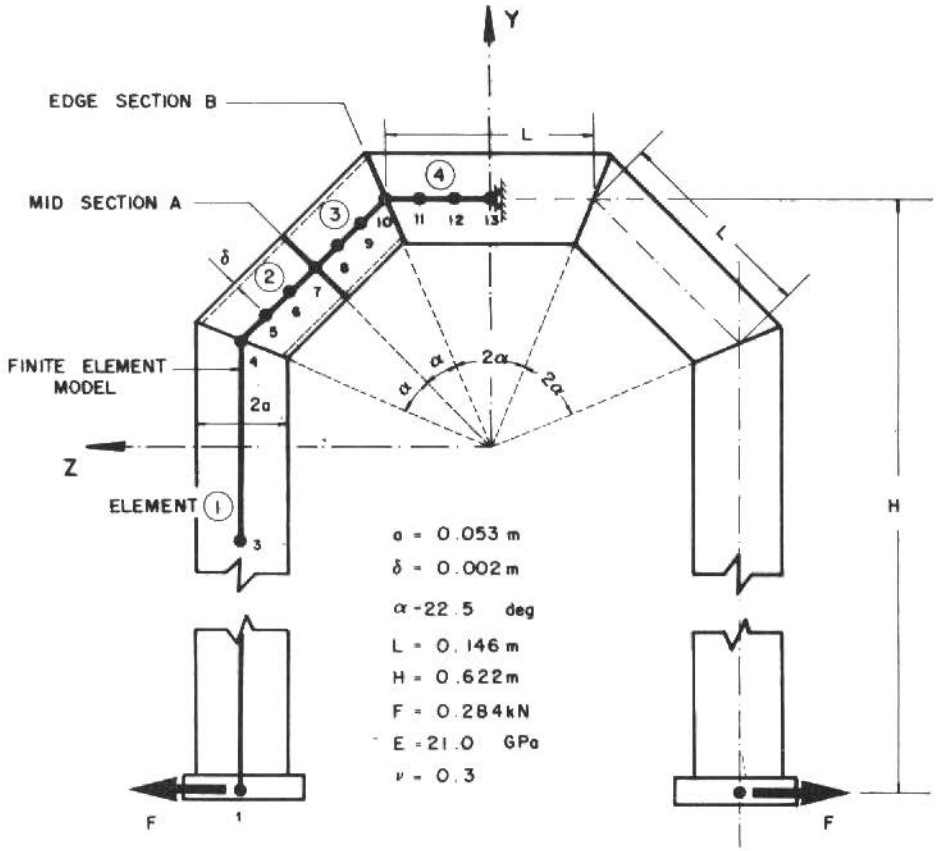

Figure 8. 180-deg. piping loop and FE idealization considered

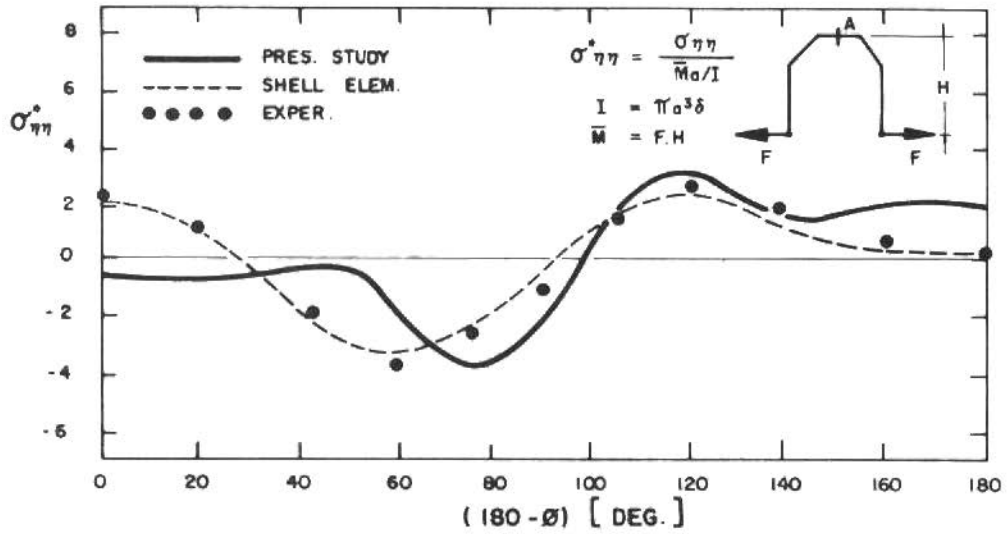

Figure 9. Longitudinal stress factors at mid-section A, at the outer surface of the pipe

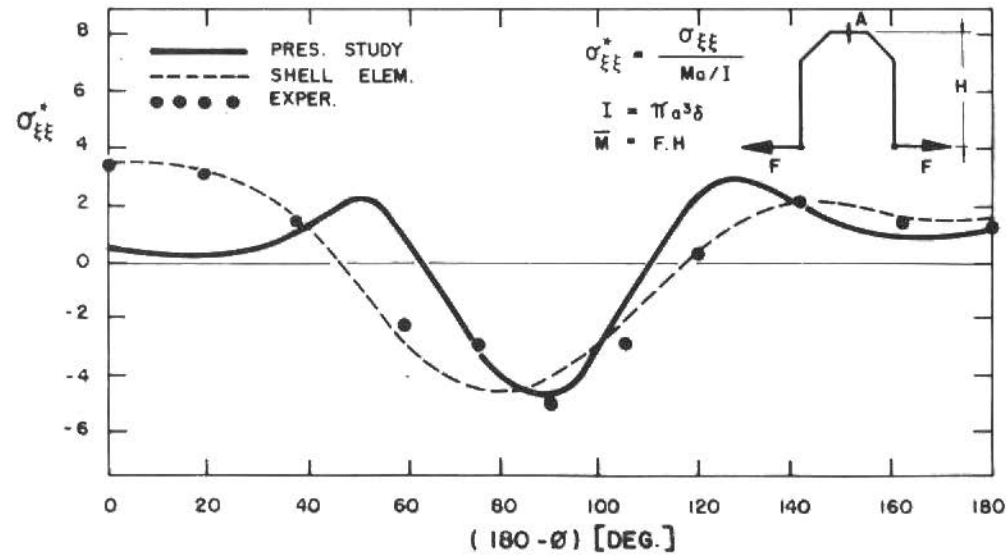

Figure 10. Circumferential stress factors at mid-section A, at the outer surface of the pipe

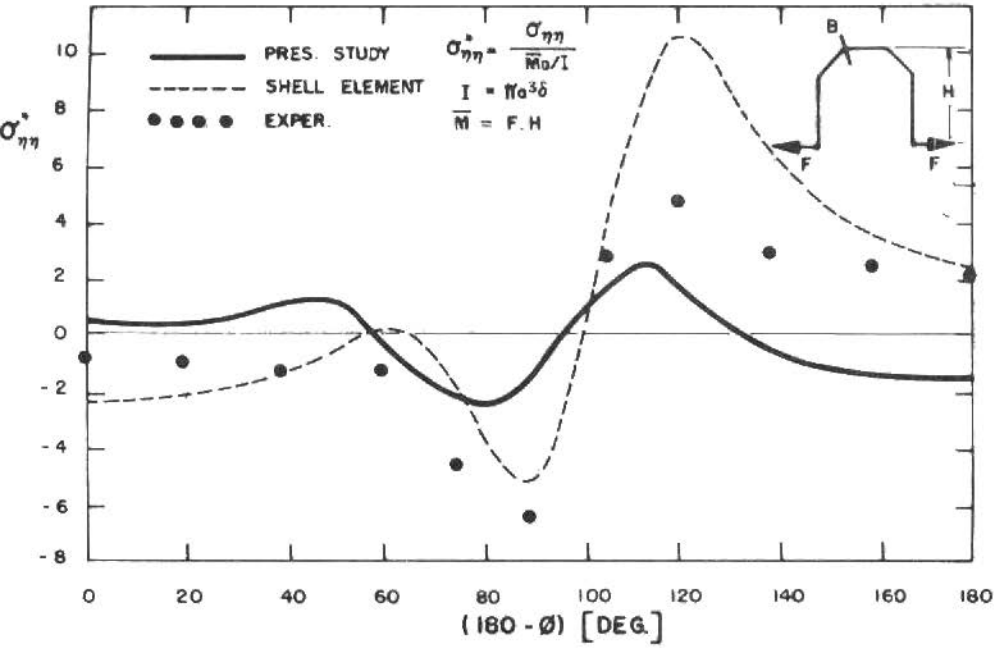

Figure 11. Longitudinal stress factors at edge-section B, at the outer surface of the pipe

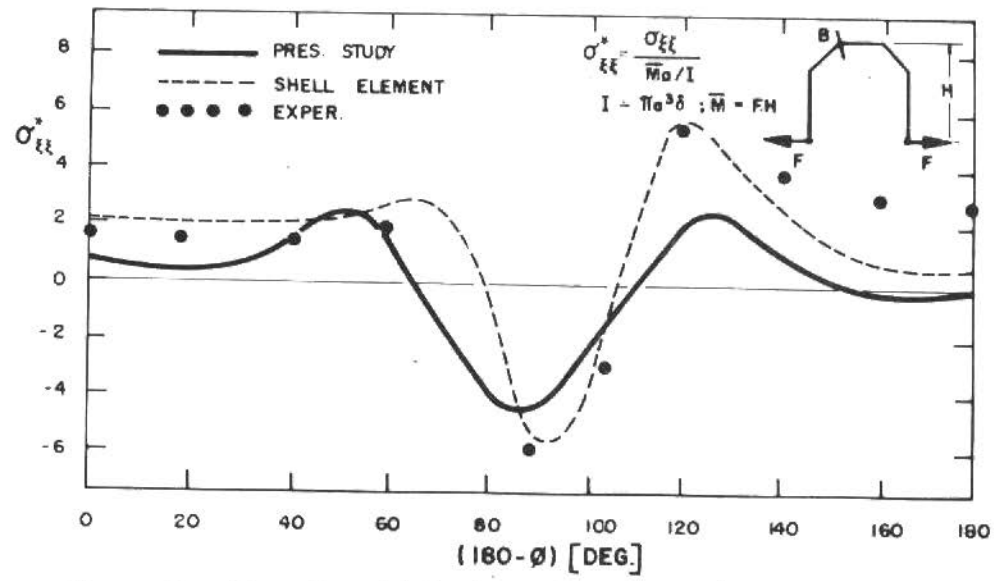

Figure 12. Circumferential stress factor at edge-section B, at the outer surface of the pipe

Table 2. 180-deg. pipe flexibility factor

Experimental [13]	11.6
Shell Elements, ADINA [13]	12.2
Present Study	10.2
Smooth Pipe Bend Theory [9]	8.56

CONCLUSIONS

The pipe elbow element formulation presented in [10,11] has been enhanced to model pipe mitred bends. The beam and the cross-section ovalisation displacement kinematics are included in a novel such the interaction conditions and the compability between adjoining elements are modelled properly. The results of some sample analyses have been presented to show the element effectiveness, however, since the total formulation is based on a number of assumptions, further detailed evaluations of the element performance are required in order to identify the limit of range of problems for which the element is applicable.

REFERENCES

[1] Jones, N. – On the design of pipe bends. Nucl. Eng. Des., 4 : 399-405, 1966.

[2] Murthy, M.V.V. – Stress in a mitred pipe joint under uniform internal pressure. Int. J. Mech. Sci., 6. 1964.

[3] Kitching, R. – Mitre bends subjected to in-plane bending moments. Int. J. Mech. Sci., 7 : 551-575, 1965.

[4] Bond, M.P. and Kitching, R. – Multi-mitred and single-mitred bends subjected to internal pressure. Int. J. Mech. Sci., 13. 1971.

[5] Wang, I.; Chen, H. and Liu, C.R. – Mitred joint of two cylindrical shells intersecting at an arbitrary angle. 4th Intl. Conf. Press. Vessel Tech., London, May 1980. Paper C92.

[6] Green, A.E. and Emmerson, W.C. – Stresses in a pipe with a discontinuous bend. J. Mech. Phys. Solids, 9 : 91-104, 1961.

[7] Van der Neut, A. – Bending at the oblique end section of cylindrical shells. Proc. Symp. on the Theory of Thin Elastic Shells, Amsterdam,

1960. p.247-269.

[8] Jones, N. and Kitching, R. – A Theoretical study on in-plane bending of a single unreinforced mitred bend. J. of Strain Anal., 1 (3) : 264-276, 1966.

[9] Von Kārmān, T. – Über die formänderung dünnwanndiger rohre, innsbesondere federnder ausgleichrohre. Zeitsechrift des Vereines Deutscher Ingenieure, 55 : 1889-1895. 1911.

[10] Bathe, K.J. and Almeida, C.A. – A Simple and effective pipe elbow element - - Linear analysis. J. of Appl. Mech., 47 : 93-100. 1980.

[11] Bathe, K.J. and Almeida, C.A. – A Simple and effective pipe elbow element - - Interaction effects. J. of Appl. Mech., 49 : 165-171. 1982.

[12] Almeida, C.A. – Efeitos da pressão interna no comportamento geral de tubulações - O Elemento viga-tubo. Revista Brasileira de Ciências Mecânicas, VI (2), 1984.

[13] Souza Fº, A.S.; Braga, A.M.B. e Freire, J.L.F. – Análise de tensões em curvas tubulares segmentadas. Revista Brasileira de Ciências Mecânicas, VII (1) : 279-302 , 1985.

[14] Novozhilov, V.V. – Thin shell theory. Translated by P.G.Lowe, P.Noordhoff Ltd., Groningen, Netherlands, 1964.

[15] Bathe, K.J. – Finite element procedures in engineering analysis. Prentice -Hall, 1982.

[16] Almeida, C.A. – A Simple new element for linear and nonlinear analysis of piping systems. Ph.D. Thesis, M.I.T., November 1981.

[17] Zienkiewicz, O.C. – The finite element method. McGraw-Hill, 1977.

[18] Almeida, C.A. – Enforcement of bending continuity and bending constraint through the penalty function method. (submetido COBEM 85 - Dez.10-13).

[19] Lane, P.H.R. and Rose, R.T. – Experiments on fabricated pipe bends. Brit. Weld. Res. Ass. Report DS/12/60, 1960.

INTERDISCIPLINARY RESEARCH RELATED TO MECHANICAL ENGINEERING

Christian P. Burger
Department of Engineering Science and Mechanics
Engineering Research Institute
Iowa State University

ABSTRACT

Methods and measurement techniques that are common in engineering practice are unfamiliar to our colleagues in the life sciences. Creative adaptations of these techniques to studies involving plants and/or the human body often lead to completely new areas of investigation. This paper describes two examples of such cross-disciplinary research, namely the application of resistance strain gages to measure levels of physiological stress in plants and the use of accelerometers and digital signal analysis to investigate the pathology of joints in the human musculo-skeletal system.

RESUMO

Métodos e técnicas de pesquisa comuns na prática de engenharia são desconhecidas aos nossos colegas de ciências biológicas. Adaptações criativas destas técnicas para o estudo de plantas e/ou o corpo humano frequentemente abrem novas avenidas de pesquisa. Este trabalho descreve dois exemplos deste tipo de pesquisa interdisciplinar, a saber: o uso de extensômetros para medir-se níveis de stress fisiológico em plantas, e o uso de acelerômetros e análise de sinais digitais para a investigação da patologia de articulações do sistema ósseo-muscular no corpo humano.

* Palestra apresentada no VII Congresso Brasileiro de Engenharia Mecânica (VII COBEM), Uberlandia – Brasil, Dezembro 1983.

INTRODUCTION

It is customary to group man's varied activities into three broad categories: physical, biological, and social. On a superficial level, such a classification appears reasonable, but in practice it leads to isolation, avoids cross fertilization of ideas, and inhibits creativity. Engineers in particular should resist classification, because in our profession we inevitably deal with the whole continuum of natural events in which any division, however useful, is also artificial. Such division reflects the needs of the human mind rather than the realities of nature and of man's response to nature.

The department at Iowa State University in which I work is known as the Department of Engineering Science and Mechanics. The name in itself expresses a reluctance to be classified according to any particular specialty. Graduates in mechanics are traditionally considered to be interdisciplinary since their field is an integral part of most engineering curricula. Similarly a graduate in Engineering Science can be expected to have a broader than average foundation in the scientific disciplines that underlie all of engineering. Thus the department is, at least in name, a fertile home for cross- or interdisciplinary research.

Although research in engineering is by its very nature interdisciplinary, the interlinked disciplines usually all belong in the physical category. There is remarkably little research being done that is cross-disciplinary between any two or all three of the main categories: physical, biological, and social. I would like to take the opportunity offered by this lecture to describe two research projects from my own experience that involve a marriage between engineering and the biological or life sciences.

PHYTOMECHANICS

Traditionally, learned men have displayed a tendency to give to every kind of specialization a distinctive greek root label. It is part of our love for big words and a desire to impress. In this spirit of obfuscation, I will combine the greek word for plants with the universally recognized name mechanics to categorize our interdisciplinary research with plants.

At daybreak on a clear day in summer, the first signs of light trigger the stomata in the leaves of plants. They open and

the plants start to transpire through their leaves. For the rest of the day each plant attempts to strike a balance between the evaporative demand from its canopy of leaves and the supply of moisture available in the soil around its roots. The stem links the two systems and since it is not rigid, it will contract and expand as the demand increases or decreases. We can therefore expect the magnitude of these changes to relate to the level of water stress in plants.

To measure these stem strains, we mounted electrical resistance strain gages directly onto the stems of young populus trees in such a way [1,2] that they measured only the circumferential strains. When connected correcly to a well-designed instrumentation system [3,4], the resolution of the strain measurement was around 20 parts per million or 20 micro strains (20 με) for long-term effects observed over a period of days, 5 με for shorter term changes observed over a period of hours, and 1 με for extremely short-term dynamic changes that occurred over periods of several seconds. These strains, together with other relevant measurements as indicated on Figure 1, were recorded onto strip chart recorders of through Analog to Digital Converters (A/D) directly into a computer-controlled data acquisition and graphics display system. Circumferential (horizontal) strains and bark temperature were always recorded together so that a temperature correction could be applied to the strain gage readings when necessary. Because ambient temperature and light have significant short-term effects on stem strain, it is necessary to record them so that their effects can be accounted for separately if other parameters that affect stem size are being studied.

Figure 2 presents the variations in circumferential stem strains on a young maple tree (Acer rubrum) with a stem diameter of 4cm at the gage location and a height of 4 meters. The tree was located in a greenhouse between two tall buildings whose shadows caused a sharp cutoff of sunlight in the morning and in the afternoon [1]. The graph for light intensity shows that direct sunlight reached the tree only from around noon until 4:30 p.m. (1200 to 1630). The ambient temperature and humidity in the greenhouse reflected the changes in light intensity, as did the stem strains which are plotted with contractions downward (smaller

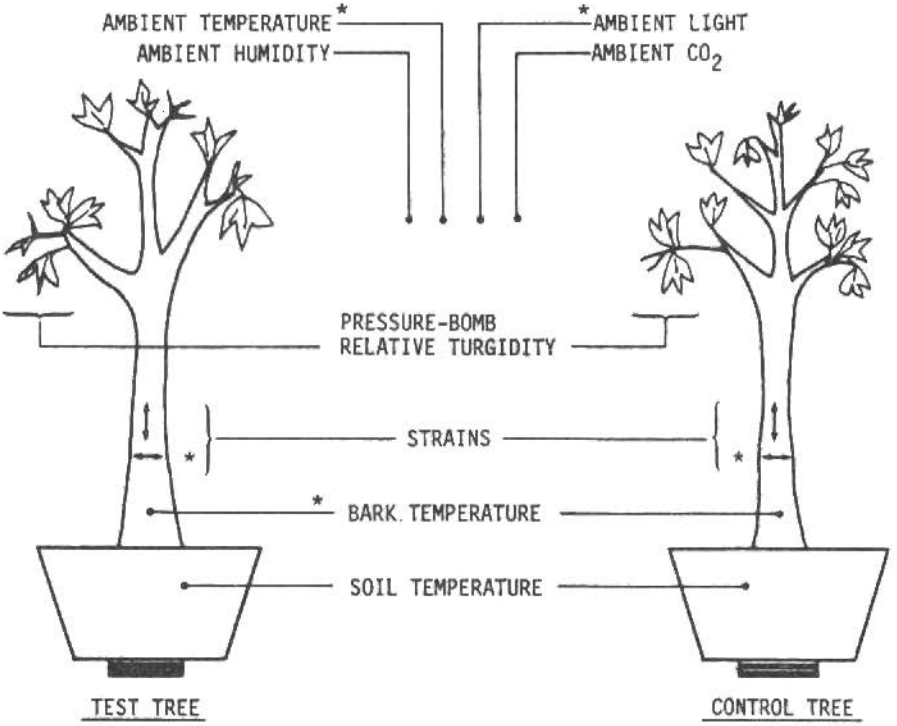

Figure 1. General measurements on trees. Asterisks(*) are standard data points that are always recorder. Other points are optional

strain). The trunk was at its largest (about 2100 με) in the predawn hours and then contracted between 600 and 900 με during its daily cycles. The magnitude of the contractions depended upon the severity of the environmental conditions as represented by the light, temperature, and relative humidity in the greenhouse. These strains translated into daily diametral changes of 0.024 and 0.036 mm, respectively. When a plant is well-watered, as was the case here, it can rehydrate at night and the stem expands until it has recovered its size of the night before. The small increase in maximum size as recorded in the middle of the nights of July 6 and 8 was the grouth for the two-day period.

Figure 3 is similar to Figure 2. However, July 4 was overcast as evidenced by the lower temperature and higher relative humidity in the greenhouse. The stem strains showed that the tree was under much less severe water stress than on the follwing day, July 5.

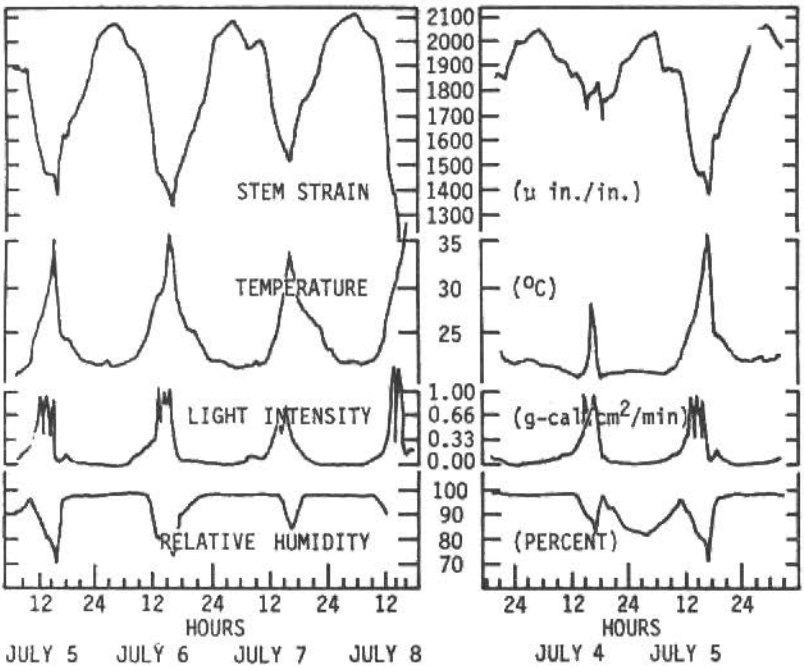

Figure 2. Trunk circumference changes as a function of the diurnal environment under well-watered conditions [1]

Figure 3. Stem chenges for less severe conditions for a well-watered tree

Temperature and humidity combine to create a "vapor pressure deficit" (VPD). Since the amount of vapor which air can hold doubles for every 10°C increase in temperature, a relatively small rise in temperature causes a large increase in VPD. With all other parameters constant, the rate of transpiration is proportional to VPD and this was reflected in the strain records. While the daytime rate of transpiration and therefore the magnitude of stem shrinkage is highly correlated with air temperature, light intensity, and relative humidity, these same variables have little or no effect on stem size at night after the stomata have closed and transpiration ceased.

On July 18 the watering schedule was changed from an ideal 6 liters per day to 1.4 liters every second day. Figure 4 shows

the results. The strain readings began to depart from the normal pattern observed in Figures 2 and 3 when there were no soil-moisture deficits. On July 18 the lowest strain recorded was 1450 με. By July 19 the minimum was further reduced to 1000 με, and this downward trend continued each day until 1500 hours on July 22. Then, with an actual reading of 50 με, the stem contraction was as much as 2150 - 50 = 2100 parts per million with respect to the nighttime unstrained condition that existed in the early hours of July 19.

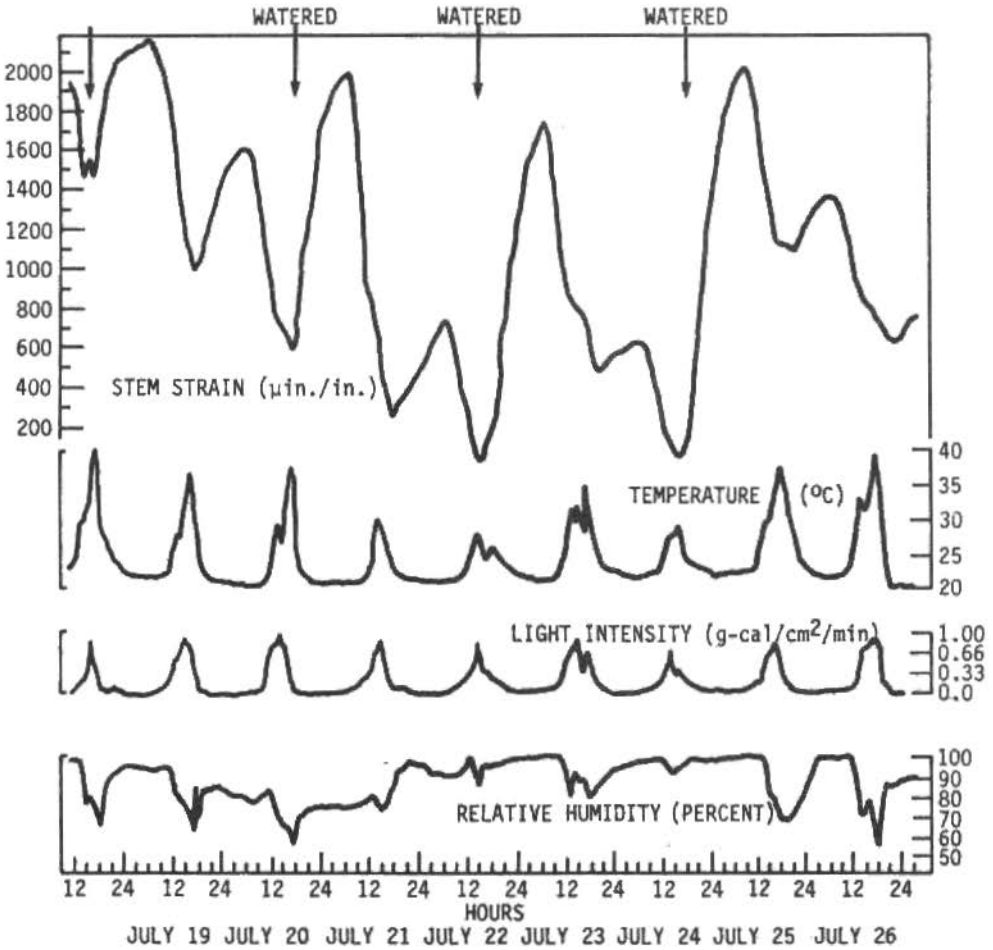

Figure 4. Stem circumference changes with inadequate amounts of water [2]

This relationship was progressive even though the tree was watered with 1.4 liters of water at 1700 hours on July 20. Nighttime recovery was also depressed because the cumulative water deficit was such that the tree was unable to fully rehydrate at night. In fact, nighttime recovery resulted in a maximum strain of only 600 to 700 με on July 21-22 and July 24-25. This was 1400 με less than the average recovery when the tree was adequately watered (Figure 2). Nighttime recovery was considerably greater on those nights following the afternoons when the tree was given 1.4 liters of water. Even then, however, the recovery was not as good as when the tree was well watered.

On July 24 the watering treatment was again altered so that 2.8 liters were added every other day. This had the immediate effect of increasing the highest strain reading to nearly 2100 με which is close to the "normal" nighttime strain readings on Figures 2 and 3. The stem contraction (reduction in strain) on the following two days (July 18 and 19) was not as great as it was when the tree was watered with only 1.4 liters per day. This change in diurnal strain cycle (i.e., smaller stem shrinkage) after the tree was given more water correctly implies that the soil remained moist for a longer period of time than it did when only 1.4 liters were added.

As soil moisture became a limiting factor, light intensity, temperature, and relative humidity had a progressively smaller effect on stem-circumference changes. Since there was very little water being absorbed by the roots, even a small rate of transpiration caused a water depletion within the stem (i.e., stem shrinkage) regardless of the temperature, light intensity, and relative humidity. This insensitivity to environmental inputs when the tree was under severe stress is clearly shown in Figure 4. During the period of July 18 to July 24, when only 1.4 liters of water were added every other day, the lowest strain readings (i.e., largest stem contractions) were recorded on July 22 and 24, yet the temperature averaged 10°C lower, and the relative humidity 25 percent higher than on July 18, 19, 20, when much higher strains were recorded. If the tree had been well watered, the reverse would have occurred.

This example illustrates that we have in the technique of strain gage dendrography a very sensitive and fully quantitative

measure for the irrigation needs of plants

Figure 5 shows three daily cycles as recorded from strain gages on the stem of a young populus tree in a greenhouse [2]. Contractions are now plotted upward so that larger numbers indicate smaller stem sizes (i.e., higher levels of water stress).

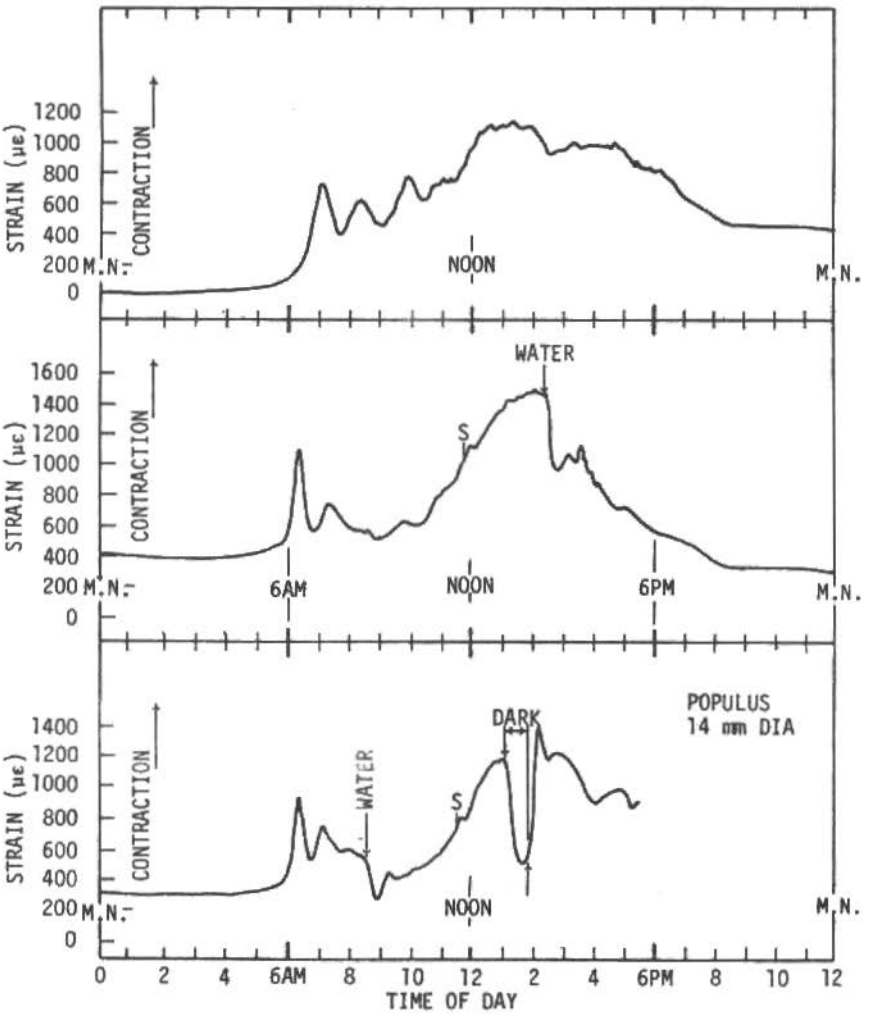

Figure 5. Stem contractions for potted populus tree in greenhouse for 3 different days [2]

Each of the three graphs indicates the responses of the plant to a different set of conditions over a 24-hour period. The soil mixture and root development of this tree was such that it required at least one liter of water each day if it was not to become dry. The upper graph illustrates the results when the tree was not watered during the day. As a result the tree was unable to rehydrate the next evening and did not recover the stem size of the previous night. The residual strain of almost 400 με at the end of the day was an indication of the dryness of the plant, and represented a severe state of water stress. Note also the strain cycles (with a half period of from 40 to 60 minutes) that occur after sunrise (6 a.m.) in all three graphs. This is a characteristic feature of most plants. When their nighttime equilibrium is suddenly disturbed by the break of day, they behave very much like a damped dynamic system, which when disturbed overshoots the new equilibrium position and completes a few oscillations at a characteristic frequency as it approaches its new state.

In the second graph of Figure 5 the plant was not under any stress at the beginning of the day. It was watered at midafternoon and the stem immediately expanded as the moisture deficit in the soil was relieved. Notice again the slight dynamic overshoot as the tree adjusted to the new set of conditions. By midnight, the stem was larger (160 με) than the night before. This was the growth for the day. Thus we could measure growth accurately, nondestructively, and over a period of only one day.

In the third graph the tree was watered early in the morning. We again see the slight overshoot as the water stress was released. At 1 p.m. the blinds in the greenhouse were drawn. Evaporation immediately decreased as the stomata started to close and the stem expanded. Shortly after the maximum expansion was reached, the blinds were opened again and the stem contracted rapidly as the tree snapped back to life. This illustrates the strong influence of light on the physiological activity of plants.

The ease with which the comparative growth data can be obtained through measurements of stem strains is illustrated in Figure 6 [5]. Here, young populus trees were nurtured in artificial environmental chambers for rapid growth. The tests lasted four days with the stem size at the morning of the first

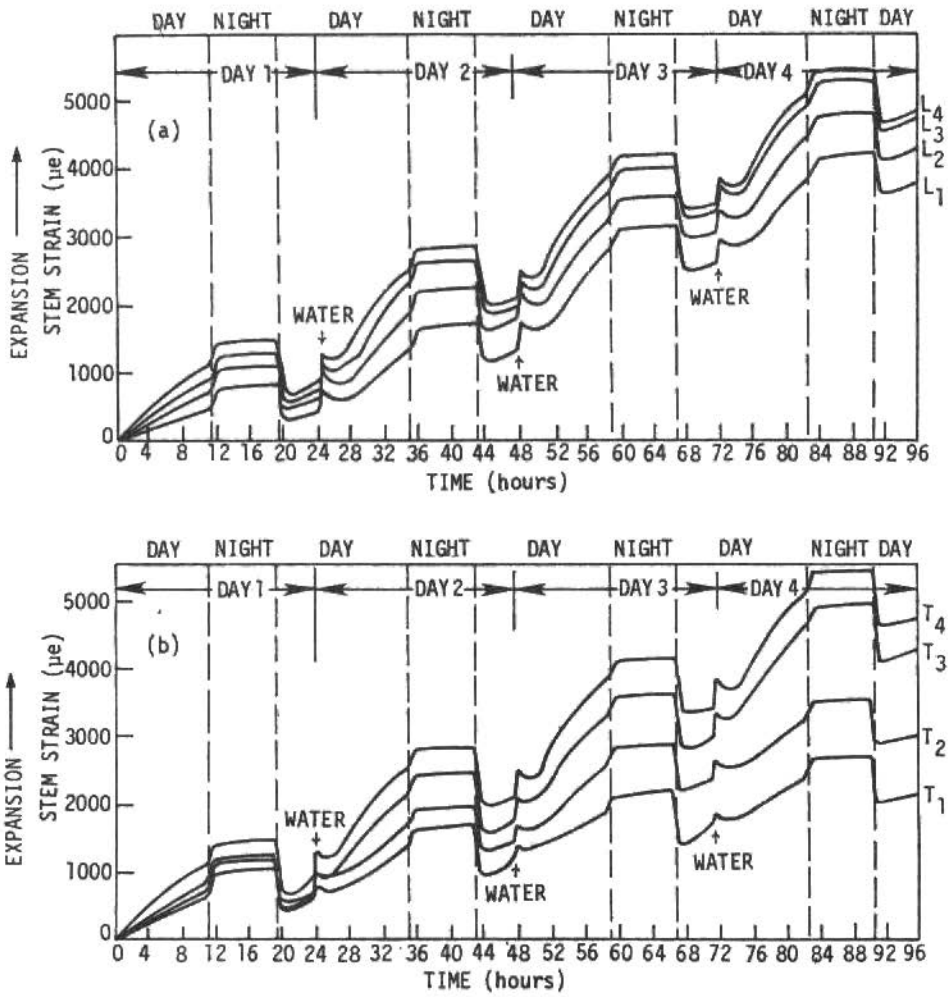

Figure 6. **(a)** Variation of stem strain with time for daytime temperature of $85^{o}F$ and four daytime light levels $L_1 = 26$ μ-einsteins $m^{-2}s^{-1}$; $L_3 = 180$ μ-einsteins $m^{-2}s^{-1}$; $L_2 = 26$ μ-einsteins $m^{-2}s^{-1}$; $L_4 = 330$ μ-einsteins $m^{-2}s^{-1}$.

(b) Variation of stem strain with time for four daytime temperatures at a daytime level of 330 μ-einsteins $m^{-2}s^{-1}$ $T_1 = 55^{o}F$; $T_2 = 65^{o}F$; $T_3 = 75^{o}F$; $T_4 = 85^{o}F$. All nighttime temperatures $15^{o}F$ lower [5]

day taken as zero. Expansion was plotted upward (i.e., positive strain indicates increase in stem diameter with respect to the reference size at zero hours). Each 24-hour cycle consisted of 16 daylight hours (lights on and daytime temperature) and 8 hours of night (lights off and nighttime temperature). Both lights and temperature were switched on or off at the same time. The light level changed abruptly, while the temperature took some time to stabilize. The trees were watered to field capacity five hours after "daybreak" each "day". The resultant rapid stem expansion can be seen on each of the eight lines in Figure 6. Here the curves are much smoother than in the previous graphs. Under the controlled conditions in the environmental chambers, the young plants grew rapidly as is evident from the large increases in the nighttime strain plateaus from one night to the next. The general trend for stem strain throughout each test was one of increasing strain (i.e., expansion of stem). Significant stem contraction occurred only twice during each day. The first was a large contraction at daybreak prior to watering. A smaller contraction occurred after the rapid expansion that followed watering. This is in agreement with the vibration analogy of a damped system discussed earlier. That water stress did exist is evident in the stem expansion that occurs when night starts, i.e., when the lights are switched off and the temperature is reduced.

Using the middle of the period of darkness as a daily reference, the total increase in strain between the first night (16 hrs) and the fourth night (88 hrs) represents the growth during three "standard days". This growth is plotted against daytime temperature for different light levels in Figure 7. This figure reveals that growth was stimulated by increases in light intensity and temperature up to an air temperature of $75^{o}F$ ($24^{o}C$). Growth did not increase at higher temperature. This established, in a very short test, the best growth chamber temperatures for optimal yield in nursery production of seedlings.

The ability of strain gage dendrography to record changes with short response times is illustrated in Figures 8 and 9 [6]. When the strain record for the period during watering of a dry tree is enlarged, the graph appears as shown in Figure 8. Here a young populus tree, similar to the plant used for Figure 5, was allowed to dry out to the point of severe water stress.

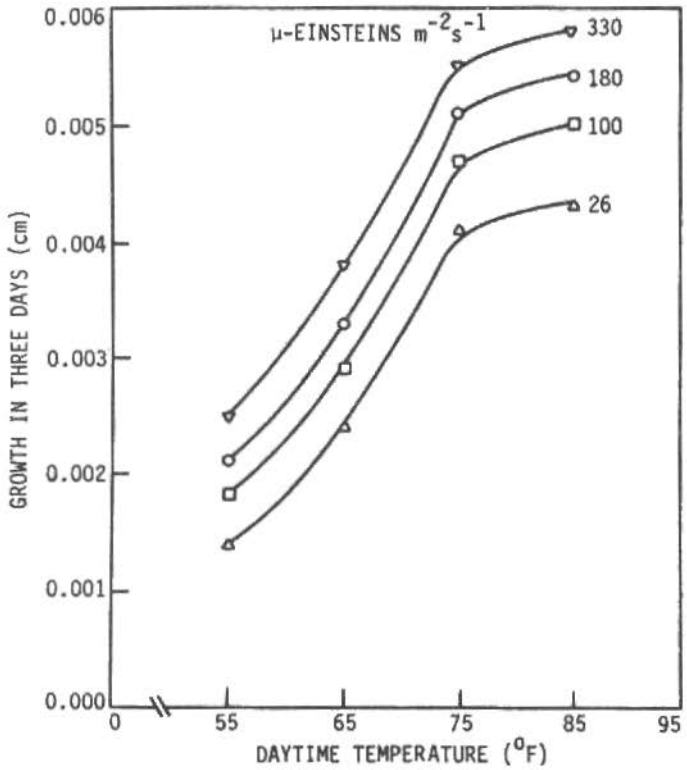

Figure 7. Variation of growth with daytime temperature for various light intensities [5]

The records in both figures start at midmorning during a period of rapidly increasing water stress, i.e., when the stem is contracting rapidly. At time "zero" one liter of water was poured rapidly onto the soil in the pot. Time in seconds was measured from the instant when the water first hit the soil. Three seconds later the stem dynamics as recorded by a strain gage close to the soil (Figure 8a) had changed from rapid contraction to rapid expansion! In Figure 8b the tree was less severely stressed at the time of watering. The response of the gage nearest the soil is similar to but less dramatic than that in Figure 8a. A gage mounted 5cm higher up the stem behaved in a similar manner but took longer to respond. This was the first time that such dynamic behavior was observed in an experiment. Furthermore, no current model for water transport accounts for the very rapid changes seen here.

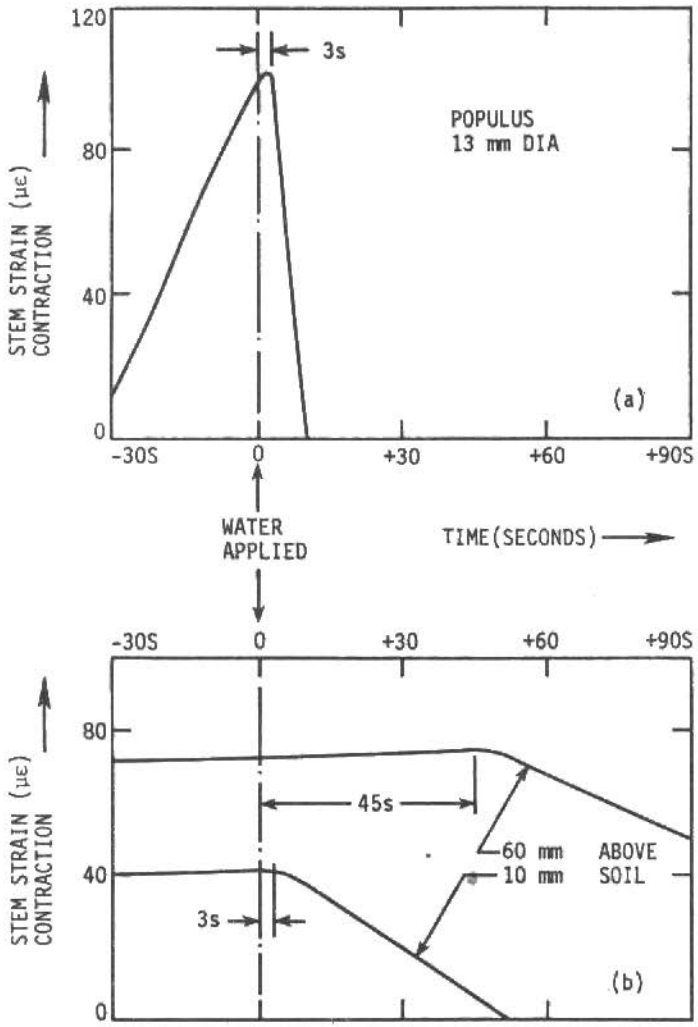

Figure 8. Rapid stem changes upon watering
(a) A severly water-stressed tree
(b) A tree under less severe water stress

Figure 9 presents evidence of a low frequency pulsation in the stems of plants. The base frequency is about 0.3 Hz but, as the figure shows, the fundamental shape and frequency changed with conditions. In this illustration a relatively dry tree was shaded to reduce temporarily the level of water stress. When the shade was removed, the water stress in the tree increased sharply with a

concurrent change in the nature of the pulsations. It is quite conceivable that a detailed study of these pulsations through, for example, fast Fourier transforms will reveal correlations between physiological stress and characteristics dynamic features of the pulsations.

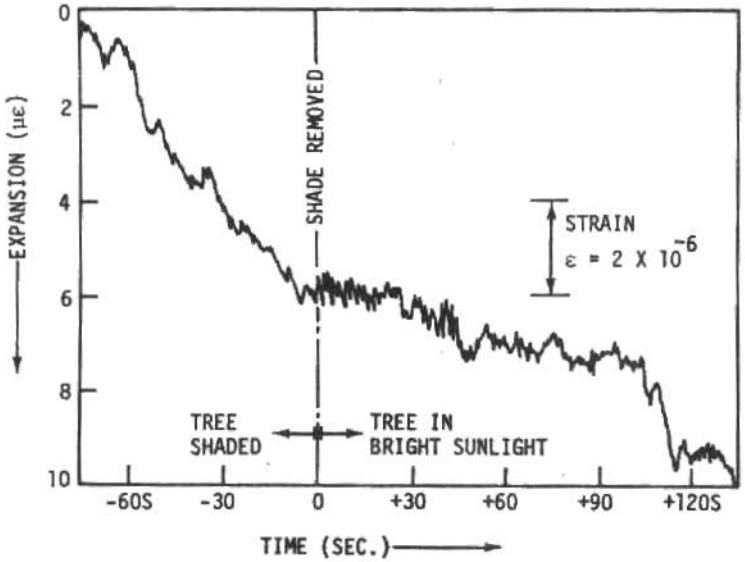

Figure 9. Stem pulsations on a small populus tree

Figure 10 shows a two-day segment of a test that investigated how mild deficiencies in selected nutrients affected the ability of plants to resist drought [7]. The results are average values for statistically selected samples from each of six groups of trees. The control group was grown with a correct balance of Mg, K, N, Bo, and Ph. Each of the other groups were grown with 25% deficiency in one of the nutrients. Two of these are shown plus the response of the control group. The nitrogen (N), potassium (K), and boron (Bo) deficient groups did not deviate significantly from the control group. Their behaviors were similar to that for the Mg deficient trees. After two days in the greenhouse without being watered, the phosphate deficient trees showed signs of severe water stress. Thus short term tests can be used to select the best clones or species for optimum yield in different types of soil.

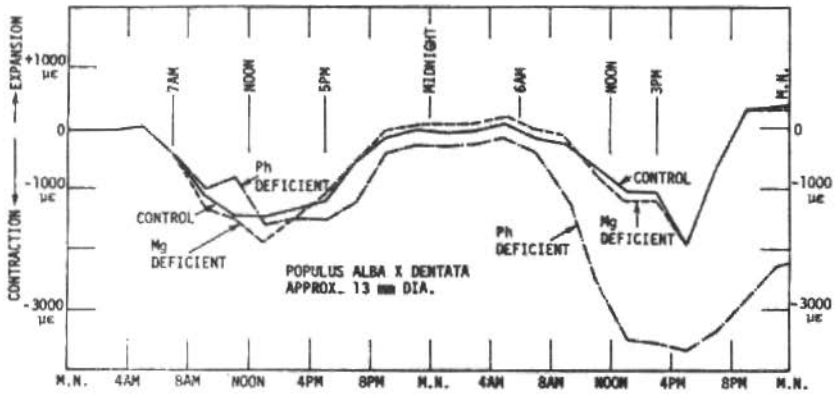

Figure 10. Effect of Ph deficiency on drought resistence of small populus tree

That dendrography is valuable in field experiments on annual crops is shown in Figure 11 [8]. Strain gages were mounted on the stems of two-month-old soybeans that were growing in test plots in the deep loess soil of western Iowa. The results from three different plots are shown in Figure 11. The upper graph is for a square pattern planting in an irrigated plot. The two lower graphs are from results on a square planting pattern and a row pattern in unirrigated lots. There was no significant difference in the daily cycle of water stress for the two types of planting but the irrigated plants showed very little, if any, water stress.

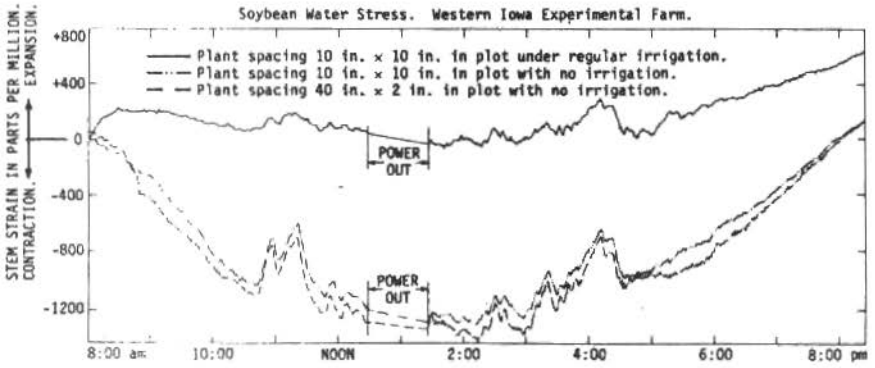

Figure 11. Diurnal record of water stress as reflected in variations in stem size of soybeam plants in three test plots of loess soils

Their growth for the day was considerably more than for the unirrigated plants. While these results are not surprising, the ability of the strain gages to identify behavior patterns in such a short time is remarkable.

These few examples were selected to demonstrate the expanded horizons in plant research that can result from closely integrated cross-disciplinary research between engineers and botanists/ /agronomists.

SKELETAL DYNAMICS

While the application of engineering measurement methods to the areas of forestry and biology is relative rare, this is not the case in medicine. Biomedical Engineering is one area where engineers and their colleagues in the life sciences have long cooperated fruitfully. There remain, however, many problems where the measurement techniques developed for engineering systems can be adapted for improved diagnosis in medicine. To be really effective these methods should be noninvasive, nondestructive, and able to be used in vivo with minimal discomfort to the patient. Also such methods should not alter normal physiological behavior and responses.

We have been able to satisfy these rather difficult requirements in studies of health problems related to abnormal gait and to the pathology of the major joints in the human musculo--skeletal system. This was done by adapting contemporary methods for dynamic signal acquisition and digital fast Fourier transforms (FET) to study how the various joints modify the impulses that result from normal walking.

At heel strike during normal gait a shock wave enters the body. The impulse propagates through the musculo-skeletal system from heel to head. Along the way it is attenuated and modified by various natural shock absorbers such as the foot, ankle, knee, and so on [9]. Voloshin and Wosk conceived the idea of strapping low mass accelerometers to the outside of the body at points where the skeleton is covered only with a thin layer of soft tissue (e.g., the bony protrusions at the ankle, knee, sacrum, and forehead). The person was then asked to walk normally along a short walkway so that the accelerations could be recorded. The resultant waveforms were displayed on a multibeam oscilloscope in such a way that their relative amplitudes could be compared. During a series

of tests on patients with chronic headaches and/or low back pain a correlation emerged between these symptoms and the amount of attenuation of the amplitude of the wave from the sacrum to the forehead. A strong correlation was also found between the shock absorbing capacity of a joint and its clinical condition [10].

The main difficulty with this method is that it only looks at the magnitude of the waves, and these are influenced by many parameters not related to skeletal damping. To overcome this difficulty we drew on some previous experience in ultrasonic spectroscopy in engineering structures. We postulated that in medical dynamics, as in ultrasonics, the really useful information will be in the shape or changes in shape of the waves rather than in their amplitudes. We should therefore look for changes in the frequency spectra rather than changes in amplitude. This turned out to be correct, and we are now embarking on a new biomechanical research program in skeletal spectroscopy.

Figure 12 shows a typical instrumentation system as used in this program. A small accelerometer was held against the tibial tuberosity with an elastic knee brace. The subject then walked naturally along an 8-meter-long walkway while an assistant followed, carrying the electrical leads in such a way that they did not hinder the walk. The leads are light and presented no problem. The sampling rate for the data acquisition was either 500 or 1000 per second, which allowed for accurate recording of signal components up to 250 or 500 Hz, respectively. A fast Fourier transform was performed on all signals and the resultant power spectra were displayed. Additionally, the transfer function (i.e., the changes in the frequenc· spectrum upon passage from one measurement point to the next) was computed and used as the main basis for drawing conclusions.

The continuously respective shocks that invade the human frame during working hours in many occupations or during leisure activities such as jogging or tennis tend to cause progressive weakening of the natural shock absorbers of the body (e.g., knee, elbow, intervertebral disci, and minisci). These shocks may lead to articular cartilage degeneration and osteoarthritis [11]. Improved shoe design, shoe inserts, and arch supports can do much to reduce the risk of degenerative changes in the joints by absorbing the most dangerous frequencies. The digital accelerometry

technique described here provides a quantitative means for evaluating footwear to achieve better health at work and at play.

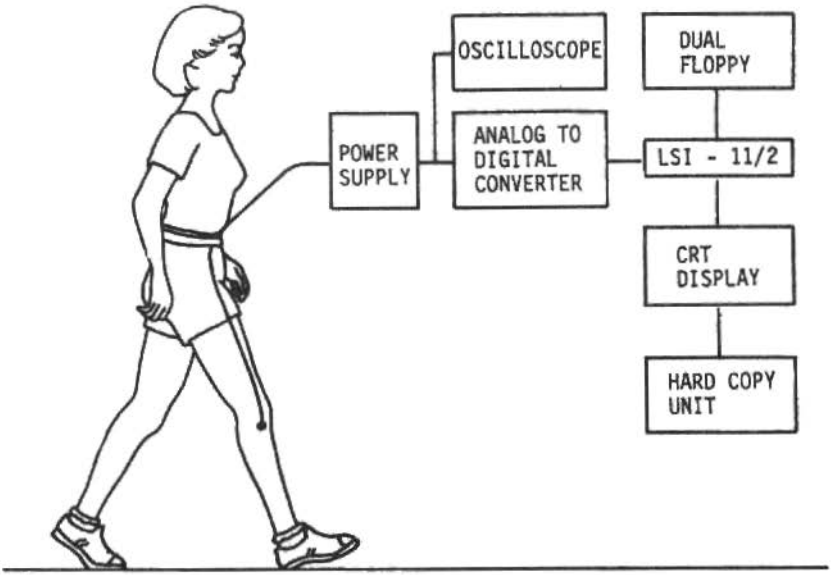

Figure 12. Experimental set-up for single accelerometer

Figure 13 shows the results for comparative tests between three arch support inserts in the same thin-soled shoe [12]. In Figure 13a the amplitude and shape of the impulse as recorded by an accelerometer on the tibial tuberosity for a healthy person walking barefoot with normal gait is compared to the signals obtained when the same person repeats the tests with shoes containing insert number 1. Figure 13b compares the frequency spectra (relative magnitude versus frequency) for the impulse waves due to heel-strike as measured at the tibial tuberosity below the knee for four cases--barefoot and then shoes with three different inserts.

It is clear that donning shoes introduces high frequency components into the wave and that different inserts attenuate selected frequencies differently. If we knew which frequencies were most damaging to health, we could use this type of direct measurement to select the most effective inserts.

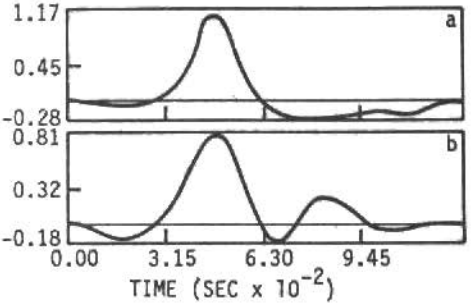

Figure 13. (a) Signal on tibia tuberosity.
(a) Barefoot
(b) Insert # 1

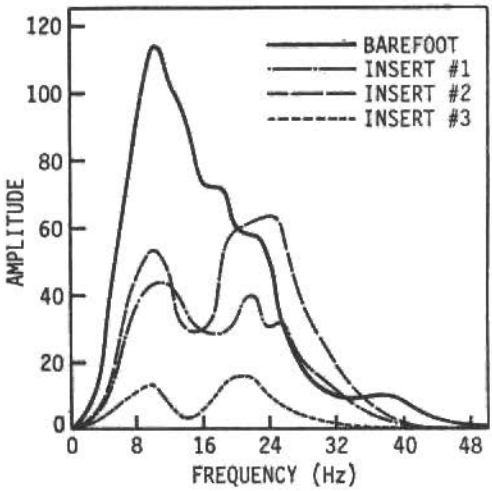

Figure 13. **(b)** Power spectrum density plots for all cases

Chronic low back pain (LBP) affects many people. Signals from accelerometers strapped to the sacrum and to the forehead on a healthy person are shown in Figure 14a [13]. When the same experiment was repeated on LBP patients, the signal as recorded from the sacrum looks different (see Figure 14b). High frequencies of around 100 Hz were apparent in 24 of 28 persons tested. None of these patients displayed neurological deficits in normal x-rays of the pelvis and lumbar spine. When special shoe inserts were prescribed to eliminate these high frequencies, 78% of patients from a test group of 382 persons with LBP reported excellent to good results after one year of treatment.

Another test sought to define the dynamic absorption capabilities of a healthy human knee [14]. Two accelerometers were strapped to the bony protrusions of the knees of five young men. One accelerometer was held in an approximately axial direction on the tibial tuberosity below the knee; the other was similarly held against the medial femoral condyle above the knee. The two analog signals for a period of four seconds were multiplexed, digitized, and stored during normal gait.

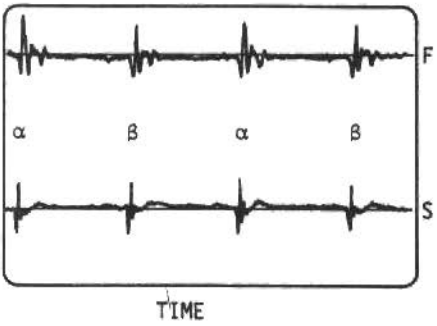

Figure 14. **(a)** A normal accelerogram on sacrum (S) and forehead (F). Impulses from heel strikes of the right foot (α) and the left leg (β) are nearly equal.
Time scale: 200 msec/div.

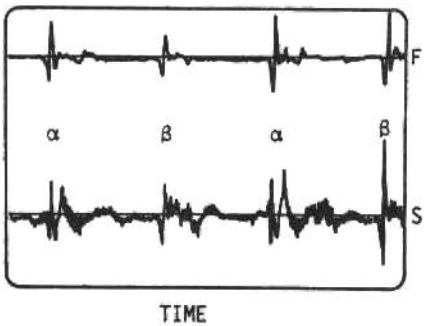

Figure 14. **(b)** Accelerographic patterns from heel strike before treatment. S--accelerometer strapped to the sacrum; F--to the forehead.
Time scale: 200 msec/div.

In this way three consecutive walking cycles were recorded during each test. Figures 15 and 16 show the relative accelerations and their fast Fourier transforms for each of the two locations. It is clear that passage through the knee not only reduced the maximum amplitude but also changed the frequency spectrum.

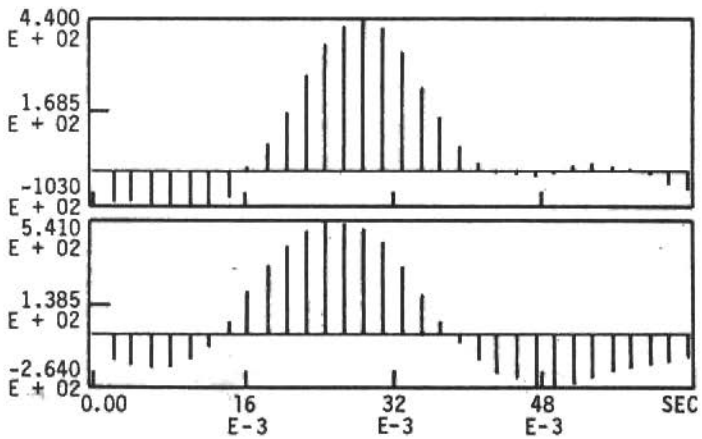

Figure 15. Typical signal recorded on a) medial femoral condyle, b) tibial tuberosity

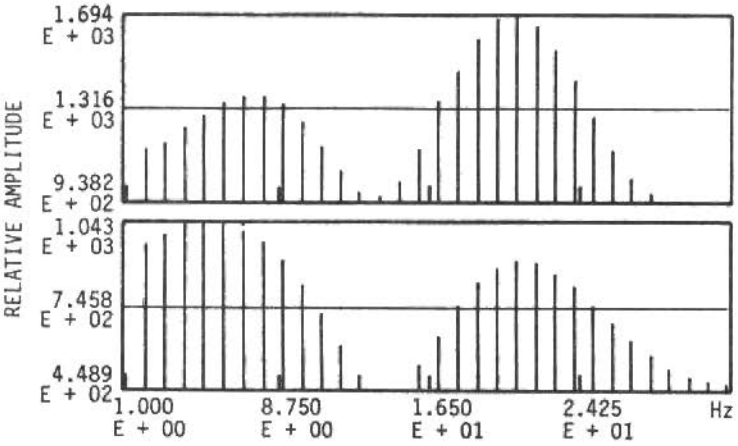

Figure 16. Power spectrum for the recorded signal a) medial femoral condyle, b) tibial tuberosity

The extent of this change is seen in Figure 17, which shows the result of a deconvolution procedure which divides the transmitted wave (medial femoral condyle) by the incident wave (tibial tuberosity) in the complex frequency domain. The important feature is the "valley" which indicated the frequencies that were selectively attenuated by the knee. Note also that there appears to be a time shift (delay) of around 4 milliseconds in the waves of Figure 15 on passage through the knee. This indicates the time needed for the force impulse to pass through the knee. Correct measurement of this time would require a much higher sampling rate (of the order of 5000/sec) than was used in this test.

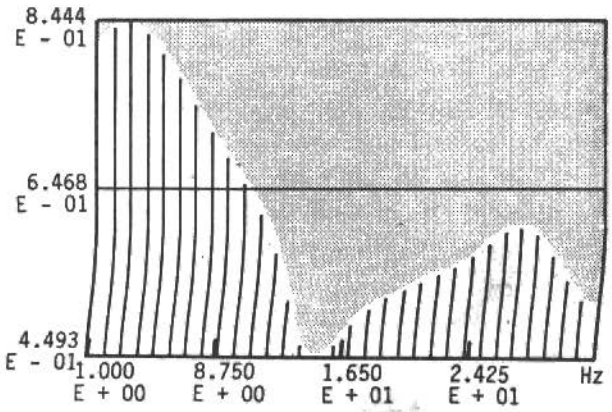

Figure 17. Transmissibility function for the human knee

The next series of experiments will be conducted on persons with knee disorders, with the goal to correlate deviations from the standard transfer function of Figure 17 with the disorders.

Figures 18 and 19 show the more complex changes that occur between the tibial tuberosity and the forehead. The transfer function (Fig.19) is also more complex. As before, deviations from a statistically satisfying standard behavior may contain significant diagnostic information about disorders at various joints and the spine.

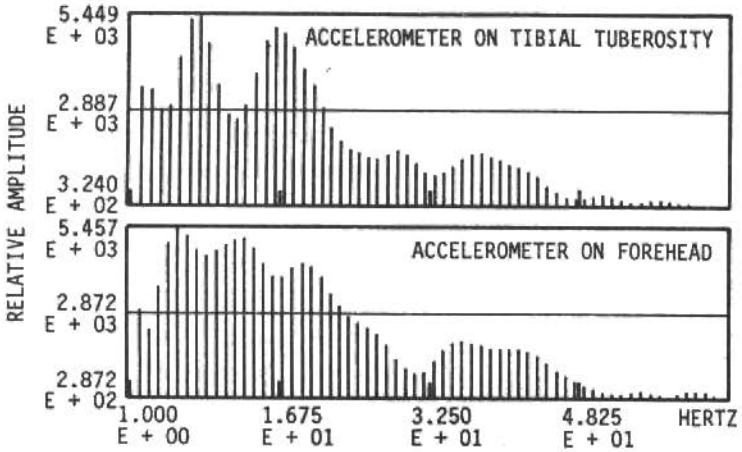

Figure 18. Fast Fourier transform of data for accelerometer on the tibial tuberosity and the forehead

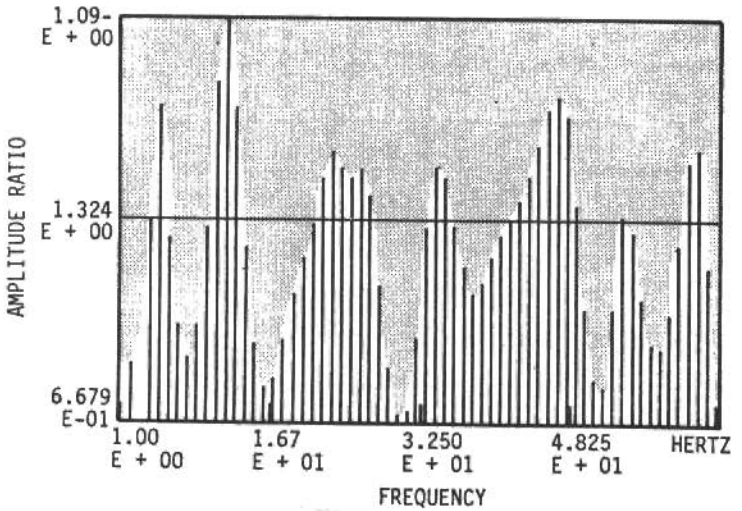

Figure 19. Transfer function for Fig.18

These procedures are made possible by contemporary developments in computers and in digital data acquisition. The acquisition of the data was easy, and the relatively complicated analytical procedures were performed rapidly with the results displayed clearly for easy interpretation. The patients experienced no discomfort and were, in fact, ready to continue their daily routine only minutes after reporting for the test.

CONCLUSION

It is said that: "If I have a dollar and you have a dollar and we exchange, we still each have one dollar. However, if I have an idea and you have an idea and we exchange these, we each end up with two ideas." When cross-fertilization occurs between disciplines, it often leads to a breakthrough which in turn spawns an array of new ideas.

Perhaps the two areas--phytomechanics and skeletal dynamics--which I have chosen as examples of cross-disciplinary research illustrate the above. In this research our results opened doors to many areas of investigation and new applications beg to be pursued. In our immaginations we can, for example, visualize automated irrigation systems based on plant needs. These can optimize water consumption, energy use, and/or production. The benefits of this concept go beyond the obvious. In large areas of the Central United States,for example, agricultural water is pumped from a massive aquifer. This aquifer regenerates only very slowly so that the water has to be considered as a nonrenewable resource. Excessive rates of withdrawal are threatening agriculture over an area that covers several states. In many irrigated lands, excessive irrigation leaches chemicals from the soil into lakes, streams, and even into the groundwater making the water progressively less suitable for consumption by humans and animals. Even in our state of Iowa, a major artificial lake was closed to fishing because of excessive amounts of leached fertilizer salts in the water. Less irrigation will mean a lower risk of chemical loss from leaching and consequently a smaller application of chemicals with benefits in all directions--lower cost, lowered consumption of products derived from petroleum, and improved health.

In other parts of the world, irrigation from large dams is raising the salinity of the soil with disastrous effects on.

productivity. Again, optimum irrigation schedules are needed and dendrography can supply the necessary information. In our cities the trees along the streets are suffereing from air pollution while in some lake areas the vegetation succumbs to acid rain. The strain gage may be the link that will permit the rapid detection of plant responses to poisons in the atmosphere or in the soil and help in selecting species that are resistant to these poisons. On the level of basic research, the measurements of phytomechanics may lead to better models for the transpiration and water transport mechanism in plants. If life on earth depends on plants, then such basic knowledge may be of incalculable value in terms of optimized production of food, shelter, fuel, and even fresh air. Some informed people predict that water and water quality will become a major national and international problem by the end of the 1980s. If that is true, then it is just conceivable that the modest electrical resistance strain gage can be important to man's welfare.

What about those small accelerometers strapped to the body? They may look unimportant but to the injured athlete, the woman with osteoarthritis, the man with an artificial hip joint, and the young war veteran with a prosthesis, they promise relief from discomfort. With the accelerometer the performance of a prosthesis can be evaluated quickly and easily. Recovery from knee surgery can be monitored, and early warning can be given of the onset of osteoarthritis. If the osteoarthritis is related to degenerative damage from vibration or shock, the measurements from these little accelerometers may be used to identify means for retarding or even stopping its development. In a like manner the jogger and the soldier with march fracture may both be thankful for improved shoes designed to eliminate the impulses that cause their maladies. Who would have thought that fast Fourier transforms and deconvolutions could help to reduce chronic headaches and cure low back pain?

In biomechanics, as elsewhere, the biggest problem is to establish dialogue between the engineer and the person with a need. Add a good knowledge of basics with a spark of creativity and the answers may change the world, or at least a small part of the world.

These examples merely scratch the surface of a potentially vast and fruitful area of research. Engineers do, indeed, have a

contribution to make in the life sciences beyond building better tractors, plows, dams, and canals.

ACKNOWLEDGMENTS

The various research projects from which the examples in this paper were drawn were supported in part by the U.S.Department of Interior through Iowa State Water Resources Research Institute, by the National Science Foundation, the Engineering Research Institute, and the Department of Engineering Science and Mechanics at Iowa State University.

REFERENCES

[1] Whipple, R.L.; Ligon, J.B.; Burger, C.P. and Coffman, M.S. – Resistance strain gages as physiological transducers on trees. Exp. Mech., 16 (9) 329-336 (1976).

[2] Johnson, D.B. and Burger, C.P. – Phytomechanics--plant physiology and applied mechanics. Developments in Theoretical and Applied Mechanics, Ed. by R.M. Hackett, vol.9, Proceedings of the Ninth SECTAM, Vanderbilt University, Nashville, Tenn. (1978), p.553-562.

[3] Schutte, K.H. and Burger, C.P. – Sensitive dendrometers for contemporary research: A critical evaluation of strain gage dendrometers. S. Afr. J. Botany, 47 (2) : 273-291 (1981).

[4] Baryeh, E.A. and Burger, C.P. – Temperature compensation for strain gages mounted on trees. Rev. Sci. Tech., 2 (1) : 109-116 (1982).

[5] Burger, C.P.; Hall, R.B.; Johnson, D.B.; Baryeth, E.A. and Faltonston, R. R. – Strain gages measure growth characteristics of trees. Trans. ASAE, 25 (6) : 1685-1690 (1982).

[6] Burger, C.P.; Johnson, D.B.; Hall, R.B. and Schultz, R.C. – Automated strain gage dendrography for improved water utilization in plants. Iowa State Water Resources Research Institute, Report ISWRRI-126, Ames, Iowa (1983).

[7] Burger, C.P.; Johnson, D.B. and Schutte, K.H. – The application of phytomechanics to study the effects of nutrient deficiencies on the response of trees to water stress. Proceedings, 7th Canadian Congress of Applied Mechanics, Sherbrooke (1979), p.325-326.

[8] Burger, C.P.; Johnson, D.B. and Hall, R.B. – Dendrography for optimal water and energy utilization in plant growth. Iowa State Water Resources Research Institute, Annual Report (1980), p.123.

[9] Voloshin, A.S.; Wosk, J. and Brull, M. – Force transmission through the

human locomotion system. J. Biomech. Eng. (ASME), 103 : 48-50 (1981).

[10] Voloshin, A.S. and Wosk, J. — Shock absorbing capacity of the human knee (in vivo properties). Proceedings, Special Conf. of Canadian Soc. of Biomechanics on Human Locomotion--I, London, Ontario (1980), p.104-105.

[11] Brown, R. and Lingg, C. — Musculoskeletal compaints in an industry:Annual complaint rate and diagnosis, absenteeism and economic loss. Arthritis Rheum., 4 : 283-291 (1961).

[12] Voloshin, A.S. and Burger, C.P. — A comparative study of arch supports and shock absorbing devices. Ed. by M.L. Hull, Proceedings, UCD Biomedical Engineering Symposium, University of California, Davis (1982), p.55-58.

[13] Wosk, J.; Voloshin, A.S. and Burger, C.P. — Treatment of low back pain by reduction of axially propagated impulsive stress waves, Proceedings, 2nd Southern Biomedical Engineering Conference (1983).

[14] Voloshin, A.S. and Burger, C.P. — Transmissibility function of the healthy human knee (in vivo study). Proceedings, 1st Southern Biomedical Engineering Conference (1982).